

A Multidisciplinary Study of Pulse Detonation Engine Propulsion

DISTRIBUTION STATEMENT A
Approved for Public Release
Distribution Unlimited

Final Report
For Award number: ONR N00014-99-1-0744

Robert J. Santoro, The Pennsylvania State University
Vigor Yang, The Pennsylvania State University
Joseph E. Shepherd, California Institute of Technology
Chung K. Law, Princeton University

January 2003

20030123 060



EXECUTIVE SUMMARY

The Penn State-led MURI effort on Pulse Detonation Engine (PDE) Research is detailed in this report. The multidisciplinary research effort brought together a team of leading researchers in the areas of the initiation and propagation of detonations, liquid hydrocarbon spray detonation, combustion chemistry, injector and flow field mixing, and advanced diagnostics to study the fundamental phenomena of importance under both static and dynamic conditions representative of actual pulse detonation engine operation. The team focused its effort on conducting key experiments and analysis in the areas of (a) Fundamental Detonation Studies, (b) Injection, Mixing and Initiation, (c) Inlet-Combustor-Nozzle Performance, (d) Multi-Cycle Operation, and (e) Computer Simulation and Cycle Analysis. These study areas are five of seven topic areas that have been delineated by the Office of Naval Research (ONR) in their roadmap on pulse detonation engine research necessary for developing the technologies needed for the design of an air-breathing pulse detonation engine. The results obtained in these five study areas under this effort by researchers at Penn State, Caltech and Princeton University, coupled with the results of the effort by the sister MURI team led by the University of California at San Diego in some of the aforementioned study areas and in the remaining two study areas of (a) Diagnostics and Sensors, and (b) Dynamics and Control provide the foundation needed for the development of a PDE system. The overall success of the program stems from ONR led coordination that fostered collaboration between the two MURI research efforts and government laboratories and industry research through a series of progress workshops held at six-month intervals. The structured feedback provided by the participation of a Technical Advisory Committee composed of Government and Industry representatives was invaluable in assisting the MURI teams in accomplishing the research goals of the program.

TABLE OF CONTENTS

	Executive Summary	i
1.	Introduction	1
2.	Caltech Results	5
2.1.	Detonation Initiation	5
2.1.1.	DDT	5
2.1.2.	Hot Jet Initiation	8
2.1.3.	Basic Studies of Shock Focusing	9
2.1.4.	Wave Shaping	10
2.1.5.	Small Tubes	11
2.1.6.	Planar Initiator	12
2.1.7.	Toroidal Initiator	13
2.2.	Detonation Propagation	15
2.2.1.	JP10 Vapor Pressure Measurement	15
2.2.2.	PDE Fuel Characterization	16
2.2.3.	Detonation Structure	18
2.2.4.	Planar Laser Induced Fluorescence	18
2.2.5.	Detonation Diffraction	19
2.2.6.	Direct Measurements of Impulse	20
2.2.7.	Effect of Extensions	22
2.2.8.	Analytical Modeling of Impulse	25
2.3.	Tube Response to Detonation Loading	28
2.3.1.	Elastic Response	28
2.3.2.	Plastic Response	29
2.3.3.	Fracture	29
2.3.4.	PDE Design Parameters	30
2.4.	Summary	32
3.	Princeton Results	34
3.1.	Chemical Kinetics Effects on Induction Length	34
3.1.1.	Second-Limit Consideration for Hydrogen-Fueled PDE	36
3.1.2.	Chemistry Reduction for Hydrogen Oxidation in PDE	38

3.1.3.	Ignition Lengths of Hydrogen, Ethylene, and Heptane	41
3.1.4.	Hydrogen, Ethylene, and Oxygen as Additives	43
3.1.5.	Summary	45
3.2.	Propagation and Quenching of Spray Detonations	46
3.2.1.	Formulation	48
3.2.2.	Results and Discussion	52
3.2.2.1.	Effects of Droplet Size	52
3.2.2.2.	Effects of Pre-vaporization	57
3.2.3.	Summary	60
4.	Penn State Results	62
4.1.	Experimental Results	62
4.1.1.	DDT Studies	62
4.1.1.1.	Experimental Setup	64
4.1.1.2.	Single-Shot Results	68
4.1.1.3.	Multi-Cycle Results	82
4.1.2.	Detonation Transition Studies	83
4.1.2.1.	Experimental Setup	85
4.1.2.2.	Results and Discussion	86
4.1.3.	Summary	89
4.2.	Modeling Results	91
4.2.1.	Supersonic Inlet Dynamics	92
4.2.2.	Thermodynamic Cycle Analysis	95
4.2.3.	Single-Tube Thrust Chamber Dynamics	97
4.2.4.	Effect of Nozzle Configuration on PDE Performance	100
4.2.5.	Multi-Tube Thrust Chamber Dynamics	102
4.2.6.	Summary	105
5.	Summary	106
6.	References	110
	Appendix: Reduced Mechanisms	119

1. INTRODUCTION

Pulse detonation engines are receiving increased interest due to their potential for improved thermodynamic cycle efficiency. However, the present lack of understanding of important aspects of detonation physics as well as the desire to operate pulse detonation engines using liquid hydrocarbon fuels, which are difficult to detonate, poses serious barriers to their utilization. The present research effort brought together a team of leading researchers in the areas of the initiation and propagation of detonations, liquid hydrocarbon spray detonation, combustion chemistry, injector and flow field mixing, and advanced diagnostics. This Multidisciplinary University Research Initiative (MURI) team comprised of Profs. Robert J. Santoro (team leader) and Vigor Yang from Penn State, Prof. Joseph E. Shepherd from Caltech, and Prof. Chung K. Law from Princeton University.

Pulsed Detonation Engines (PDEs) potentially represent a revolutionary propulsion technology that offers advantages in cycle efficiency, hardware simplicity, operations and reliability. In particular, the potential for constant volume combustion with self-aspirating operation is highly attractive from an efficiency and operation perspective. These characteristics translate into propulsion systems possessing high performance, low development and life-cycle costs, and new advanced mission capabilities. Realization of the potential of PDE technology, however, is hindered by the absence of fundamental understanding of detonation phenomena as well as some key specific system related issues. Therefore, this effort to mature PDE technology broadly addressed a number of research issues that crossed disciplinary boundaries in an integrated program. Although the initiation and propagation of a detonation wave in the engine combustor is clearly the critical element in the PDE, achieving an operating engine that meets the performance goals requires development of several elements that include:

- suitable inlets that perform well over a Mach number range consistent with a multi-tube detonation chamber geometry,
- injection systems that provide rapid propellant mixing under conditions conducive to initiation of a detonation,
- inlet and injection schemes that allow for repetitive, highly reproducible detonations that occur in multi-tube detonation chambers,
- nozzles capable of high performance under conditions where pulsed combustor operation occurs as compared to steady state operation of present gas turbine or rocket engines.

Inefficiencies in any of these aspects of the PDE system can easily eliminate any inherent efficiency gains provided by the constant volume combustion process. Thus, it is critical to keep in mind that despite the importance of detonation phenomena, a PDE is a propulsion engine, not a single-pulse detonation tube. The challenges posed by PDE are further complicated by the requirement in most applications to use propellants that are "insensitive", i.e., difficult to detonate. Hydrocarbon-air mixtures are a clear example of this class of propellants.

This study addressed the fundamental phenomena of importance under both static and dynamic conditions representative of actual pulse detonation engine operation. Both experimental and theoretical efforts were included that focus on the key problem areas involving the detonation of insensitive propellants such as hydrocarbons and air. Both predetonator and main chamber detonation environments were studied and included consideration of the important areas of direct initiation, deflagration to detonation transition, and detonation wave diffraction from both single-pulse and multi-cycle perspectives. The objectives of the study included the integration of the results of fundamental studies of detonation phenomena to demonstrate multi-cycle operation of a pulse detonation chamber.

This MURI research effort was part of an overall ONR roadmap for advancing the fundamental scientific understanding necessary for developing a PDE system. The top level roadmap for the program is depicted in Fig. 1.1. Seven research areas were identified as being the most important for PDE technology development. This MURI team focused its efforts in the areas of (I) Fundamental Detonation Studies, (II) Injection, Mixing and Initiation, (III) Inlet-Combustor-Nozzle Performance, (IV) Multi-Cycle Operation, and (VII) Computer Simulation and Cycle Analysis. The second MURI team led by the University of California at San Diego focused on research areas I-III, IV and VI as shown in the roadmap. The MURI efforts were also coordinated with research efforts at the Naval Postgraduate School (NPS), Naval Air Warfare Center (NAWC) and Naval Research Laboratory (NRL).

In addition to advancing the state of maturity of pulse detonation engine technology, the present study provided for rapid transitioning of the understanding gained to industry. Effective coordination and collaboration of this research effort with the University of California at San Diego led MURI team, government laboratories and industry research programs have also been a key element of the work. This latter objective was accomplished through a series of progress workshops held at six month intervals to evaluate progress and assist in future planning. The participation of a



ONR PULSE DETONATION ENGINE RESEARCH ROADMAP

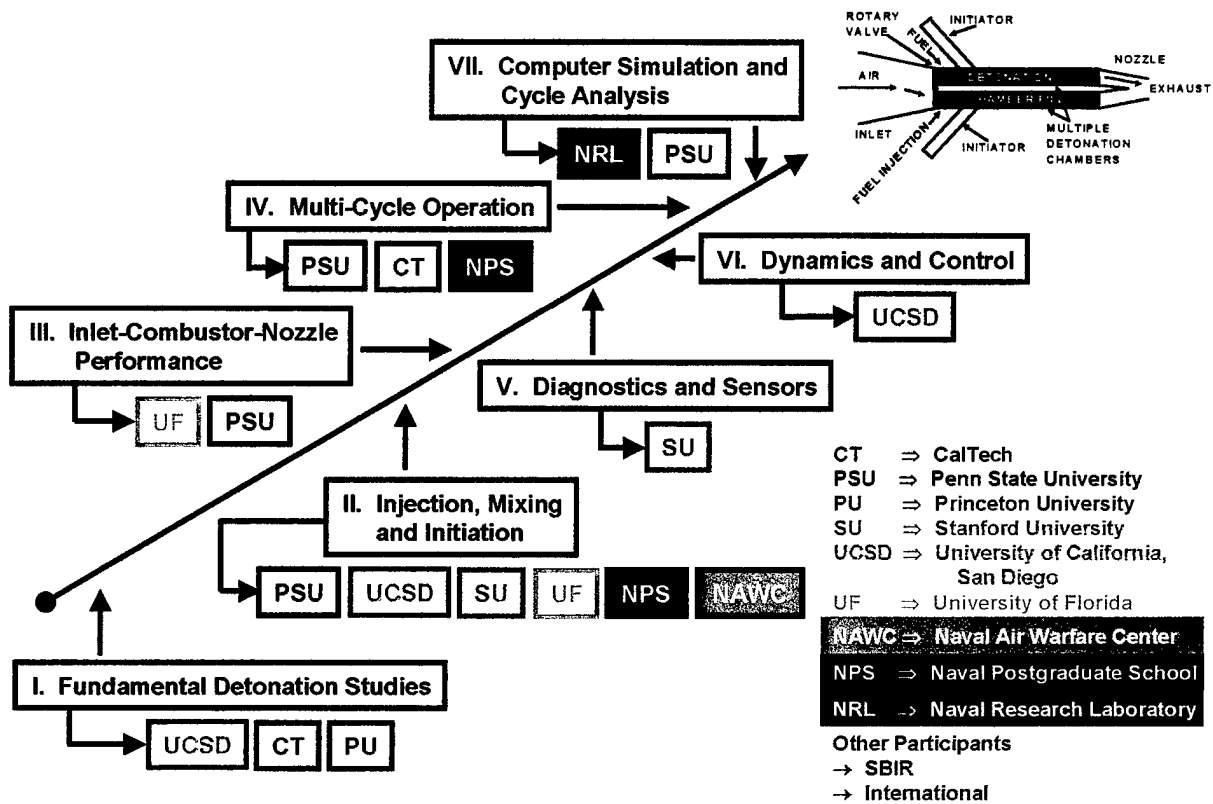


Fig. 1.1. Overall ONR Roadmap for Pulse Detonation Engine research.

Technical Advisory Committee composed of Government and Industry representatives provided the structured feedback that assisted the team in accomplishing the research goals of the program.

In the first area of fundamental detonation studies, Caltech conducted experimental and analytical research in the areas of detonation initiation, detonation propagation and tube response to detonation loading. In the same topic area, Princeton University analytically studied chemical kinetics effects on induction length, and propagation and quenching of spray detonations. These results are presented and discussed in Chapters 2 and 3 of this report, respectively.

The experimental research at Penn State was focused in topic areas (II) Injection, Mixing and Initiation, and (IV) Multi-Cycle Operation. Hydrocarbon/Air injection and mixing schemes for initiating and optimizing deflagration to detonation transitioning (DDT) were scientifically studied for both single-shot and multi-cycle conditions. Requirements necessary for successful transitioning of detonations from a small predetonator tube to a large detonator tube were also experimentally defined in this study area. Results are reported in Chapter 4.

Modeling studies at Penn State in the study areas of (III) Inlet-Combustor-Nozzle performance and (VII) Computer Simulation and Cycle Analysis focused on understanding supersonic inlet dynamics, both single-tube and multi-tube thrust chamber dynamics, and the effect of nozzle configuration on PDE performance. An overall thermodynamic cycle analysis was also performed. The results of this endeavor are also presented and discussed in Chapter 4.

2. CALTECH RESULTS

Research at the Explosion Dynamics Laboratories at Caltech has examined many issues critical to Pulse Detonation Engine (PDE) development. These include: fundamental and applied studies of detonation initiation; detonation cell width measurements to characterize fuels, including JP10; visualization of the reaction zone structure of propagating detonations; direct measurements and analytical modeling of impulse from a detonation tube, including the effects of partial fill and exit geometry; studies of detonation diffraction; and the structural response of tubes to detonation loading, including fracture and failure. Each of these aspects is discussed and key results are presented.

2.1. Detonation Initiation

A variety of techniques for detonation initiation in insensitive fuel-air mixtures (such as JP10 and air, or propane and air) for air-breathing PDE applications were investigated, including transition from flame to detonation, hot turbulent jet initiation, and shock and detonation wave focusing. Requirements for an initiation device for PDEs include: low energy, short length, and minimal flow obstruction.

2.1.1. DDT

Deflagration-to-detonation transition (DDT) is a mechanism of interest for use in practical engine design. However, current practice in designing detonation initiation systems using DDT is highly empirical and no design guidelines are available. A study of DDT initiation was performed for various fuels with oxygen and diluents [1]. The time required for detonation was measured as a function of initial conditions and correlated with the detonation and deflagration characteristics of the mixture.

The detonation tube used for the DDT experiments is 1.5 m long and has an internal diameter of 38 mm. The ignition source is a spark plug followed by a Shchelkin spiral. The spiral enhances transition of the spark-induced deflagration to a detonation. It is 305 mm long, has a 38 mm outside diameter, and a wire diameter of 4 mm. The distance between the coils is 11 mm. The tube is equipped with three pressure transducers spaced 400 mm apart along the length of the tube. The pressure transducers enabled the measurement of the DDT time, which is defined as the time from the spark discharge to the time at which a detonation wave

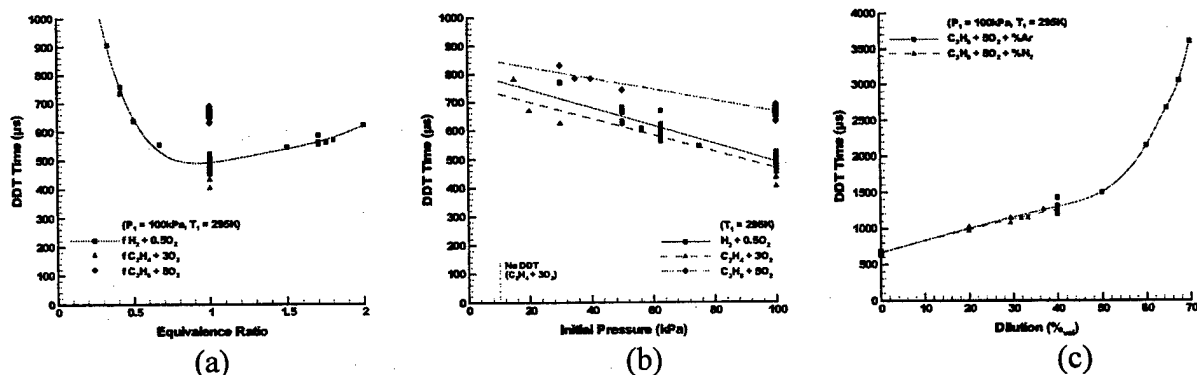


Fig. 2.1. DDT time as a function of initial conditions for fuel-oxygen mixtures. a) DDT time vs. equivalence ratio. b) DDT time vs. initial pressure. c) DDT time vs. percent dilution for propane-oxygen mixtures.

reached the first pressure transducer. A successful DDT event occurred if the wave propagated within +1% and -2% of the Chapman-Jouguet (CJ) detonation velocity from the first pressure transducer through the remainder of the detonation tube.

Experimental results are presented on Fig. 2.1. Multiple data points at the same condition indicate repeat experiments. DDT time data versus equivalence ratio in hydrogen-oxygen are shown in Fig. 2.1a. The familiar U-shaped behavior is observed with minimum DDT times occurring near the stoichiometric condition. At stoichiometric conditions, DDT times are greatest for propane, followed by hydrogen. The shortest DDT times are observed in ethylene. DDT times decrease with increasing pressure and the same hierarchy between fuels is maintained. Increasing the dilution increases the DDT time. Carbon dioxide was found to be the more effective inhibitor of the DDT process, followed by nitrogen, helium, and argon. Repeat experiments showed that the data followed a fairly normal statistical distribution, with temporal deviations around the mean of approximately $\pm 5\%$.

DDT times (t_{DDT}) were analyzed in terms of deflagration and detonation characteristic properties. In particular, characteristic times can be associated with ideal instantaneously-initiated detonations ($t_{CJ} = L/U_{CJ}$) and laminar flames ($t_{lam} = L/V_f$), where L is the distance from the spark plug to the first pressure transducer, U_{CJ} is the CJ detonation velocity, and V_f is the flame propagation speed, equal to the product of the burning velocity and the expansion ratio of the mixture. The time required for the acceleration and transition process is given by the excess transit time ($t_{DDT} - t_{CJ}$). Since the acceleration process is much slower than the detonation onset process, it is expected that the excess transit time is dominated by the time required for flame

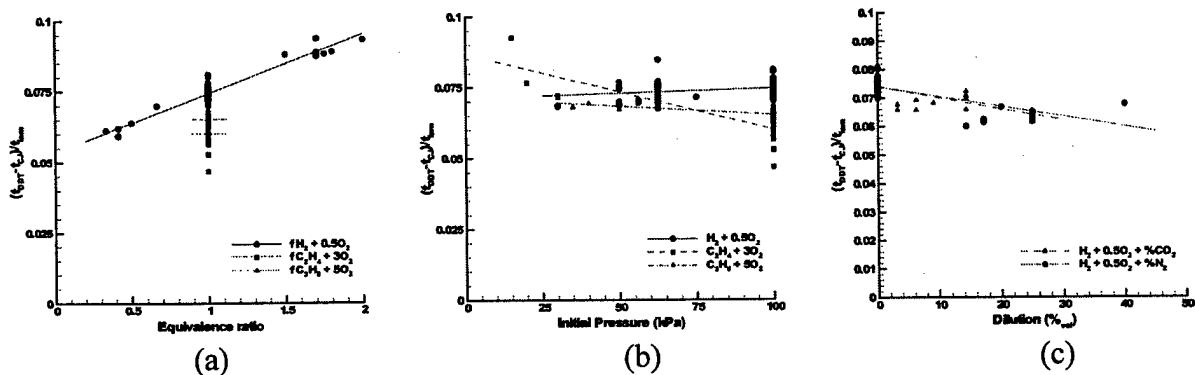


Fig. 2.2. Non-dimensional DDT for fuel-oxygen mixtures. a) vs. equivalence ratio. b) vs. initial pressure. c) vs. dilution for hydrogen-oxygen mixtures.

propagation within the spiral and that the excess transit time is proportional to the laminar flame propagation time. In general, the results will be a function of the geometry and mixtures parameters such as expansion ratio, σ , Lewis number, Le , and Zeldovich number, β . Non-dimensional DDT times, $(t_{DDT} - t_{CJ})/t_{lam}$ are shown on Fig. 2.2. All non-dimensional DDT times fall in a narrow range between 0.06 and 0.09. The modest range of variation indicates that the scaling ideas capture the essential dependence of the DDT time on the characteristic idealized time scales.

An attempt was made to correlate the non-dimensional DDT times with other non-dimensional flame parameters, such as the expansion ratio or the Zeldovich number. Figure 2.3 shows correlations with σ and $\beta(Le-1)$. The expansion ratio represents how much a

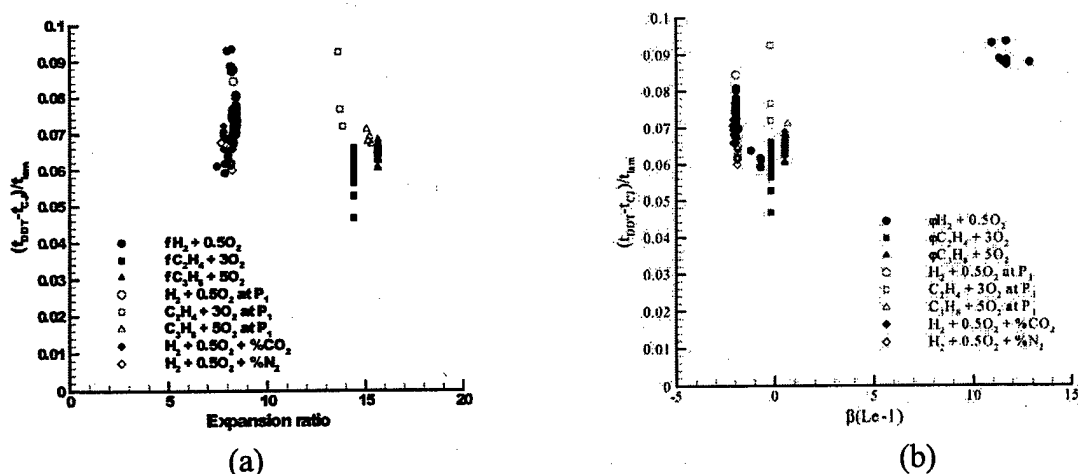


Fig. 2.3. Non-dimensional DDT time correlation. a) DDT time vs. expansion ratio. b) DDT time vs. $\beta(Le-1)$.

fluid particle will expand when it combusts. It is therefore expected that mixtures with higher expansion ratios will be more susceptible to DDT. The combination $\beta(Le-1)$ is expected to control the onset of cellular instability in flames. Unstable flames are expected to accelerate faster than stable flames. In general, large expansion ratios and small Lewis numbers are conducive to minimizing DDT time. No special influence of the Zeldovich number was identified in this study. Further work with a large range of values will be required in order to isolate the role of this factor.

2.1.2. Hot Jet Initiation

The effectiveness of using a hot turbulent jet to initiate a detonation in a short distance was investigated experimentally [2]. A turbulent jet of combustion products, passing from a driver section through an orifice into a test section, was used to initiate a turbulent flame in the test gas. The turbulent flame may transition to detonation. Such low-energy methods of detonation initiation are of particular interest to PDEs.

The experiments were performed in the ballistic pendulum facility with a tube that consists of two vessels: a 100 cm³ volume driver section and a 1 m long by 76.2 mm diameter test section. The vessels are connected by an orifice, the diameter of which can be varied. The test section is equipped with three pressure transducers and ten ionization probes to measure the pressure history and wave velocity. The driver section has a pressure transducer on the ignition end wall. The driver is filled with a stoichiometric propane-oxygen and the test section is filled with stoichiometric propane-oxygen mixture with varying nitrogen dilution. A Mylar diaphragm initially separates the driver and test gases. The aim of the current study is to examine the effect of the orifice diameter and the initial pressure of the driver section on the maximum (or critical) nitrogen dilution for which a detonation can be initiated in the test section.

Driver pressure is found to have a mild effect on the critical N₂ dilution, see Fig. 2.4. Increasing the driver pressure by a factor of four resulted in an increase in the critical N₂ dilution from 30% to 40%. Figure 2.5a shows the effect of varying the orifice diameter on the critical N₂ dilution with the initial driver pressure at 1 bar. Increasing the orifice diameter from 3 mm to 19 mm increases the critical dilution level from 30% to 40% N₂. Figure 2.5b shows measured I_{sp} versus test section N₂ dilution for initial driver pressures of 1 to 4 bar. The orifice diameter is 3.125 mm. The solid line corresponds to the theoretical impulse model proposed by

Wintenberger et al [3]. Experiments were also carried out with an array of orifices to examine the role of jet mixing. For a given open area, the multiple hole geometry resulted in a 5% increase in the critical dilution level over the equivalent single hole geometry.

2.1.3. Basic Studies of Shock Focusing

Shock wave focusing is a method that can be used to initiate detonations in insensitive mixtures and has a low energy input requirement. Shock wave focusing involves the collision of two or more shock waves. In the region behind the colliding shock waves, high pressures and temperatures occur. In general, increased temperatures and pressures facilitate the initiation of detonation. The characteristics of the focal region was examined in order to develop criteria for the initiation of detonations under these conditions.

The study was performed by using numerical simulation to examine shock focusing in non-reactive mixtures and making comparisons with previous results. The results of several simulations are shown and compared to experimental data in Fig. 2.6. Pressure and temperature amplifications were found to be very sensitive to the type of reflection. Three types of reflection

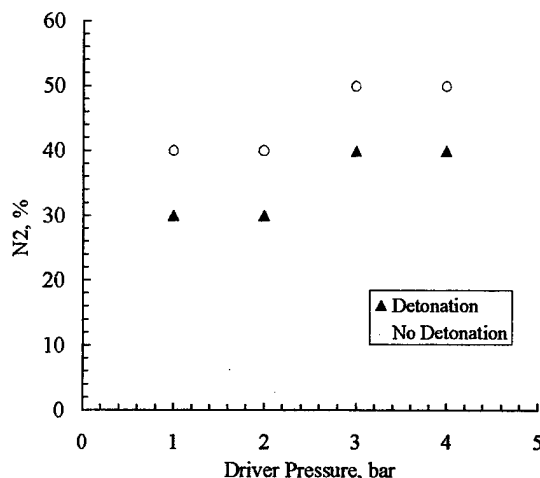


Fig. 2.4. Critical N₂ dilution amount vs. initial pressure in the driver section.

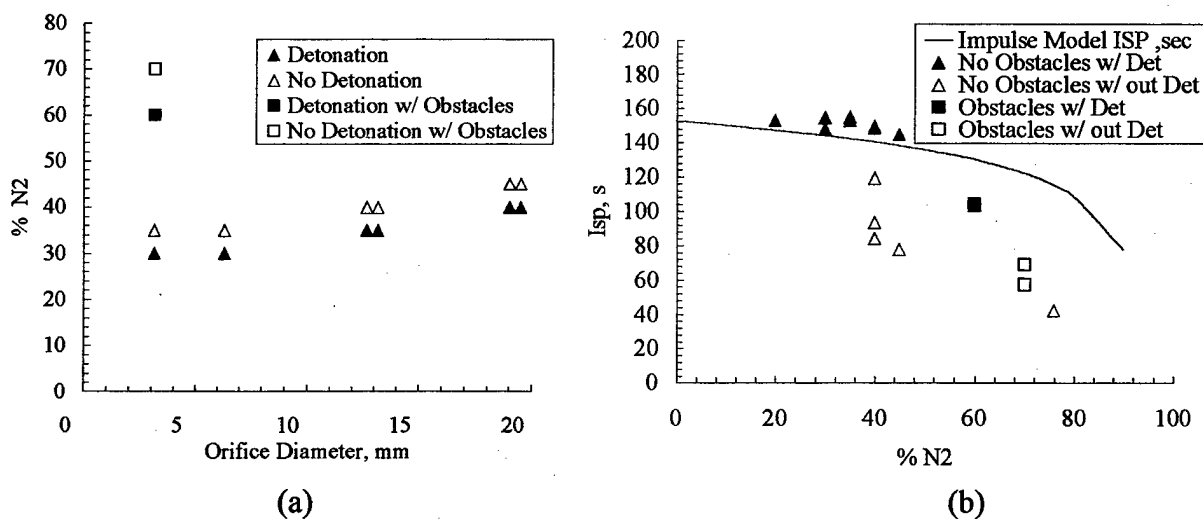


Fig. 2.5. a) Critical N₂ dilution amount vs. orifice diameter. b) Corresponding I_{sp} measurements.

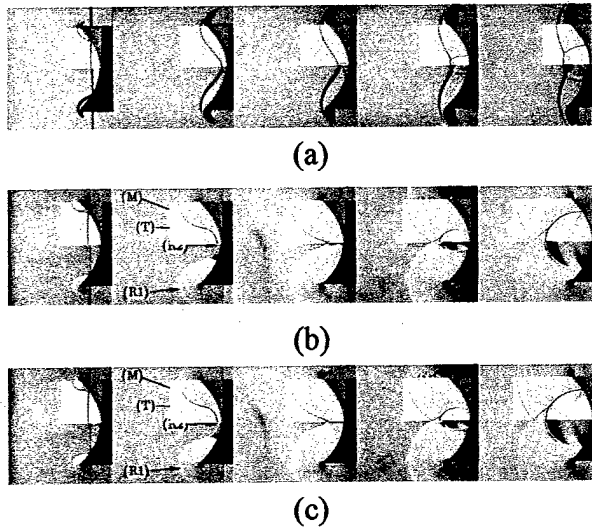


Fig. 2.6. Numerical simulations of shock wave focusing using Amrita [4] and comparisons with previous experimental results of Izumi et al. [5].

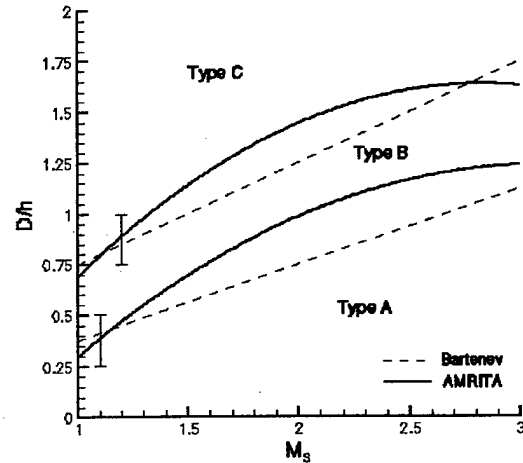


Fig. 2.7. Map of focusing regimes as a function of reflector geometric parameters (D/h is the depth-to-half-height ratio) and incident shock Mach number M_s . Comparison between CFD (Amrita [2]) and previous studies (Bartenev et al. [6]).

are observed and were characterized as a function of the incident wave strength and the reflector geometry. Type A reflection is characterized by the formation at focusing of a strong Mach stem growing with time, leaving an open focal region. This reflection type occurs for strong shocks and shallow reflectors. Type B reflection occurs when the diffracted shocks at the reflector edges intersect on the axis after focusing and then precede the Mach stem. Type C reflection occurs when the diffracted shocks at the reflector edges intersect on the axis before focusing. It results in a closed focal region, a small triangular region of fluid that is compressed by focusing. This reflection type is characteristic of weak shock waves and deep reflectors. A summary of the reflection regimes is given in Fig. 2.7. Type C reflection was found to produce higher pressure and temperature amplification; however, this amplification is usually followed by a very strong expansion.

2.1.4. Wave Shaping

Efficient methods of initiating detonations in insensitive fuel-air mixtures (such as JP10 and air, or propane and air) are of interest for air-breathing PDE applications. A necessary step in moving from laboratory demonstration to actual propulsion systems is the development of a device capable of efficiently generating the pressures and temperatures necessary to initiate detonations in these mixtures. It is desirable to develop a system capable of initiating

detonations in hydrocarbon-air mixtures with a low-energy spark (less than 100 mJ) for use in short length, small diameter detonation tubes. The use of low spark energy eliminates the possibility of direct initiation of detonations in the mixtures of interest. Previous work at Caltech has investigated the potential of several initiation concepts that involve low-energy input, such as DDT, use of driver tubes, and wave focusing techniques. Each concept was evaluated for use with air-breathing PDEs. One such concept involves detonation wave focusing. In detonation wave focusing, a toroidally-collapsing detonation wave generates a high-pressure and -temperature focal region by adiabatically compressing products as they flow into an ever-decreasing area. The compression increases the post-detonation wave pressure higher than the CJ pressure, which results in an accelerating detonation wave.

The following sections describe a program [7] designed to maximize transmission efficiency by generating high-energy density regions via an imploding toroidal detonation wave. First, research was conducted on detonation propagation through small tubes. This determined the minimum tube diameter (and thus gas volume) necessary to propagate stable detonation waves. Second, a device capable of generating a planar detonation wave was developed to verify that several detonation fronts initiated from a weak spark and propagated through small tubes could be merged to create a detonation wave with a planar front. Finally, a low-drag initiator system capable of producing a repeatable, high-pressure focal region with a minimum amount of driver gas was built using experience gained from small tube and planar initiator data.

2.1.5. Small Tubes

In order to minimize the amount of sensitive driver gas used in detonation initiators, the initiator volume should be as small as possible. However, as the length scale of the initiator approaches the order of the cell size of the mixture, losses due to boundary layer effects can become significant. Such losses can cause the detonation wave to fail or weaken it enough to interfere with the operation of the initiator. Thus, knowledge of minimum tube diameters and minimum initial pressures necessary to avoid severe boundary layer effects is crucial for design of an efficient system.

Researchers such as Manzhalei [8] have identified and characterized modes of detonation propagation through small tubes in acetylene-oxygen mixtures. However, limited information is available on the regime of stable propagation in propane mixtures. It was necessary to carry out

experiments to establish the stable detonation regimes in propane-oxygen in order to optimize the initiator design.

A detonation wave was initiated in a driver tube and propagated into a small tube test section. The small tube test section was equipped with three pressure transducers for velocity and pressure measurements. Test sections of 1.27 mm and 6.35 mm inner diameters were used. Propane-oxygen mixtures were tested, varying the initial pressure and equivalence ratio. Data indicated that significant (>10%) velocity deficits were present when the ratio of induction distance to tube radius was greater than 0.1. This corresponds to a minimum tube diameter of 1.27 mm for stoichiometric propane-oxygen mixtures at 1 bar.

The experiments determined the minimum tube diameter necessary to propagate a detonation through a straight, unobstructed tube. The inclusion of corners, bifurcating channels, and other geometries likely to promote detonation diffraction necessitates larger tube diameters in order to ensure successful detonation propagation.

2.1.6. Planar Initiator

A device capable of producing a planar detonation wave was successfully built and tested to demonstrate the principles of merging a series of wave fronts into a single front. This device served as a stepping-stone in the development of the toroidal wave generator discussed below. The planar initiator is capable of producing a large aspect ratio, planar detonation from a weak spark ignition source.

The planar version, shown in Fig. 2.8, consists of a main channel with secondary channels branching off the main channel. All secondary channels terminate on a line and exhaust into a common test section area. The channel geometry is such that all path lengths from the spark point to the secondary channel termination line are equal. For use with propane-oxygen mixtures, the main channel width was 9.53 mm and the length was 0.431 m. The width of the secondary channels was 5.08 mm and the secondary channel spacing was 2.54 mm. All channels were square in cross-section. The channels exhausted into a test section 0.305 m wide and 0.152 m long. The test section contained a ramp near the secondary channel exhaust that enlarged the channel depth from 5.08 mm to 19.05 mm over a distance of 38.1 mm. The device was filled from a reservoir with premixed propane-oxygen or ethylene-oxygen

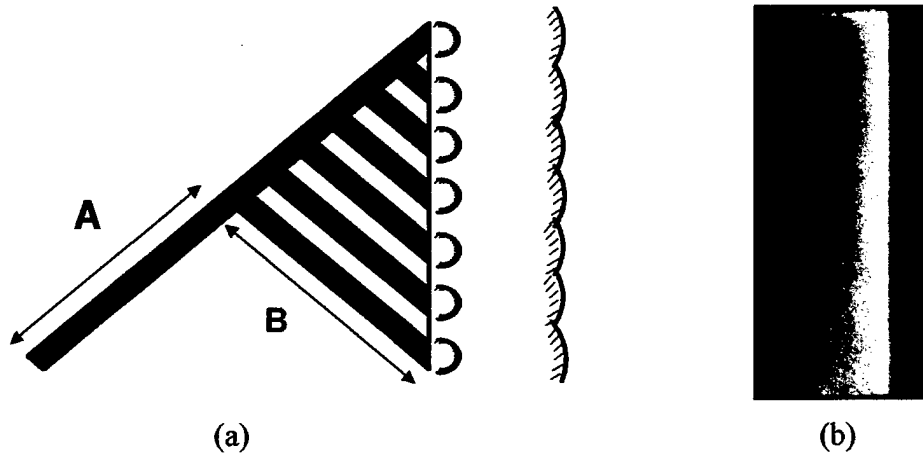


Fig. 2.8. a) Schematic of planar initiator. ($A+B = \text{constant}$ for all paths.) b) chemiluminescence image of merged planar detonation front. Flow is left to right. Image height is 0.3 m and width is 0.13 m.

mixtures. A spark plug and associated discharge system with 30 mJ of stored energy was used to ignite the combustible mixture.

The presence of obstacles in the main channel promoted DDT, resulting in a detonation that travels down the main channel with small fronts branching off and traveling down the secondary channels. All detonation fronts exhaust into the test section at the same time and combine to form a planar detonation front. Images and pressure traces show that the device produces planar waves with deviations of less than 1 mm over the width of the test section. The results are extremely repeatable. A chemiluminescence image of the detonation front is shown in Fig. 2.8. The planar initiator allows for efficient generation of planar detonation waves with large aspect ratios over a short distance.

2.1.7. Toroidal Initiator

To create a toroidal wave, the planar initiator design was modified such that the exit of each channel lies on a circle with the channels exhausting inwards. This involved mapping the planar design onto a cylinder, creating an annular imploding wave instead of a planar wave as shown in Fig. 2.9. The mapping transforms the metal substrate containing the channels into an inner sleeve while the cover plate becomes the outer sleeve. A pressure seal between the inner and outer sleeves was created by a shrink fit. All initiator channel dimensions are similar to that of the previously described planar initiator. The small channels exhaust into a test section that is 76.2 mm in diameter. The design allows the initiator to be incorporated into the walls of a PDE.

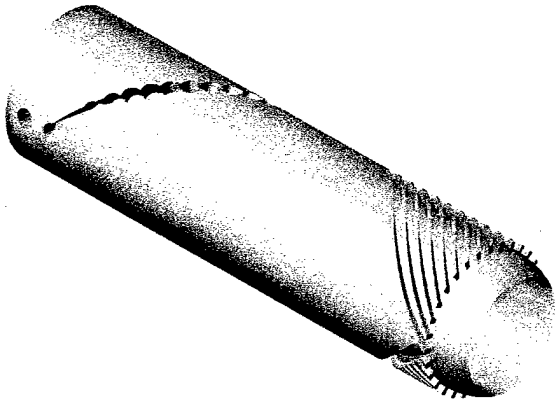


Fig. 2.9. Schematic of annular detonation wave initiator. (Covering shell omitted for

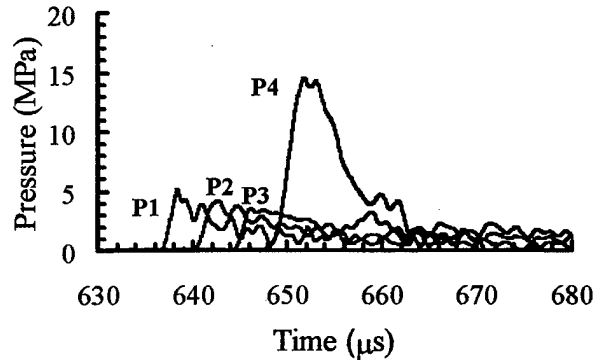


Fig. 2.10. Pressure traces from annular initiator tests.

Since no part of the initiator is inside the flow path, drag losses are expected to be minimal in PDE applications.

Testing was performed in stoichiometric propane-oxygen mixtures initially at 1 bar. The device was filled using the method of partial pressures. The mixture was circulated to ensure homogeneity using a bellows pump which limited initial pressures to 1 bar or greater. Pressure history was obtained at locations near the focus of the collapsing torus by four pressure transducers, one of which was placed as close to the implosion axis as possible. The distance separating the pressure transducer axis from the implosion center was 19.05 mm. The transducers were equally spaced 10.7 mm apart on a radial line with the central transducer located on the central axis of the initiator tube. A typical set of pressure traces is shown in Fig. 2.10. Images of the detonation front luminosity were also obtained. A series of images of the collapsing detonation wave are shown in Fig. 2.11.

The outermost three pressure transducers show a gradually decreasing pressure wave as the radius of the imploding torus decreases. The central pressure transducer, however, recorded a value above its maximum reliable operating range. This value was four times larger than the CJ pressure for the mixture. Images of the detonation front show a fairly regular collapsing toroidal wave. A structure behind the wave is also visible and may be due to the detonation interacting with the window.

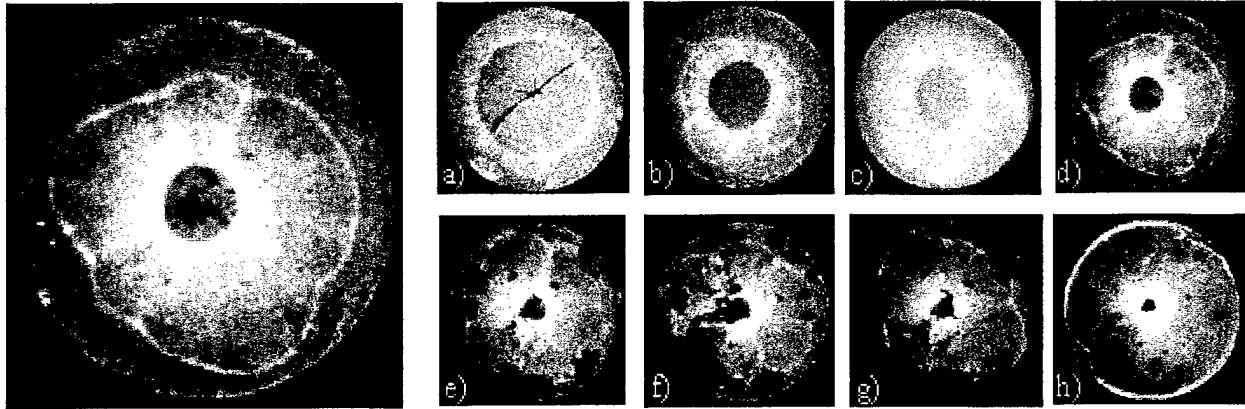


Fig. 2.11. Chemiluminescence images of imploding detonation wave. Irregular secondary wave is thought to be due to interaction with window.

2.2. Detonation Propagation

2.2.1. JP10 Vapor Pressure Measurement

JP10 vapor pressure measurements were carried out to obtain reliable data for use in JP10 detonation experiments. The experimental facility was similar to that used in previous [9] vapor pressure measurements in Jet-A. A vessel containing liquid JP10 was placed in an ethylene glycol bath. The ethylene glycol temperature was regulated by a feedback-controlled heating system. Thorough mixing of the ethylene glycol and insulation of the bath ensured a uniform temperature distribution. The temperature was set using a digital controller and measured using thermocouples in the bath and in the test liquid. The temperature was varied from ambient to 120°C.

The vapor pressure of JP10 was measured in steps of 10°C using a digital pressure gauge. At every step, pressure measurements were taken only after ensuring that the temperature of the bath and the test liquid was stable. The vessel was then evacuated at the start of the experiment and at each temperature, the pressure was allowed to build up to a constant value before the pressure was recorded. The results are plotted on Fig. 2.12. The error bars represent the uncertainties in the measurements, which are $\pm 2\%$ for the temperature and $-0.13/+0.28$ kPa for the measured pressure, accounting for gauge precision and leak rate.

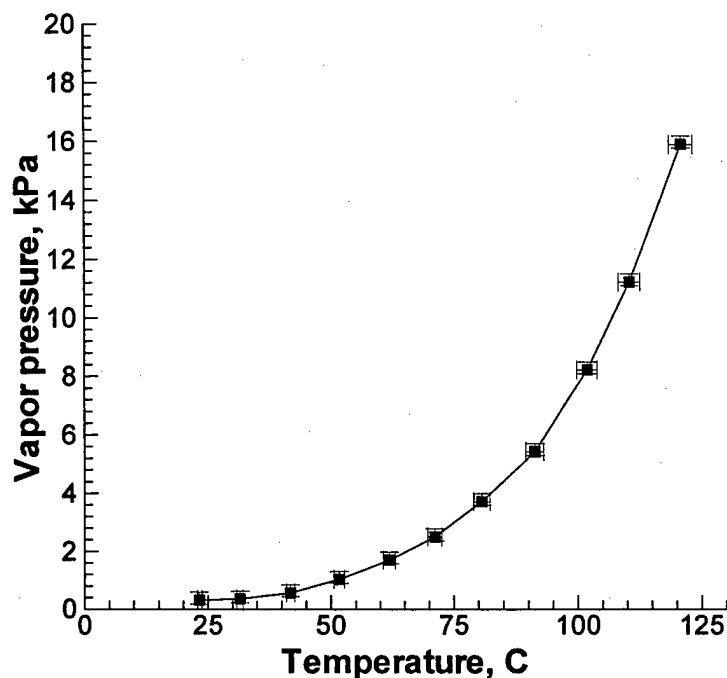


Fig. 2.12. Measured vapor pressure of JP10.

2.2.2. PDE Fuel Characterization

Liquid hydrocarbons are the fuel of choice for aviation propulsion systems, including the PDE. Much of the published PDE research to date has used low molecular weight hydrocarbon fuels (C_1 - C_3) due to the difficulty of creating uniform fuel-air mixtures with liquid hydrocarbon fuels and initiating detonations in these mixtures. The detonation cell width, defined as the average transverse wave spacing recorded on a sooted foil (Fig. 2.13), is a useful measure of the sensitivity of a mixture to detonation. Generally speaking, the smaller the cell width, the smaller the minimum energy required to initiate detonation. The cell width can also be empirically related to other dynamic parameters such as the minimum tube diameter that is required for detonation propagation.

During the course of this program, the Caltech 280 mm detonation tube was modified to include a heating system and strengthened to extend the range of operation with liquid fuels and higher oxygen concentrations. The cell widths in vaporized JP10 have been measured at temperatures above 80°C for several mixtures [10]: a) JP10-air at 100 kPa for equivalence ratios between 0.7 and 1.4 (Fig. 2.14). b) stoichiometric JP10- O_2 and JP10-air for initial pressures between 20 and 130 kPa (Fig. 2.15) c) JP10- O_2 - N_2 at an equivalence ratio of one and nitrogen amounts between zero and air equivalent (Fig. 2.16). The cell widths of JP10 mixtures were

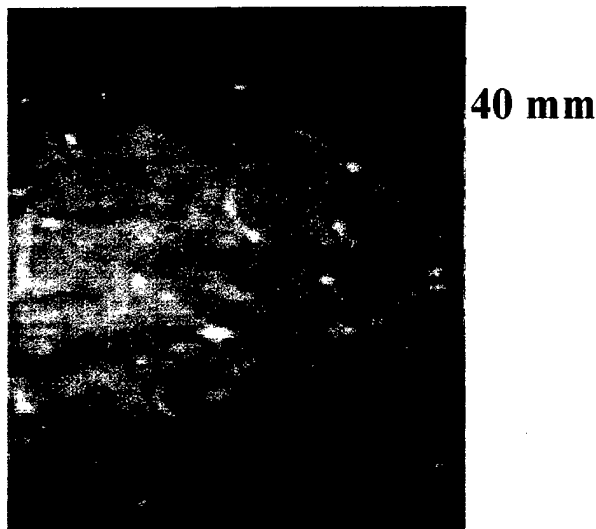


Fig. 2.13. Soot foil of JP10-20% C_2H_2 -Air. Detonation propagated from left to right.

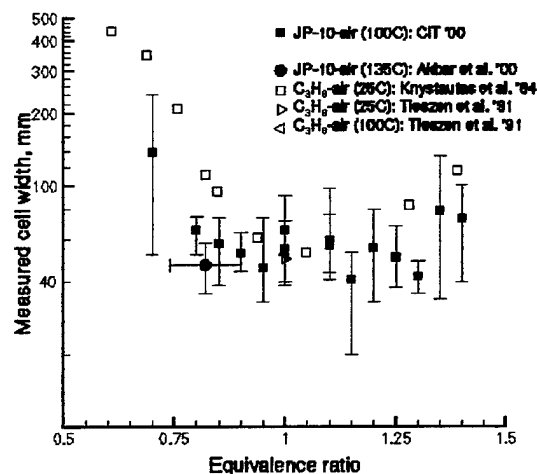


Fig. 2.14. Detonation cell width measurements in JP10-Air vs equivalence ratio. Propane data are shown for comparison.

found to be comparable to those of propane and hexane mixtures. This result suggests that propane may be a useful surrogate fuel for preliminary PDE studies.

The addition of hydrocarbon fuels to JP10 was investigated (Fig. 2.17). C_2H_2 , C_2H_4 , and CH_4 were chosen as examples of low-molecular weight hydrocarbons that result from thermal or catalytic decomposition [11] of JP10. Such data will also be of use in validation studies for JP10 reaction mechanisms.

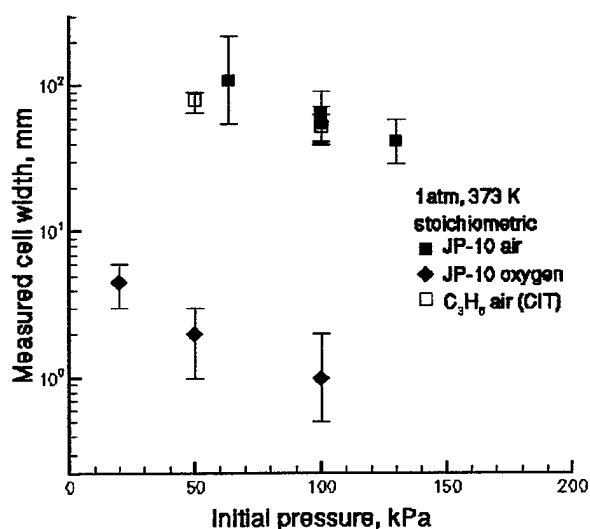


Fig. 2.15. Cell width measurements in JP10-air with varying initial pressure.

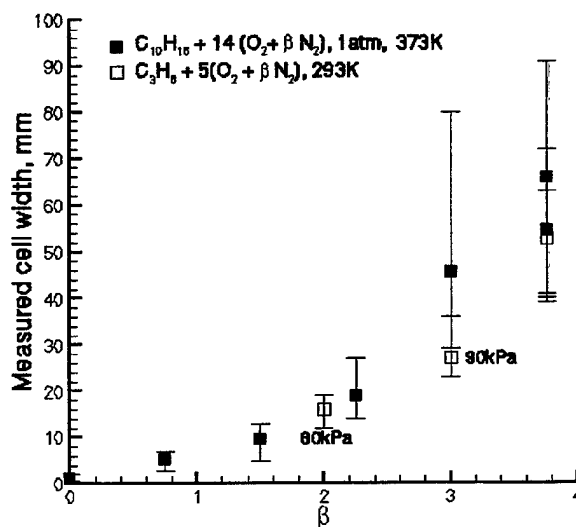


Fig. 2.16. Cell width measurements in JP10- O_2 with varying nitrogen dilution to JP10-air.

2.2.3. Detonation Structure

Several important areas of PDE development such as initiation, minimum tube size, and tube geometry benefit from greater understanding of the fundamental mechanism by which detonation waves propagate. The cellular nature of all detonation waves propagating near the CJ velocity is well known and may be observed from tracks on sooted foils, as discussed above. Previous researchers [13-16] have also used schlieren and interferometry to visualize shocks in the detonation front but resolved experimental images of chemical species in the reaction zone have been lacking.

2.2.4. Planar Laser Induced Fluorescence

A dye-laser and optical system were purchased and integrated with existing equipment, cameras and an excimer laser, to create a Planar Laser Induced Fluorescence (PLIF) capability. The experiments were successful in visualizing OH fluorescence and simultaneous schlieren visualization on detonation waves propagating H_2/O_2 /diluent (N_2 and Ar) in a 150 mm by 150 mm test section [17]. Characteristic "keystone" structures in the OH intensity have been revealed and correlated with detonation wave instability structures computed on the basis of reduced chemistry and also inferred from gas dynamic considerations. A marked difference in structure is observed between nitrogen and argon diluted mixtures, which agrees with the known characterization of the cellular structures as irregular and regular, respectively [18].

In the current experimental setup, three-dimensional effects complicate both schlieren and PLIF images (Fig. 2.18). An investigation was made of the possibility of simplifying the flow field by damping out-of-plane transverse waves using a porous wall (Fig. 2.19). The technique was found to be successful, but only for a limited range of mixtures. The experiments also studied detonation propagation through narrow channels of different

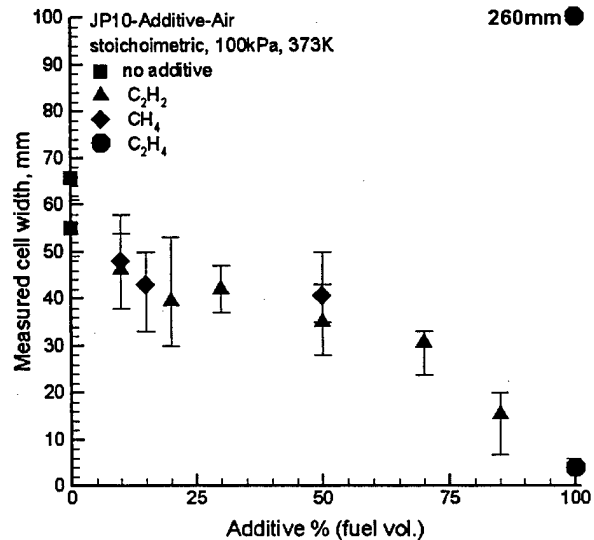


Fig. 2.17. Detonation cell width measurements in JP10-hydrocarbon-air at 100 kPa initial pressure, 353 K initial temperature. All data points for hydrocarbon-air are from Tieszen et al. 1991 [12]. CH_4 -Air cell width is actually 260 mm.

widths. Diagnostics included soot foils to record cell structure (Fig. 2.20) and pressure gauges to measure velocity deficits.

2.2.5. Detonation Diffraction

Diffraction of detonations in H_2 , C_2H_4 , and C_3H_8 in O_2 /diluent from a 38-mm orifice into a 150 mm by 150 mm test section [19] has been investigated (Fig. 2.21a). Single-frame laser schlieren, rotating-mirror framing, and chemi-luminescence images have been used to develop an analytical model of critical conditions for detonation diffraction. The model uses a detailed reaction mechanism validated against experimental shock tube data from a wide variety of sources. Excellent quantitative agreement has been obtained between experimental and computed critical tube diameters (Fig. 2.21b).

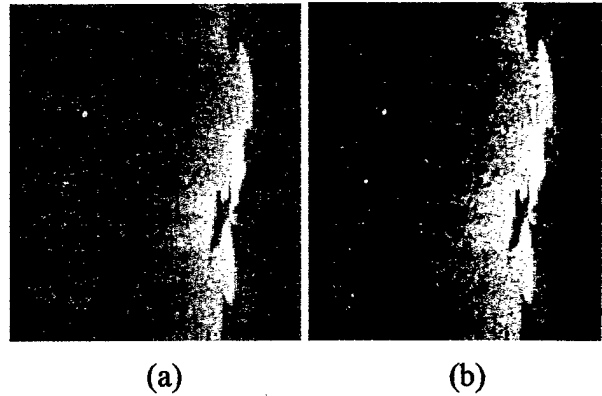


Fig. 2.18. OH PLIF images of reaction zone structure in $2H_2-O_2-4.5N_2$ (a) and $2H_2-O_2-17Ar$ (b) at 20 kPa.

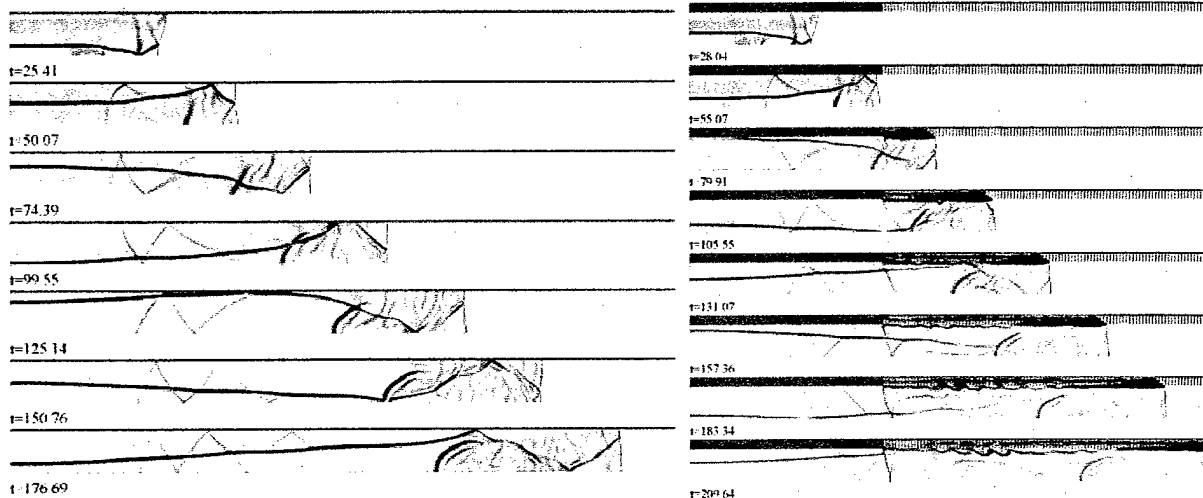
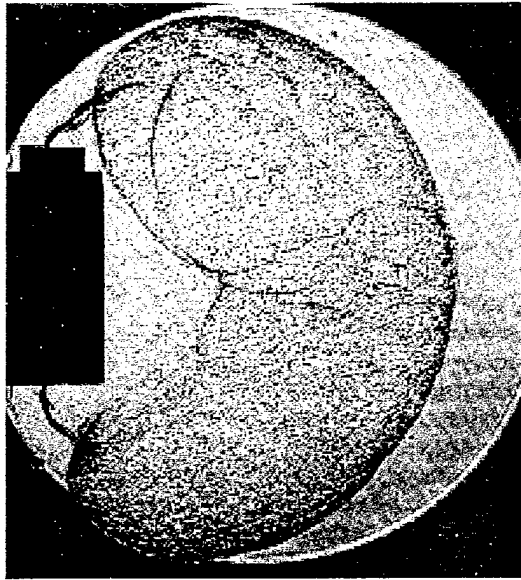


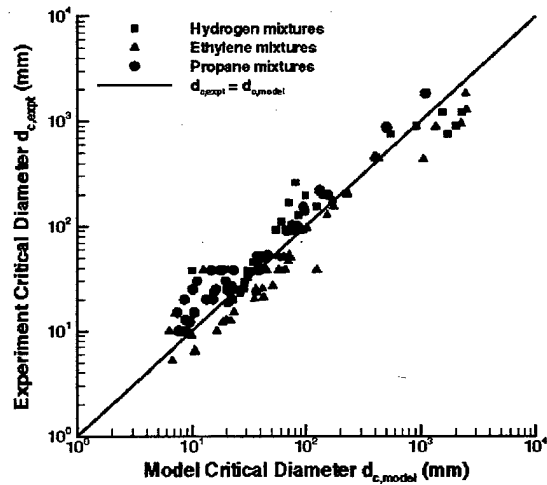
Fig. 2.19. AMRITA [4] simulations of a Mach stem propagating over solid and porous walls by Prof. H.G.Hornung, Caltech. The transverse wave is damped on reflection from the porous surface.



Fig. 2.20. Soot foil obtained in 18 mm channel with porous wall in $2H_2-O_2-3Ar$, 30kPa. The detonation propagated left to right. Triple point tracks are significantly weakened downstream of the porous wall (far right), corresponding to damped transverse waves.



(a)



(b)

Fig. 2.21. a) Laser shadowgraph image of detonation diffraction in the critical regime. b) Experimental critical diameter data vs. model prediction.

2.2.6. Direct Measurements of Impulse

Impulse per cycle is one of the key performance measures of a PDE. In order to evaluate the performance of the engine concept, it is necessary to have reliable estimates of the maximum impulse that can be obtained from the detonation of a given fuel-oxidizer combination at a specified initial temperature and pressure. While the overall performance of an engine will depend strongly on a number of other factors such as inlet losses, nonuniformity of the mixture in the detonation tube, and the details (nozzles, extensions, coflow, etc.) of the flow downstream of the detonation tube exit, conclusive studies investigating the impulse available from a simple detonation tube are essential.

Direct impulse measurements were carried out [20] using a ballistic pendulum arrangement for detonations and deflagrations in a tube closed at one end (Fig. 2.22). Three tubes of different lengths and inner diameters were tested with stoichiometric propane- and ethylene-oxygen-nitrogen mixtures. Results were obtained as a function of initial pressure and percent diluent. Experimental results were compared to predictions from an analytical model [21] and generally agreed to within 15%. The effect of internal obstacles on the transition from deflagration to detonation was studied. Three different extensions were tested to

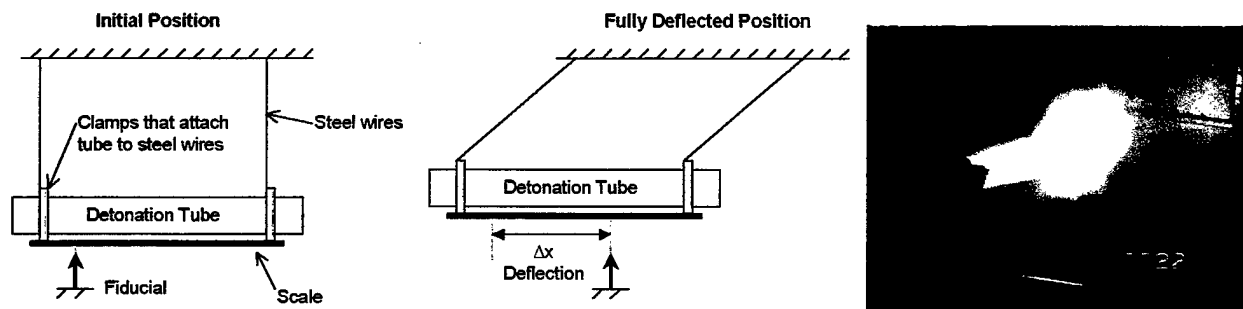


Fig. 2.22. Schematic and photograph of ballistic pendulum experiment.

investigate the effect of exit conditions on the ballistic impulse for stoichiometric ethylene-oxygen-nitrogen mixtures as a function of initial pressure and percent diluent.

All mixtures were ignited by a spark with a discharge energy (30 mJ) much less than the critical energy required for direct initiation of a detonation (approximately 283 kJ for propane-air mixtures [22] and approximately 56 kJ for ethylene-air mixtures [22] at atmospheric conditions). Thus, detonations were obtained only by transition from an initial deflagration. The presence of a deflagration is denoted by a gradual rise in the pressure histories as the unburned gas ahead of the flame is compressed due to the expansion of the burned gases behind the flame. If the correct conditions exist, this initial deflagration can transition to a detonation wave. Otherwise, transition will not occur and the deflagration wave will travel the entire length of the tube.

Direct impulse measurements for propane- and ethylene-oxygen-nitrogen mixtures were made with different obstacle geometries. Figure 2.23 shows impulse as a function of diluent amount for the 0.609 m tube with Shchelkin spiral obstacles. It can be seen that the obstacles with a smaller pitch have a lower impulse than those with a larger pitch. This loss in impulse is attributed as being due to a greater form drag associated with the flow around the obstacles as the spiral pitch decreases. At 100 kPa, a 5% reduction in the distance between successive coils causes a 13% reduction in impulse if the spirals extend over the entire tube length. In Fig. 2.24, the impulse for blockage and orifice plate obstacles is shown. Although obstacles can induce DDT in less sensitive mixtures and significantly increase the impulse, the obstacle drag can decrease the impulse by an average of 25% from the value measured without obstacles when fast transition to detonation occurs. When obstacles are present, the impulse obtained from integrating the thrust wall pressure history significantly overpredicts the actual impulse.

From Fig. 2.24, it can be seen that, without obstacles, detonation cannot be achieved in this tube for nitrogen dilutions of 40% or greater. A dramatic drop in measured impulse occurs

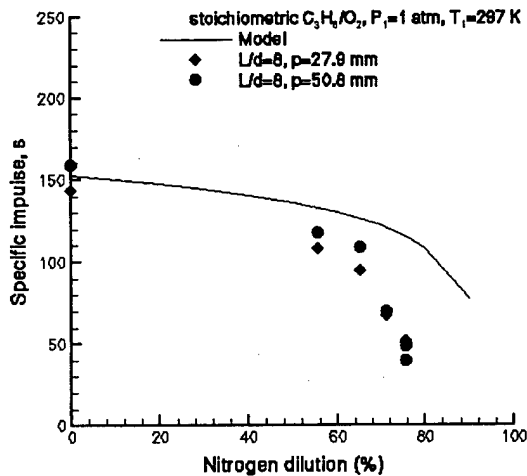


Fig. 2.23. Measured impulse vs. N_2 dilution for different spiral geometries.

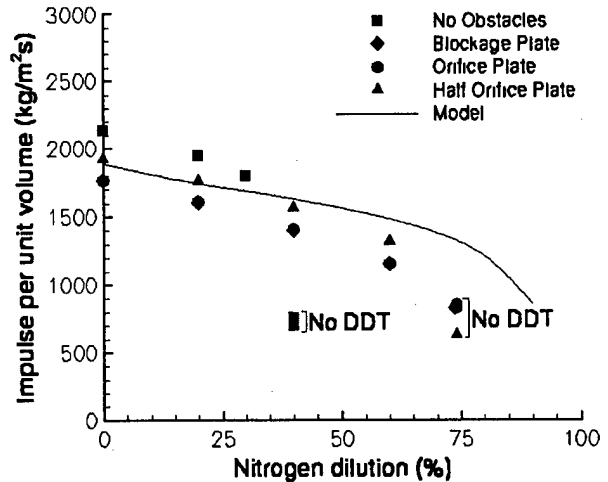


Fig. 2.24. Measured impulse vs. N_2 dilution for orifice and blockage plates.

for these mixtures. The addition of obstacles enabled DDT to occur in mixtures with up to 60% nitrogen dilution. Deflagrations propagate slowly through the tube, compressing the unburned gas ahead of the flame. This unburned gas compression is sufficient to rupture the thin diaphragm causing a considerable part of the mixture to be ejected outside the tube. The mixture ejected from the tube does not contribute to the impulse due to its unconfined burning. The effect of this mixture spillage due to no DDT can be seen in the cases with greater than 70% diluent where a 30-50% reduction in impulse is observed. The onset of a detonation wave can mitigate this effect if it occurs sufficiently quickly. If DDT occurs early enough in the process, the detonation can overtake the compression waves created by the deflagration before they reach the diaphragm. Cases of late or no DDT illustrate the importance of more sophisticated initiation methods for less sensitive fuels, such as storable liquid hydrocarbons (Jet A, JP8, JP5 or JP10) with cell widths similar to propane. Experiments with more sensitive ethylene-oxygen-nitrogen mixtures show that using obstacles to induce DDT within the tube can be effective.

2.2.7. Effect of Extensions

Proposed concepts for pulse detonation engines have often included the addition of different kinds of extensions, including nozzles, to the basic straight detonation tube. In part, this is motivated by the effectiveness of converging-diverging nozzles in conventional rocket motors. The effectiveness of a converging-diverging nozzle is based on the steady flow conversion of the thermal to kinetic energy. However, the PDE is an unsteady device that relies

on waves to convert the thermal energy into kinetic energy. It is not obvious how a nozzle would affect performance since the diffraction of the detonation wave through a nozzle is a complex process that involves significant losses. This problem was approached experimentally by examining the effect of various exit treatments on the measured impulse. For the tests, a thin diaphragm separates the tube length filled with the combustible mixture from the extension, which was filled with air at atmospheric conditions. This simulates the condition of having a single tube only partially filled with explosive mixture.

Three different extensions were tested on the detonation tube with a length of 1.016 m in a ballistic pendulum arrangement to determine their effect on the impulse. Each extension modified the total tube length, L , while the charge length, L_0 , remained constant. The first extension was a flat plate ($L/L_0 = 1$) or flange with an outer diameter of 0.381 m that extended radially in the direction perpendicular to the tube's exhaust flow. A hole located in the center of the plate matched the tube's inner diameter, thus increasing the apparent wall thickness at the exhaust end from 0.0127 m to 0.1524 m. The purpose of this flange was to see if the pressure behind the diffracting shock wave would contribute significantly to the specific impulse. The second extension was a straight cylinder ($L/L_0 = 1.6$) with a length of 0.609 m. This extension simulated a partial fill case. The third extension was a diverging conical nozzle ($L/L_0 = 1.3$) with a half angle of eight degrees and a length of 0.3 m.

The flat plate and straight extension were tested with ethylene-oxygen-nitrogen mixtures in a tube that did not contain internal obstacles (Fig. 2.25 a and b). The flat plate extension yielded a maximum specific impulse increase of 5% at 0% nitrogen dilution that is within the uncertainty in measured impulse. This effect can be understood by recognizing that the flat plate or flange extension has a minimal effect on the impulse since the shock Mach number decays very quickly as the shock diffracts out from the open end. The straight extension increased the measured specific impulse by 18% at 0% nitrogen dilution, whereas a 230% increase in the specific impulse was observed at 40% nitrogen dilution. This large increase in the specific impulse occurred since the additional tube length enabled DDT to occur in the extension's confined volume.

To better isolate the effect of the extensions over the range of diluent percentages tested, cases of late or no DDT were eliminated by the addition of obstacles over half the tube length (Fig. 2.25c). The straight extension attached to a tube with internal obstacles increased the

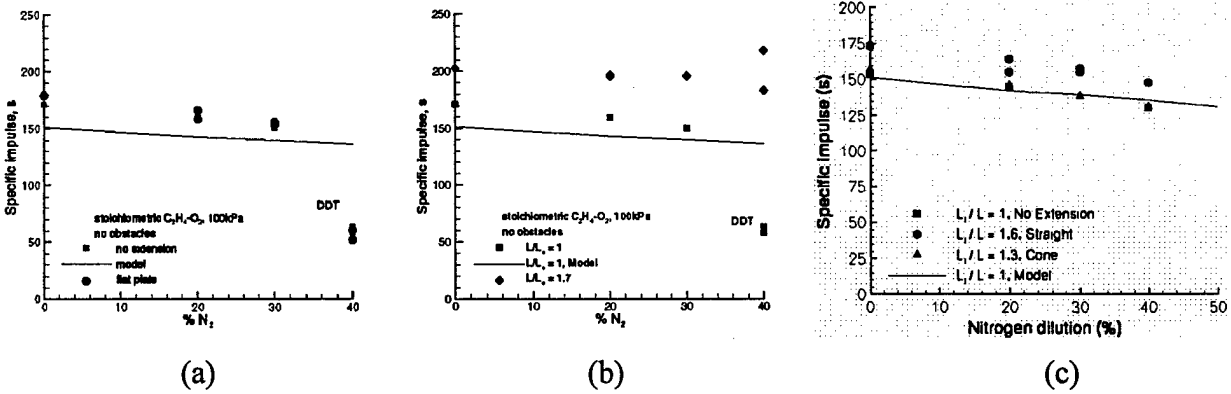


Fig. 2.25. Effect on measured impulse of different tube exit geometry.

specific impulse by an average of 13%. As shown above, the straight extension attached to a tube without internal obstacles increased the impulse by 18%. This 5% reduction in impulse is due to drag and heat transfer losses induced by the obstacles. The diverging nozzle had a minor effect, increasing the specific impulse by an average of 1%, which is within the experimental uncertainty.

The straight extension was more effective than the diverging nozzle in increasing impulse (Fig. 2.25c). One explanation [23,24] of this effect is that the additional length of the straight extension as compared with the diverging extension delays the arrival of the expansion wave from the tube exit, effectively increasing the pressure relaxation time and the impulse. Standard gas dynamics considerations indicate that two reflected waves will be created when an extension filled with inert gas is added to a detonation tube. The first wave is due to the interaction of the detonation with the mixture-air interface and is much weaker than the second wave created by the shock or detonation diffraction at the tube exit. Additionally, the continuous area change of the diverging nozzle creates expansion waves that propagate back to the thrust surface resulting in a gradual but continuous decrease in pressure that starts as soon as the detonation reaches the entrance to the diverging nozzle. Another way to interpret these impulse results with extensions is that the added inert gas provides additional tamping [25] of the explosion which will increase the momentum transfer from the detonation products to the tube.

The results of this experimental work have several significant implications for PDE technology. The use of internal obstacles may be effective in initiating detonations in highly insensitive mixtures of larger cell widths such as all the storable liquid hydrocarbon fuels. However, because there are limits to obstacle effectiveness, their use will have to be optimized

for a given mixture and application. The use of extensions may also be beneficial in augmenting the specific impulse obtainable from a given fuel-oxidizer mass. However, the maximum impulse is always obtained by filling the available tube volume entirely with the combustible mixture. Additional studies in progress are required to quantify the effect on impulse that could be obtained with diverging and converging-diverging nozzles [21].

2.2.8. Analytical Modeling of Impulse

A key issue in evaluating pulse detonation engine performance is reliable estimates of the performance as a function of operating conditions and fuel types. It is therefore desirable to develop simple analytical methods that can be used to rapidly and reliably estimate the impulse delivered by a detonation tube during one cycle. An analytical model for the impulse of a single-cycle pulse detonation tube has been developed and validated against experimental data [3]. In developing the model, the simplest configuration of a detonation tube was considered, a tube open at one end and closed at the other, and single-cycle operation. Although there are significant issues associated with inlets, valves, exits, and multi-cycle operation, it is anticipated that the simple model can be incorporated into more elaborate models that will take these features into account and that the present model will provide a key component for realistic engine performance analysis.

The model is based on the pressure history of the thrust surface (closed end) of the detonation tube (Fig. 2.26). An analysis of the gas dynamic processes inside the tube shows that the propagation of the detonation from the closed end to the open end of the tube is followed by the generation of a reflected expansion wave propagating back to the thrust surface, for all hydrocarbon-oxygen and hydrocarbon-air mixtures and most cases with hydrogen. After interacting with the Taylor wave, the reflected expansion propagates to the closed end of the tube, decreasing the pressure and accelerating the fluid towards the open end through a "blowdown" process. The pressure at the thrust surface is modeled by a constant pressure followed by a decay due to this "blowdown" process. The duration and amplitude of the constant pressure portion are determined by analyzing the gas dynamics of the self-similar flow behind a steadily-moving detonation within the tube. In particular, the constant pressure duration can be calculated by computing the trajectory of the first characteristic of the reflected

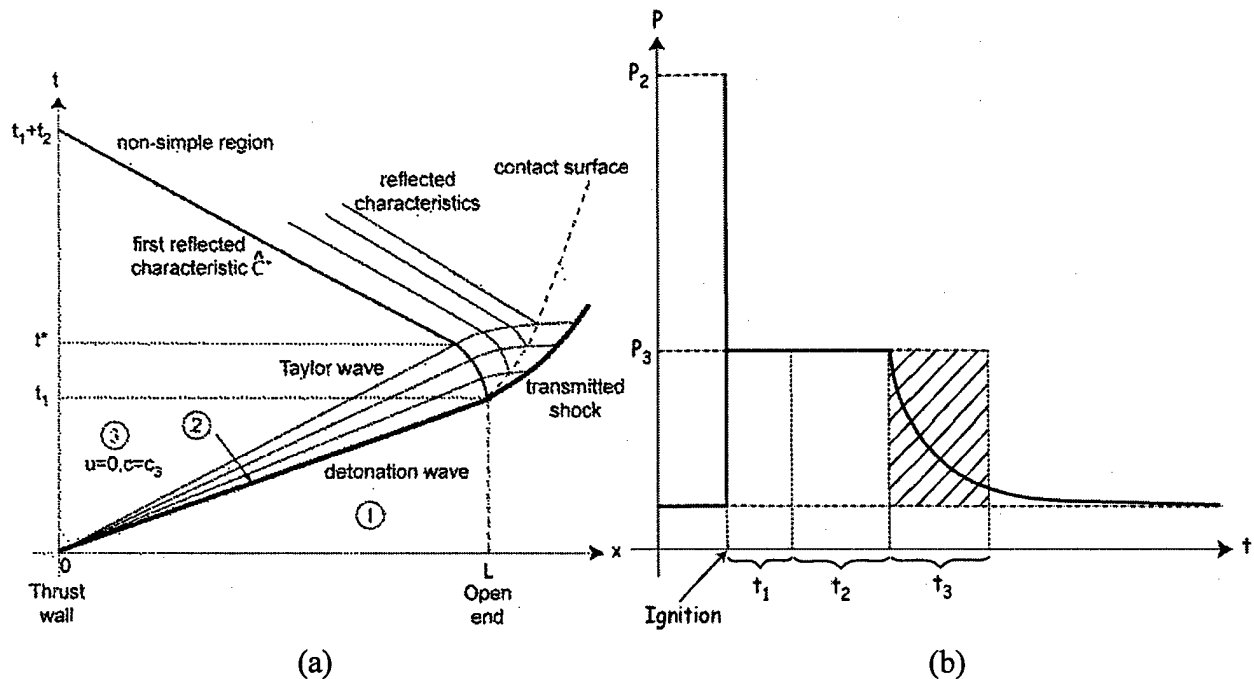


Fig. 2.26. a) Wave diagram showing the gas dynamic processes inside the detonation tube. b) Modeling of the pressure history at the thrust surface.

expansion wave. The decaying part of the pressure history, corresponding to the gas expansion process, is modeled using dimensional analysis and empirical observations.

The impulse model was validated against single-cycle experimental data obtained in the laboratory (Fig. 2.27a) [20]. Direct experimental measurements were carried out using a ballistic pendulum technique. In these experiments, detonation initiation was obtained via DDT. The agreement between the model predictions and the experimental values is better for cases with high initial pressure and no nitrogen dilution. In general, the model underpredicts the experimental values for unobstructed tubes by up to 15%, and it overpredicts them for cases when obstacles are used by up to 15%. Comparisons with multi-cycle experiments [26] were also carried out for hydrogen-air and propane-air mixtures (Fig. 2.27b). The specific impulse predictions are fairly close to the experimental data (within 8% error for hydrogen and within 15% for propane). The decrease in experimental impulse at low equivalence ratios is probably caused by cell-size effects in the case of propane and increased transition distance in the case of hydrogen. Thrust was calculated from the single-cycle impulse predictions by assuming a very simple PDE consisting of a sequence of ideal single cycles. Comparison with multi-cycle thrust measurements (Fig. 2.27c) [26] resulted in good agreement (within 4% error).

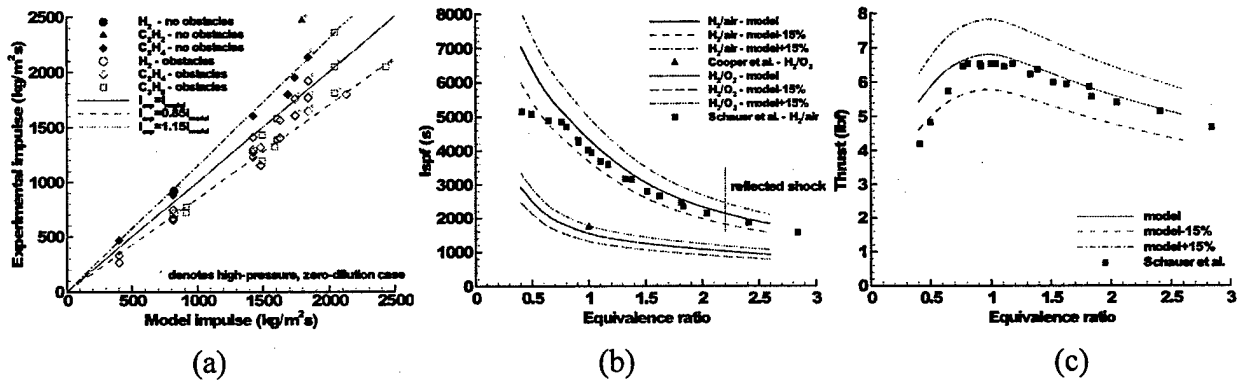


Fig. 2.27. Comparison of model impulse with a) single-cycle experiments [20] b) multi-cycle experiments [26] and c) comparison of thrust predictions with multi-cycle experiments [26].

Impulse calculations were carried out using the model for different mixtures including hydrocarbon fuels and hydrogen, and for a wide range of initial parameters including equivalence ratio, initial pressure, and nitrogen dilution (Fig. 2.28). The input required by the model consists of the outside pressure, the detonation velocity, the speed of sound behind the detonation front, the CJ pressure, and the ratio of the specific heats of the products. The impulse was calculated for the following fuels: ethylene, propane, acetylene, hydrogen, Jet A, and JP10 with varying pressure (from 0.2 to 2 bar), equivalence ratio (from 0.4 to 2.6), and nitrogen dilution (from 0 to 90%). Results were expressed in terms of impulse per unit volume of the tube, mixture-based specific impulse, and fuel-based specific impulse. The influence of the initial temperature was also investigated. The predicted values of the mixture-based specific impulse are on the order of 150 s for hydrocarbon-oxygen mixtures, 170 s for hydrogen-oxygen,

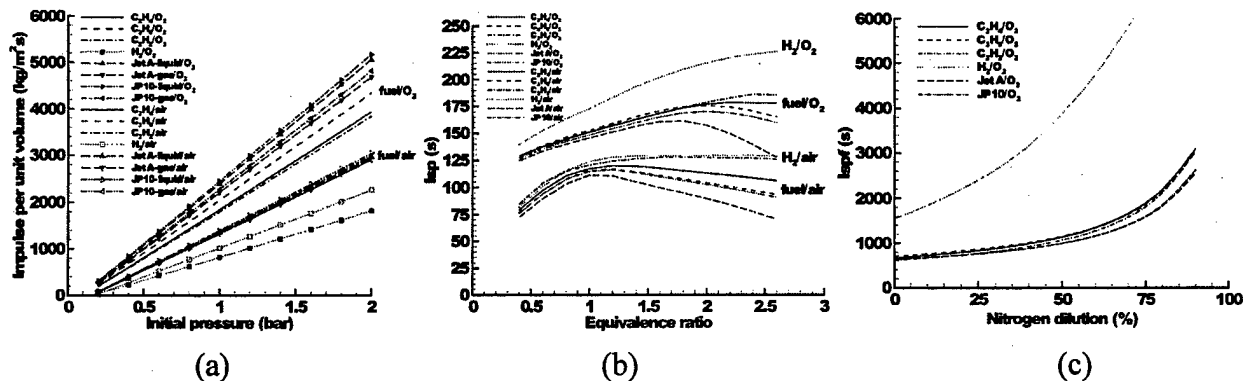


Fig. 2.28. Impulse calculations for different fuels varying initial parameters. a) impulse per unit volume varying initial pressure (stoichiometric fuel-oxygen, 300 K). b) mixture-based specific impulse varying equivalence ratio (1 bar, 300 K). c) fuel-based specific impulse varying nitrogen dilution (stoichiometric fuel-oxygen, 1 bar, 300 K).

and on the order of 115 to 130 s for fuel-air mixtures at initial conditions of 1 bar and 300 K. The trends observed are explained using a simple scaling analysis showing the dependency of the impulse on initial conditions and energy release in the mixture. The scaling relationships and equilibrium computations were used to verify the following conclusions:

1. At fixed composition and initial temperature, the impulse per unit volume varies linearly with increasing pressure.
2. At fixed composition and initial pressure, the impulse per unit volume varies inversely linearly with initial temperature.
3. At fixed composition and sufficiently high initial pressure, the specific impulse is approximately independent of initial pressure and initial temperature. This makes specific impulse the most useful parameter for estimating pulse detonation tube performance over a wide range of initial conditions.

2.3. Tube Response to Detonation Loading

The PDE is a new kind of aerospace structure that involves many challenges in repetitive, traveling, impulsive loading and thermomechanical fatigue. Studies at Caltech have investigated different aspects of this problem. The linear elastic, plastic, and fracture response of metal tubes under single-cycle shock and detonation loading have been studied.

2.3.1. Elastic Response

The traditional strategy for design of tubes under shock or gaseous detonation loading is to use linear elastic static formulas and assume a dynamic amplification factor (defined as the ratio of dynamic strain to static strain of the same pressure magnitude) of two. This model may be inadequate if the true dynamic stresses are increased due to resonance or reflection effects. It is apparent that a reliable relation between the dynamic amplification factor, the load traveling speed, and the various tube parameters should be established.

The GALCIT 280-mm stainless steel detonation tube was used to verify the existence of the critical velocity phenomenon in the linear elastic regime [27]. Strain gages were mounted on the tube, which was loaded with a range of CJ detonation speeds. Amplification factors ranging from 1 to 4 were measured, with maximum strain occurring when the CJ speed reached a critical

velocity that is a function of tube parameters. Analytical studies and transient finite element modeling were done and the results show fair agreement with experiments.

The critical velocity phenomenon was also verified with shock loading on a 52-mm aluminum tube [28]. Dynamic strains exceeding static strains by a factor of 3.5 were measured at the critical velocity. Again, analytical studies and transient finite element modeling were done and the results show reasonable agreement with experiments. This work shows that it is important to incorporate the critical velocity concept in shock and detonation tube designs.

2.3.2. Plastic Response

The study of tubes under detonation loading was extended to the plastic regime. For these experiments, a ductile material had to be used. Copper tubes were chosen, and their plastic response under detonation loading was characterized in a series of experiments at Caltech [29]. Strains exceeding the yield strain were obtained. The strain patterns observed were characterized by a large step-like response on which small-amplitude damped elastic oscillations are superimposed.

2.3.3. Fracture

If structural failure may occur, it is desirable and often possible to have benign failure rather than catastrophic failure. The use of fracture mechanics approach in structural design allows the cracks to be brought to quick arrest and prevents fragmentation. Experiments at Caltech have shown that the fracture modes in axially preflawed aluminum tubes loaded by detonations are a strong function of the initial flaw length [30]. Different fracture modes (for example, see Fig. 2.29) were observed (sometimes all on the same specimen) including short distance straight propagation, helical propagation, and bifurcation.



Fig. 2.29. Crack propagation and bifurcation under detonation loading. Detonation propagated from left to right. $P_{CJ} = 6.2$ MPa, notch length 5.08 mm.

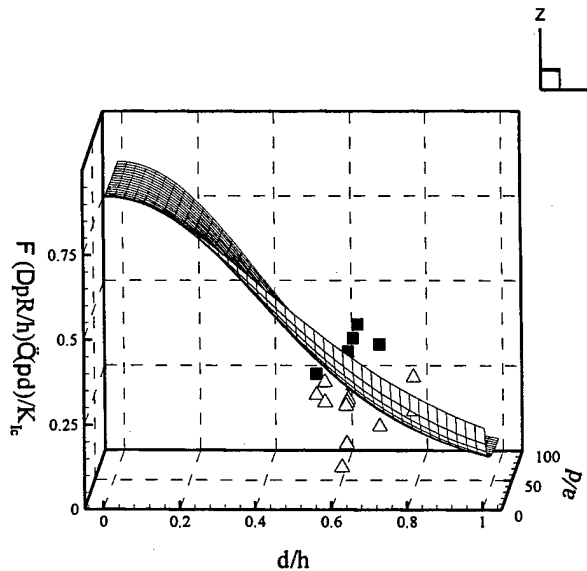


Fig. 2.30. Fracture threshold model and experimental data. Mesh surface: theoretical threshold. Filled squares: rupture. Open triangles: no rupture. Nomenclature and experimental conditions are shown in Tables 2.1 and 2.2, respectively.

Table 2.1. Nomenclature

ΔP	$P_{CJ} - P_{atm}$
R	tube mean radius
h	Tube wall thickness
d	Surface notch depth
2a	Surface notch length
K_{Ic}	Fracture toughness
Φ	Dynamic amplification factor

Table 2.2. Experimental Conditions.

Tube material	6061-T6
Wall thickness	0.89 - 1.2 mm
Tube O.D.	41.3 mm
Axial flaw length	13 to 76 mm
d/h	0.5 to 0.8
P_{CJ}	2 to 6 MPa

It is common for flaws such as voids or cracks to develop in aerospace structures during their manufacture or lifetimes. Flaws can be small and insignificant, or they can lurk until they are fatigued to a critical size, at which point the structure fails. A fracture threshold model was developed to predict the single-cycle detonation pressure at which the tubes would burst given the tube's geometry and material properties. The experimental data showed fair agreement with the model (Fig. 2.30). Strain gages were also mounted on the tubes to monitor the large scale yielding during dynamic fracture.

2.3.4. PDE Design Parameters

Critical structural and performance parameters of a conceptual PDE were studied [31]. Performance parameters included thrust specific fuel consumption (TSFC), frequency limits, and thrust-to-weight ratio. The conceptual PDE operates with stoichiometric JP10-air at standard conditions and has a design thrust of 100 N. The fixed design thrust implies a relationship between the geometrical parameters of the engine and the cycle frequency. The tube design parameters, which are the diameter d , the length L , and the cycle frequency f , are subject to

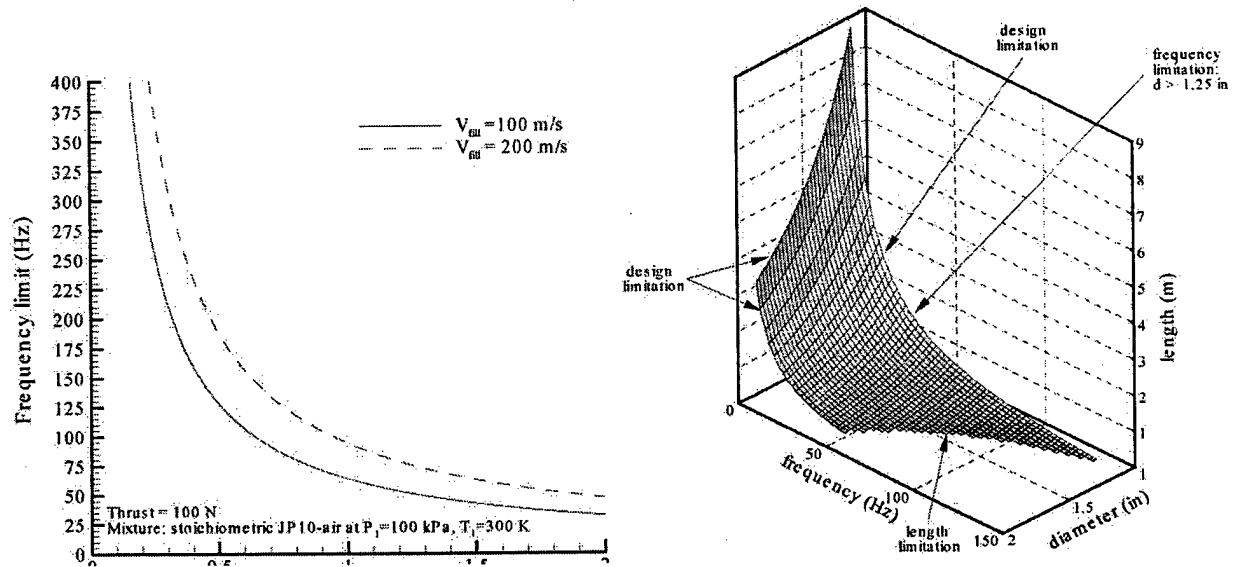


Fig. 2.31. Estimate of PDE frequency limits and PDE design surface.

constraints. These are a maximum frequency limit, which is a function of the average filling velocity, and minimum dimensions proportional to the cell width ($d > \lambda/\pi$ for propagating detonations and $L > 10\lambda$ for successful indirect detonation initiation). These relationships are summarized in a design surface in the (f, d, L) parameter space, given in Fig. 2.31. Several additional issues were identified in addition to these calculations, including frequency limits due to filling and mixing, mixture sensitivity, efficient detonation initiation, liquid fuel injection system, multi-cycle operation, drag and flow losses, and engine operational envelope.

The structural aspects include engine geometry, mass, yield stress, structural resonance due to flexural wave excitation, critical flaw size, and fracture toughness. The yield stress criterion was used to determine the minimum wall thickness of an unflawed tube for four materials: aluminum, inconel, steel, and silicone nitride. Structural resonance due to flexural wave excitation was taken into account in these calculations. Fracture mechanics was used to predict critical flaw sizes for a detonation tube (Fig. 2.32). The engine thrust-to-weight ratio was estimated based on the yield stress criterion for various tube lengths and diameters. Additional structural issues were highlighted such as impulsive thermomechanical fatigue, fracture due to single-cycle detonation loading, and plastic creep due to cyclic detonation loading.

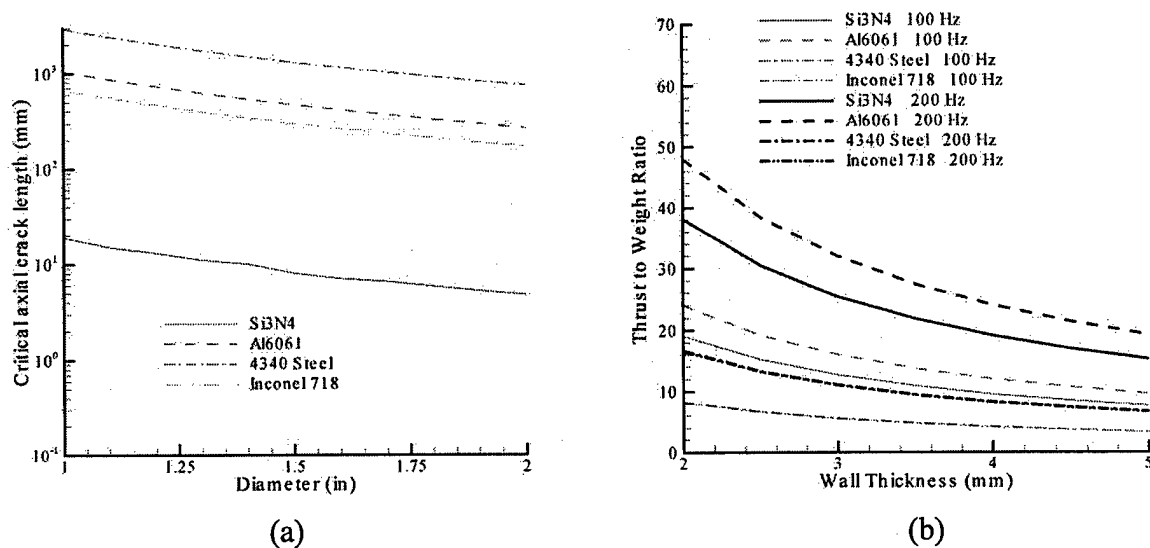


Fig. 2.32. a) Critical flaw size versus tube diameter (fixed 2-mm wall thickness) and b) thrust-to-weight ratio versus wall thickness (fixed 1.5-in tube diameter).

2.4. Summary

Caltech has investigated fundamental detonation physics, detonation initiation techniques, fuel physical properties, detonation cell widths, impulse measurements and modeling for detonation tubes, and the structural aspects of detonation tubes. Significant accomplishments include:

1. Visualization of detonation structure using PLIF in propagating detonations. Observations of "keystones" and correlation of keystones to transverse wave structure.
2. Measurement of detonation diffraction and development of a simple model for correlating critical diffraction diameter to chemical kinetic and gasdynamic properties of propagating detonations.
3. Measurement of detonation cell widths in mixtures of JP10 and air over a range of equivalence ratios, initial pressure, addition of small HC fuels.
4. Development of detonation initiation technique based on toroidal imploding waves.
5. Direct measurement of detonation tube impulse for hydrocarbon fuels using the ballistic pendulum technique.
6. Development of an analytical model for impulse from a detonation tube and validation against single-cycle and multi-cycle experiments.

7. Measurement and analysis of structural response of tubes to detonation loading, including elastic response, plastic response, and fracture thresholds.
8. Design parameter studies examining the trade-off between structural, geometrical, and combustion parameters.

The results of these studies have been documented in over 15 conference proceedings, journal publications, and Caltech technical reports. The work has been presented at international and national meetings on combustion and propulsion. The results are available on-line from the Explosion Dynamics Web page in the form of electronic documents, databases, and spreadsheets. Over eight graduate students have participated in the program, five MS projects have been performed, one PhD has been completed, and four more are in progress on topics related to PDE science and technology.

3. PRINCETON RESULTS

The research effort at Princeton has focused on detonation analysis in two areas, viz., effects of complex chemical kinetics on the induction length in C-J detonations, and heterogeneous effects in the propagation and quenching of detonations. Analysis in the first area placed emphasis on hydrogen oxidation and applications to pulse detonation engines. The problems studied included the role of branching-termination reactions on the overall reaction rate, the reduction of detailed mechanism to simpler ones without compromising comprehensiveness of description, the coupled influence of compressibility and chemical reactivity on ignition, and the use of hydrogen and ethylene as potential ignition enhancers. In the second area, the steady propagation of the 1-D detonation wave in heptane/air sprays was computationally studied using detailed chemistry, with emphasis on the effects of droplet heating, vaporization, and drag, as well as wall drag and heat loss, on the detonation velocity and quenching. The results of these analyses are presented here.

3.1. Chemical Kinetics Effects on Induction Length

Studies of the C-J detonation can be conducted at several levels of detail. At the simplest level of adiabatic propagation and downstream chemical equilibrium, the detonation velocity can be readily determined without knowledge of chemical kinetics. The predicted velocity also agrees well with experimental observations for propagation in off-limit situations [32].

Finite-rate kinetics and the associated kinetic mechanisms are however needed in the study of two aspects of detonation phenomena. The first is concerned with near-limit propagations leading to quenching of the detonation wave. The agent of quenching can be volumetric heat loss, frictional and heat loss at the wall of the detonation tube, or wave curvature. Combustion is non-adiabatic and complete reactant consumption is not achieved at the sonic state. The second is concerned with determining the ignition length for the adiabatic propagation, and using it to estimate such global flame parameters as the cell size of steady propagation and the wave curvature at quenching based on some empirical relations [33].

The simplest description of chemistry is that of one-step irreversible reaction. Elegant theories and detailed computations have been conducted on various aspects of detonation based on this assumption, and useful insights have been gained. At the same time, however, it is also recognized that such a simplification inherently cannot quantitatively describe many detonation

responses of interest, especially in view of the sensitive Arrhenius nature of the reaction rate to temperature variations. Furthermore, *ad hoc* correlations of the experimental results with adjustable kinetic parameters such as the activation energy are applicable only in limited ranges of the system and thermodynamic parameters.

What is more serious with the use of one-step chemistry is that it precludes the influence of chain branching-termination mechanisms that are invariably multi-step in nature. A prominent example is the three explosion limits of the hydrogen/oxygen system (Fig. 3.1), showing that for a homogeneous mixture at a fixed temperature, increasing the system pressure from a low value of non-explosion can render it to be explosive, non-explosive, and explosive again.

Another example is the recent observation that ignition of hydrogen and hydrocarbons can be achieved via radical proliferation instead of thermal feedback [34-35]. Such a phenomenon again cannot be described by a one-step overall reaction.

The primary objective this study is to demonstrate the intrinsic importance of chemistry, beyond that of the one-step approximation, through an induction length analysis of the CJ wave. Furthermore, for quantitative relevance, the operating parametric ranges of the pulse detonation engine (PDE) are adopted for the demonstration.

Specifically, three problems that demonstrate various aspects of chemistry on the induction length were studied. The first is an investigation of the influence of the non-monotonic explosion limits of the hydrogen/oxygen system on the induction length. The analysis yields an operation map that indicates the transition boundaries in the initial temperature (T_1), initial pressure (p_1), and fuel equivalence ratio (ϕ) space for which drastic changes in the ignition length are expected. The second explores the extent to which the detailed hydrogen/oxygen mechanism can be reduced and still maintain predictive capability. The third compares the ignition lengths of hydrogen with those of two hydrocarbon fuels, namely ethylene and heptane, and investigates the potential of using small amounts of hydrogen and ethylene as ignition enhancers.

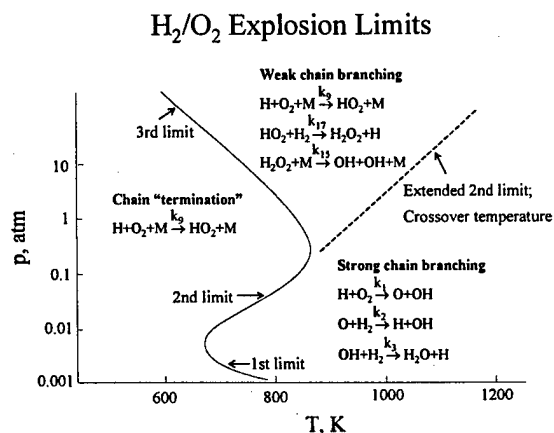


Fig. 3.1. Approximate explosion limits of hydrogen/oxygen mixtures.

The combined effects of chemistry and compressibility have been identified. These three problems are presented sequentially.

Calculation of the ignition length involved first determining the CJ velocity for the given T_1 , p_1 , and ϕ . This yields the post-shock temperature T_2 and pressure p_2 , from which the structural evolution of the post-shock homogeneous mixture undergoing chemical reaction is traced. Induction length is defined as the state at which the temperature gradient attains a maximum. For PDE and PDRE applications, an initial temperature range between 298 and 500 K, initial pressure between 0.1 and 5 atmospheres, and equivalence ratio between 0.5 and 1.5 are assigned.

The detailed oxidation reaction mechanisms for hydrogen, ethylene, and heptane are respectively taken from Refs. 36-38. Discussion on their validation and comprehensiveness can be found in the respective references.

3.1.1. Second-Limit Consideration for Hydrogen-Fueled PDE

Figure 3.1 shows a representative diagram for the explosion limits of hydrogen/air mixtures. It is seen that in the regime where the temperature is not too high, there are three explosion limits as the pressure increases. Excluding the very low pressure regime which is not of interest to PDE operations, the explosive regime above the first explosion limit is controlled by the branching and propagating reactions involving the generation of H, O, and OH radicals. The fastest and hence controlling reaction is



The rate of chain branching, however, is moderated by the chain "termination" reaction,



because the HO_2 radical produced is much less reactive than H, where M is a third body. However, with increasing pressure the collision frequency and hence rate of the three-body termination reaction (R9) greatly increases relative to that of the two-body branching reaction (R1). Consequently, at the second limit reaction (R9) becomes dominating, leading to the suppression of explosion. It can then be shown that the second limit is given by the relation

$$p = (2k_1 / k_9) R^0 T \quad (3.1)$$

where R^0 is the universal gas constant. Since k_1 and k_9 are only functions of temperature, Eq. (3.1) uniquely relates the system pressure and temperature. This relation yields the crossover temperature.

Finally, with further increase in pressure, the concentration of the relatively inactive HO_2 radicals becomes high. Their subsequent reactions with either themselves or H_2 will eventually lead to the formation of H and OH radicals, and consequently explosion beyond the third explosion limit. The overall reaction rate for these high-pressure, low-temperature situations involving the HO_2 and H_2O_2 radicals, however, are weaker than that of the low-pressure, high-temperature H-O_2 chain branching reactions.

For sufficiently high post-shock temperatures, the transition between the strong H-O_2 branching to the weak H_2O_2 branching occurs directly, without going through the non-explosive regime bounded by the first and third limits. This extended second-limit transition is now simply controlled by the crossover temperature of Eq. (3.1), as shown in Fig. 3.1.

The above discussion then implies that while the induction length is expected to decrease with increasing shock strength because of the simultaneous increase in the post-shock temperature and pressure, the presence of the pressure-sensitive but temperature-insensitive third-order termination reaction could substantially reduce the overall reaction rate. In particular, for a sufficiently weak mixture with a correspondingly low post-shock temperature and weakened temperature-sensitive branching reaction (R1), the termination reaction (R9) will exert a stronger influence. Consequently, it is reasonable to expect that the ignition length could actually increase with increasing pressure when the combustible mixture is either sufficiently fuel lean or fuel rich. To examine the above possibility, Fig. 3.2 shows the calculated ignition length for H_2/air mixtures of various equivalence ratios and initial pressures p_1 , at a fixed initial temperature (T_1) of 298 K. It is seen that, except for the strongly reacting $\phi = 1$ case, the ignition length initially decreases

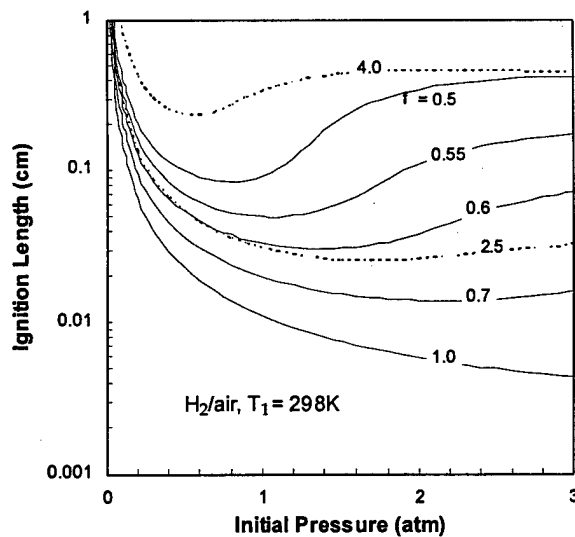


Fig. 3.2. Dependence of the ignition length of hydrogen/air mixtures on initial pressure (p_1) and equivalence ratio (ϕ).

and then increases again with increasing p_1 and hence increasing post-shock pressure p_2 . The non-monotonic trend is stronger for leaner mixtures. The essential importance of detailed chemistry, particularly the influence of chain branching and termination mechanisms, is therefore demonstrated.

As a consequence of the above result, it is prudent that operation of the PDE should avoid situations in which the post-shock temperature (T_2) and pressure (p_2) would fall above the relation for the crossover temperature, as originally noted by Shepherd [39]. Thus if Eq. (3.1) is represented as

$$p_2 = \{2k_1(T_2)/k_9(T_2)\}R^0T_2 = f(T_2) \quad (3.2)$$

while from the shock jump relations the following is obtained

$$p_2 = p_2(p_1, T_1, \phi) \quad (3.3)$$

$$T_2 = T_2(p_1, T_1, \phi) \quad (3.4)$$

for a given ϕ , then the operation boundary between slow and fast branchings in the system parameter (p_1, T_1) space can be determined.

Such a generalized, chemistry-affected operation map is shown in Fig. 3.3. For a given ϕ , operation with initial states above the transition boundaries between the slow and fast branchings should therefore be avoided.

3.1.2. Chemistry Reduction for Hydrogen Oxidation in PDE

In obtaining the above results, the hydrogen oxidation mechanism used was the detailed one, consisting of 19 steps and 8 participating species ($O_2, H_2, O, H, OH, H_2O, HO_2, H_2O_2$). While the use of such a detailed mechanism assures comprehensiveness in the description of all possible outcomes under all possible system operating conditions, the computational requirement can be rather demanding, especially for complex flows such as those involving the cellular

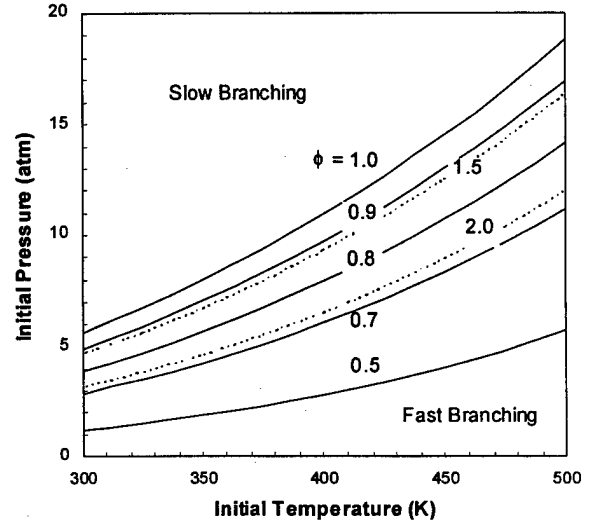


Fig. 3.3. Hydrogen/air PDE operation map showing regimes of slow and fast branching for given operating parameters T_1, p_1 , and ϕ .

detonation wave structure. Thus there is the incentive to simplify the detailed mechanism through rational approximation, without compromising the comprehensiveness of the detailed mechanism.

The particular feature of a complex chemical reaction mechanism that lends itself for approximation is the disparate time scales associated with various groups of reactions. As such, for a given phenomenon or during a particular phase in the progress of the overall reaction, either some individual reactions can be approximated to be in equilibrium, or the concentrations of some species can be approximated to be in steady state. This would reduce the number of species that needs to be solved through differential equations.

A useful algorithm for the systematic reduction of detailed mechanism is Computational Singular Perturbation (CSP) [40-41]. Using the CSP algorithm, possible reduction of the detailed hydrogen oxidation mechanism for PDE applications, as defined by the operation map of Fig. 3.3, have been examined. Since the system consists of eight participating species and two elements (O and H), the detailed mechanism can be reduced to six semi-global reaction steps without assuming any quasi-steady-state (QSS) species. Figure 3.4 shows the number of species in a reduced mechanism as a function of the threshold factor α [41], which is the ratio of the characteristic system/phenomenon time (e.g. ignition time for PDE analysis) to the characteristic, approximately e-folding, time of the species concentrations. It is obvious that the larger the α , the better is the QSS assumption for the particular species. Figure 3.4 then shows that OH has the shortest time scale, and is the best QSS candidate. A 5-step reduced mechanism can then be derived by selecting OH as the QSS species. The global reactions and reaction rate expressions for the reduced mechanisms are given in the appendix. Further reduction to a 4-step reduced mechanism, with correspondingly reduced accuracy, can be achieved by including O as a QSS species. Additional reduction would lead to substantial inaccuracies over the entire parametric

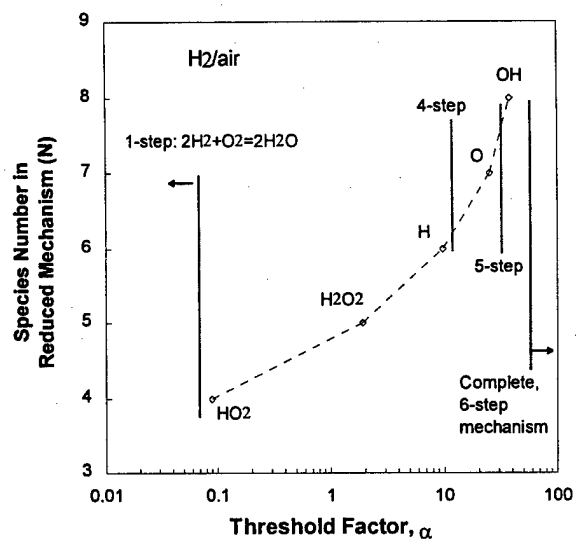


Fig. 3.4. CSP-determined dependence of the number of species in reduced mechanisms on the threshold factor α , for the ignition of hydrogen/air mixtures in PDE

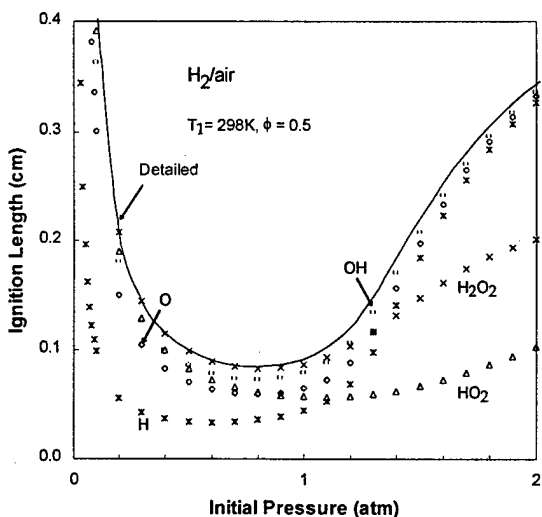


Fig. 3.5. Comparison of the calculated ignition length by using the detailed mechanism versus various 5-step mechanisms obtained by assuming one of the five radicals (H, O, OH, HO₂, H₂O₂) to be in steady state, for $\phi = 0.5$.

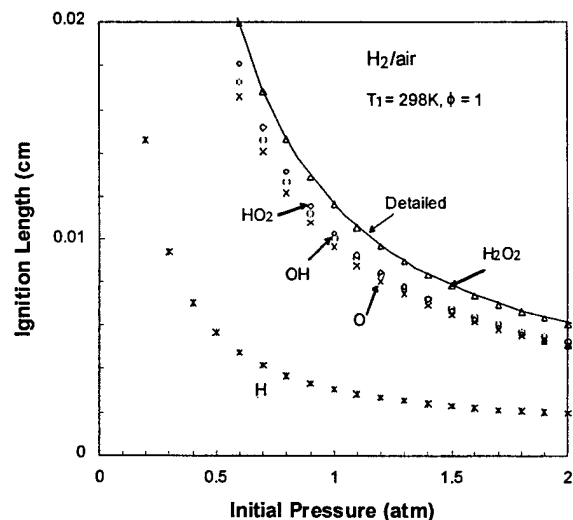


Fig. 3.6. Comparison of the calculated ignition length by using the detailed mechanism versus various 5-step mechanisms obtained by assuming one of the five radicals (H, O, OH, HO₂, H₂O₂) to be in steady state, for $\phi = 1$.

range as species with $\alpha \leq 10$ are assumed to be QSS. For reference, the 5-, 4- and 2-step reduced mechanisms are listed in the appendix.

To demonstrate the influence of each species on the system performance in terms of the extent of the quasi-steadiness, for specialized situations, the ignition lengths obtained by assuming quasi-steadiness for each species as indicated for $T_1 = 298$ K and $\phi = 0.5$ are plotted in Fig. 3.5. It is seen that the simulation of the detailed mechanism throughout the entire p_1 regime is the closest with OH being a QSS. The next best candidate is O. Both reduced mechanisms, however, show deviation from the detailed mechanism. The mechanism with H as QSS species yields significant error in low and normal pressures while mechanisms with HO₂ or H₂O₂ as QSS species give large errors in the normal and elevated pressure ranges.

Figure 3.6 shows a simulation for the strongly burning case of $\phi = 1$; similar results exist for $\phi = 1.2$. Here because of the high post-shock temperature T_2 , H₂O₂ becomes an excellent QSS candidate while HO₂, O, and OH are all satisfactory ones. For many PDE cases in which the fuel composition is close to stoichiometric, a 2-step reduced mechanism could be generated by choosing these four species to be all in QSS. However special attention is required to make sure that there will be no locally lean region in applying the 2-step reduced mechanism.

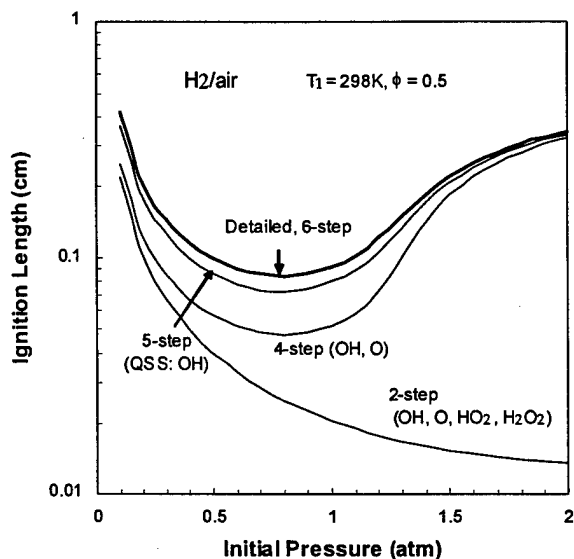


Fig. 3.7. Comparison of calculated ignition length by using detailed mechanism versus reduced mechanisms with different levels of reduction, for $\phi = 0.5$.

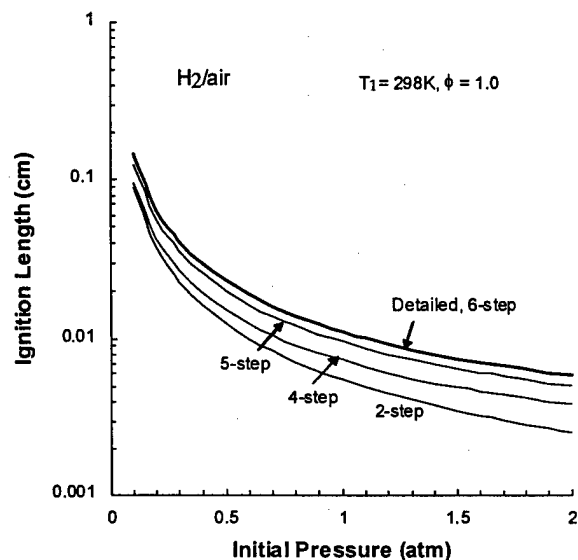


Fig. 3.8. Comparison of calculated ignition length by using detailed mechanism versus reduced mechanisms with different levels of reduction, for $\phi = 1$.

Based on the above results, ignition length as a function of p_1 has been calculated for reduced mechanisms of different sizes. Figure 3.7 shows that, for $\phi = 0.5$, the 5-step mechanism is quite satisfactory while the 4-step mechanism could also be acceptable, especially at higher initial pressures. However the 2-step reduced mechanism gives large error in moderate and high pressure. In Fig. 3.8, which is the corresponding plot for $\phi = 1.0$, it is seen that the performance of even the 2-step reduced mechanism is acceptable.

3.1.3. Ignition Lengths of Hydrogen, Ethylene, and Heptane

There are both practical and fundamental motivations in comparing the ignition characteristics of hydrogen, ethylene and heptane. Practically, hydrogen has been the fuel of choice for high-speed propulsion, while heptane is a representative liquid hydrocarbon fuel. Ethylene is a crucial reaction intermediate of higher hydrocarbons, and has been used as a surrogate fuel in the simulation of the combustion of these higher hydrocarbons. Fundamentally, these three fuels have distinctively different chemical and physical properties. Chemically, they have vastly different reactivities, with hydrogen being the most reactive and heptane the least. Physically, they have very different molecular weights and structures, which would affect the compressibility of the combustible mixture through the variation in the upstream speed of sound.

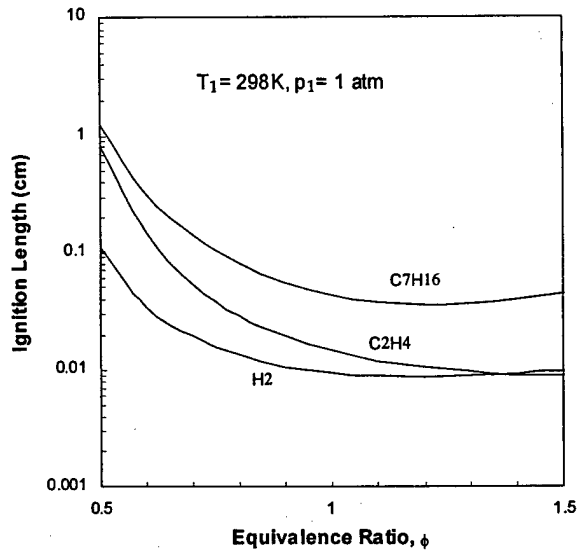


Fig. 3.9. Dependence of ignition length on equivalence ratio for hydrogen, ethylene, and heptane mixtures with air.

Figure 3.9 compares the ignition lengths of the three fuels as a function of ϕ , for fixed $T_1 = 298 \text{ K}$ and $p_1 = 1 \text{ atm}$. It is seen that, except for the fairly rich regime, the ignition length increases in the order of hydrogen, ethylene, and heptane. Furthermore, they exhibit minimum values for ϕ slightly on the rich side of stoichiometry. These trends are anticipated on the basis of chemistry, and indeed resemble those of the subsonic laminar flame burning velocity. It is, however, also of interest to note that while the ignition lengths of ethylene are closer to those of heptane for the very lean mixtures, they are closer to those of hydrogen for the rich mixtures. This is a consequence of compressibility, to be discussed next.

Figures 3.10 to 3.12 respectively show variations of the detonation velocity, upstream speed of sound, and upstream Mach number with ϕ for the three fuels. It is seen that the detonation velocity increases in the order of hydrogen, ethylene, and heptane, demonstrating the dominating influence of chemistry. However, their respective speed of sound not only varies in the opposite manner, but also shows opposite trends with ϕ , with hydrogen increasing and ethylene and heptane decreasing with increasing ϕ . These are primarily effects of molecular weight in that hydrogen is the lightest and heptane the heaviest. Furthermore, since they are respectively lighter and heavier than air, their positive and negative influences on the mixture's speed of sound increase with increasing fuel concentration and hence ϕ . The fact that the speed

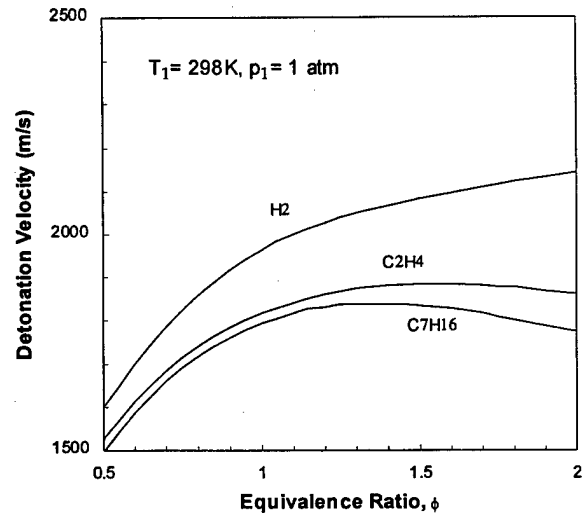


Fig. 3.10. Dependence of the CJ detonation velocity on equivalence ratio for hydrogen, ethylene, and heptane mixtures with air.

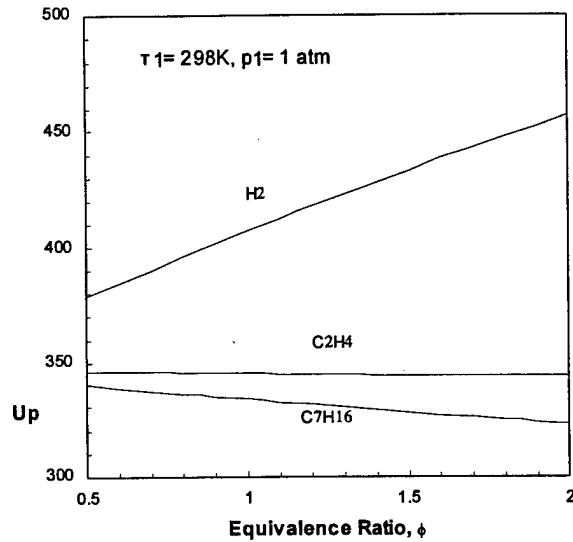


Fig. 3.11. Dependence of the upstream speed of sound on equivalence ratio for hydrogen, ethylene, and heptane mixtures with air.

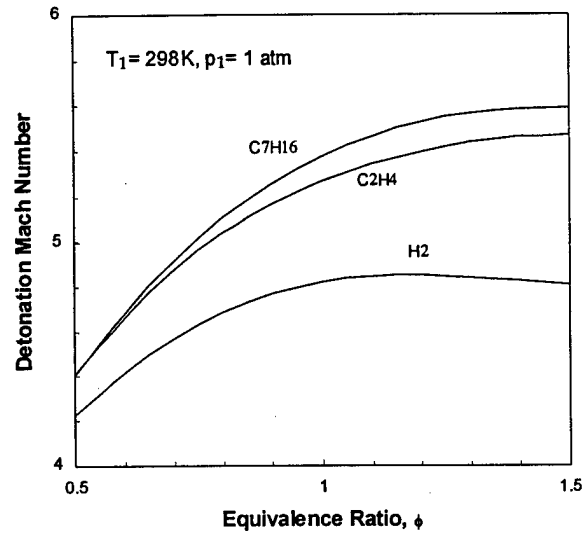


Fig. 3.12. Dependence of CJ detonation Mach number on equivalence ratio for hydrogen, ethylene, and heptane mixtures with air.

of sound of ethylene decreases with ϕ , even though its molecular weight is about the same as that of air, is probably due to its larger specific heat and hence smaller specific heat ratio γ .

Combining the results of Figs. 3.10 and 3.11, Fig. 3.12 shows that the upstream Mach numbers of the three fuels vary oppositely to their respective detonation velocities. Consequently, because of this compressibility effect, the hydrogen detonation wave has the lowest strength while that of heptane the strongest. Such a trend is then directly translated into the behavior of the post-shock temperature and pressure, as shown in Figs. 3.13 and 3.14. Consequently, the hydrogen mixture has a chemically weaker post-shock environment to achieve ignition than the ethylene and heptane mixtures. Referring back to Fig. 3.9, it is now clear that while hydrogen still has the shortest ignition length, its strong chemistry has been moderated by compressibility.

3.1.4. Hydrogen, Ethylene, and Oxygen as Additives

Because of the strong reactivity of hydrogen and ethylene, it has been suggested that they can be used as additives to reduce the ignition lengths of hydrocarbon fuels. However, in light of the negative compressibility effect identified above, it is not clear if the benefit of enhanced reactivity can be readily realized.

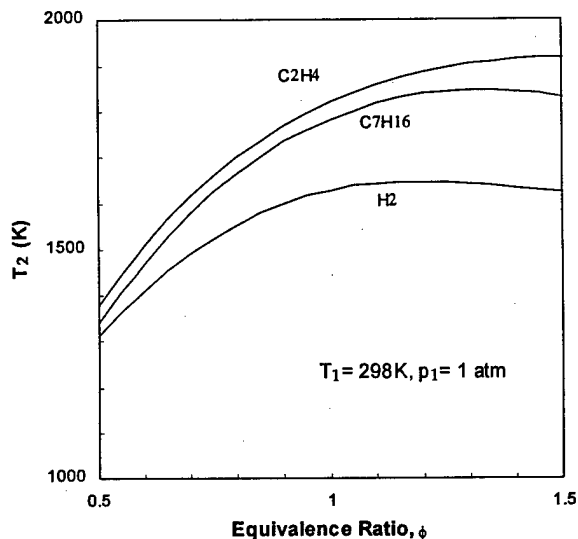


Fig. 3.13. Dependence of post-shock temperature T_2 on equivalence ratio for hydrogen, ethylene, and heptane mixtures with air.

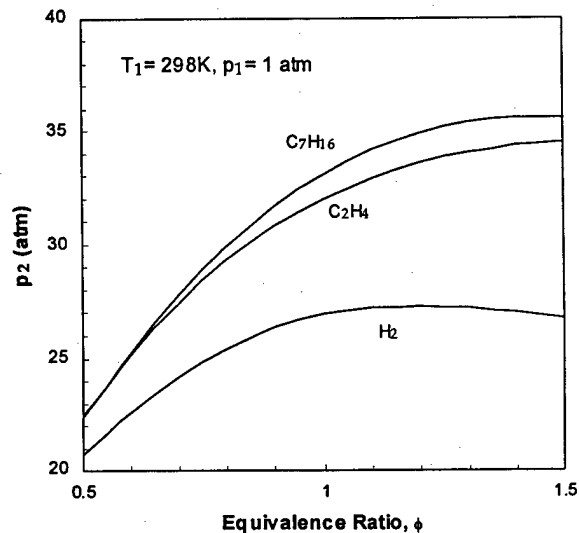


Fig. 3.14. Dependence of post-shock pressure on equivalence ratio for hydrogen, ethylene, and heptane mixtures with air.

Figure 3.15 shows the ignition lengths of mixtures of ethylene and hydrogen, and heptane and hydrogen. The results clearly show that, because of the influence of compressibility, addition of small amounts of hydrogen to either ethylene or heptane as an ignition enhancer actually has the opposite effect of increasing the ignition length. Indeed, Fig. 3.15 shows that the ignition length assumes a maximum for mixtures that have about equal concentrations of hydrogen and the hydrocarbons. This demonstrates that the ignition length is increased from the pure hydrocarbon limit due to hydrogen compressibility, and from the pure hydrogen limit due to the reduced reactivity of the hydrocarbon. Thus mixtures of hydrogen and hydrocarbons have longer ignition delays as compared to those of the more abundant component.

Figure 3.16 shows the ignition length of mixtures of ethylene and heptane. Since compressibility effect is minimized here, it is seen that doping heptane by the more reactive ethylene indeed has the beneficial effect of reducing the ignition length. At present it is not clear whether compressibility will again become important when ethylene is doped in a hydrocarbon that has a higher molecular weight than heptane, such as decane or dodecane which are representative of JP fuels. Such an assessment requires the availability of reaction mechanisms of these large hydrocarbon fuels.

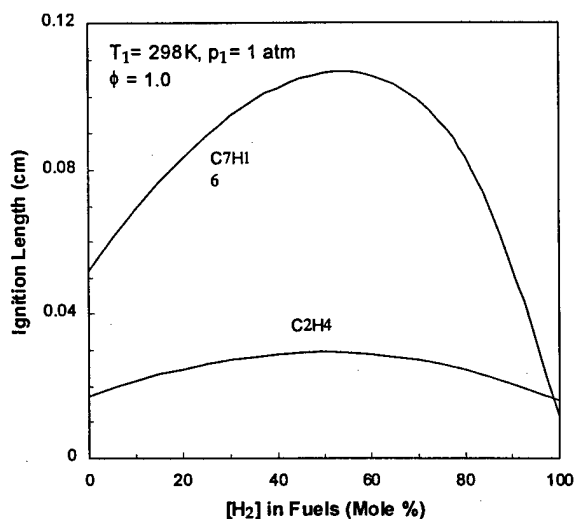


Fig. 3.15. Ignition length for ethylene/air and heptane/air mixtures with various amount of hydrogen addition.

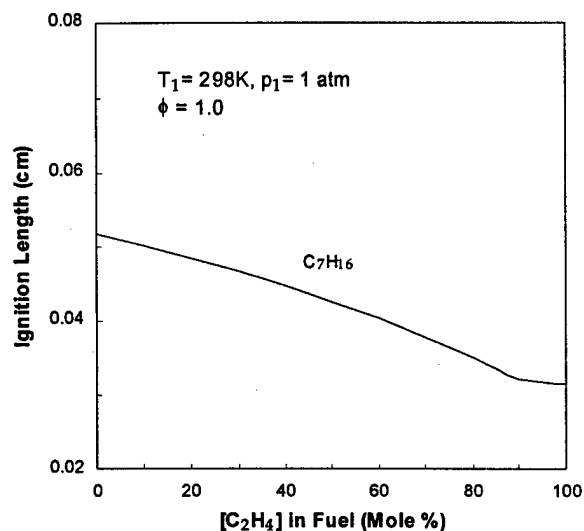


Fig. 3.16. Ignition length for heptane/air mixtures with various amount of ethylene addition.

Finally, Fig. 3.17 shows the effect of increasing the oxygen content of “air” by replacing part of its nitrogen by an equal amount of oxygen. The substantial reduction in the ignition length for all fuels with even a small amount of oxygen enrichment is quite evident.

3.1.5. Summary

In this area of study, several chemistry-related issues on the structure and propagation of detonation waves have been investigated. While the vehicle of study is the ignition length of the C-J wave, and the numerical calculations were conducted for system parameters of interest to PDE applications, the concepts and order of magnitude effects identified are expected to be of general utility.

Specifically, it was convincingly demonstrated that for hydrogen oxidation, the important role of branching-termination chain mechanisms in the overall reaction rate, and that increasing pressure could actually moderate its progress. The concept of crossover temperature was applied to derive an operation boundary in terms of p_1 , T_1 , and ϕ in order to avoid operation regimes for which the ignition length could become excessively long.

The potential reduction of the detailed hydrogen/oxygen reaction mechanism to simpler schemes suitable for integration into large-scale computations has also been investigated. Results demonstrate that, because of the relatively small numbers of species and reactions

associated with the H_2/O_2 mechanism as compared to those of hydrocarbon oxidation, only a minimal reduction is possible in that the existing detailed mechanism is probably already almost the smallest for a comprehensive description of hydrogen oxidation. The potential utility of a 2-step mechanism for near-stoichiometric operations is however noted.

By comparing the ignition lengths of hydrogen with those of ethylene and heptane, which are representative hydrocarbon fuels, the effect of compressibility through the upstream speed of sound and Mach number is identified, showing that the potential benefit of the high reactivity of hydrogen is moderated by its lower Mach number and hence lower post-shock temperature and pressure. This negative compressibility effect also indicates that using hydrogen as an ignition enhancer for hydrocarbon fuels could actually prolong the ignition delay.

3.2. Propagation and Quenching of Spray Detonations

While much has been learned about the initiation and steady propagation of spray detonations [42-44], corresponding studies on quenching have been relatively few. It is well established that when there is no loss of energy or momentum, the Chapman-Jouget detonation velocity is independent of the detonation structure and is determined by the initial conditions alone [32]. Furthermore, the adiabatic C-J velocity of spray detonation is only slightly lower than that of the corresponding gaseous detonation [45]. However, when loss occurs, the velocity deficit can become substantial and an analysis of the detonation structure is required for the determination of the detonation velocity [46]. In particular, detonation in a gaseous mixture with loss was numerically studied using detailed chemistry [47] and analyzed with a one-step overall reaction [46-49]. Sources of loss include the friction and heat loss to the wall of the detonation tube, and the curvature effect for a freely expanding wave. Results showed that the reduction in detonation velocity is proportional to the induction length and the intensity of the loss during the

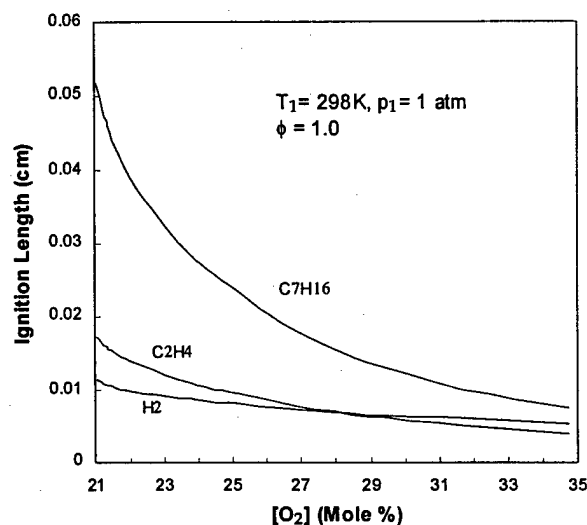


Fig. 3.17. Ignition length for hydrogen/air, ethylene/air and heptane/air mixtures with various amount of oxygen addition.

induction period preceding the state of ignition runaway. Characteristic extinction turning points were obtained [46], yielding a definitive identification of the state beyond which steady propagation of the detonation is not possible.

The effects of the induction length and loss on detonation in sprays are expected to be more complex, and thereby interesting, primarily due to the additional processes of droplet drag, heating and vaporization. Sichel and co-workers [50,51] analyzed the structure of two-phase detonations with heterogeneous reactions, while Ju and Law [49] studied two-phase detonation quenching with substantial particle heating and loss. For spray detonation, the high volatility of the liquid can render strong coupling between vaporization and ignition runaway in that vaporization simultaneously lowers the temperature of the induction region and enriches it with fuel vapor [52,53]. The former tends to retard the reaction rate and increase the induction length while the latter facilitates ignition. It is also of interest to distinguish between loss processes that are internal and external to the spray interior. The "losses" from the gas phase due to droplet drag, heating, and vaporization will be returned to it when the droplets are completely vaporized, and as such can be considered to be internal losses [54]. On the other hand, losses due to wall drag, heat transfer, and incomplete vaporization beyond the sonic state are external and hence permanent. As a result, the effects of droplet drag and vaporization on the detonation velocity and quenching limit can be quite different from those due to the external losses.

Recognizing the importance of droplet vaporization on spray detonation through its coupling with chemistry, the present work computationally solved the structure of the 1-D, steady heptane/air spray detonation, with simultaneous determination of detonation velocity and the state of quenching. The interest is in the dependence of these responses on the various spray parameters such as droplet size, loading, number density, drag, and vaporization rate. The aim of the exploration is to be reasonably realistic with respect to the thermochemical aspects of the detonation process. Consequently, heptane was chosen because it is probably the only hydrocarbon whose gas-phase chemistry and droplet vaporization process have been studied extensively. Thus there is a reasonable measure of confidence in the use of the detailed reaction and droplet vaporization mechanisms developed. On the other hand, super-critical "gasification" and post-shock droplet shattering are not included. Consequently, high initial and hence post-shock pressures are not involved so that the post-shock environment is sufficiently sub-critical. Furthermore, the initial droplet sizes are restricted to sufficiently small values so as to avoid

severe droplet distortion and shattering. Suffice to note that the initial pressure used in the present simulation, 0.5 atmosphere, is realistic for aero-engine applications and is close to atmospheric pressure under which most explosions take place. Regarding the initial droplet size, it is restricted to at most 20 μm , noting the observation of Eidelman and Burcat [55] that shattering occurs for droplet diameters between 50 and 800 μm . Finally, the 3-D cellular structure of the detonation is not considered, recognizing that a 3-D simulation would bring the computational effort to a much higher level of involvement, which would require the concomitant simplification of other aspects of the model such as the chemistry. Furthermore, useful information can be gained from a 1-D analysis of the present nature, as exemplified by Zeldovich's gas-phase analysis of the quenching of the gaseous detonation [46].

The problem is formulated in the next section, which is followed by presentation of the computed results on the effects of droplet size and pre-vaporization on detonation propagation and quenching.

3.2.1. Formulation

In the detonation stationary frame, a monodisperse spray of initial temperature T_1 , pressure p_1 , (total) fuel-to-air equivalence ratio (ϕ), and droplet radius $r_{d,0}$, passes through an infinitesimally thin shock. The initial mass fraction of the liquid fuel to the total fuel is designated by the droplet loading, α . Upon crossing the shock, the droplets of initial velocity D , which is the detonation velocity, are dragged to slow down and also start to vaporize. Individual droplet burning is not expected because of the very small droplet sizes of interest [56]. Chemical reaction therefore takes place only in the bulk gaseous medium, downstream of the shock, and runs away after an induction period.

The propagation is assumed to take place in a tube, and the detonation wave loses momentum and energy due to viscous drag and heat transfer through the tube wall. With sufficiently strong loss, chemical runaway cannot accelerate the flow to the sonic state and steady propagation is not possible. Since the analysis is a steady state one, the solution yields the detonation velocity D when steady propagation is thermochemically possible. The state beyond which such propagation is not possible then yields the state of quenching.

The steady state governing equations for mass, momentum, species, energy, droplet size, and droplet number density for the 1-D planar detonation wave in a single-fuel, monodisperse spray are given by:

$$\frac{d}{dx}(\rho_g u_g) = \dot{m}_v, \quad \frac{d}{dx}(\rho_d n_d \frac{4}{3} \pi r_d^3 u_d) = -\dot{m}_v \quad (3.5), (3.6)$$

$$\frac{d}{dx}(n_d u_d) = 0, \quad \frac{d}{dx}(\rho_g u_g Y_{g,k}) = \omega_k W_k + \dot{m}_v Y_{d,k} \quad (3.7), (3.8)$$

$$\frac{d}{dx}(p + \rho_g u_g^2) = f_d + f_w + \dot{m}_v u_d \quad (3.9)$$

$$\frac{d}{dx}(\rho_d n_d \frac{4}{3} \pi r_d^3 u_d^2) = -f_d - \dot{m}_v u_d \quad (3.10)$$

$$\frac{d}{dx} \left[\rho_g u_g \left(h_g + \frac{u_g^2}{2} \right) \right] = f_w D - q_w + f_d u_d - q_d + \dot{m}_v \left(h_{g,f} + \frac{u_d^2}{2} \right) \quad (3.11)$$

$$\frac{d}{dx} \left[\rho_d n_d \left(\frac{4}{3} \pi r_d^3 \right) u_d \left(h_d + \frac{u_d^2}{2} \right) \right] = q_d - f_d u_d - \dot{m}_v \left(h_{g,f} + \frac{u_d^2}{2} \right) \quad (3.12)$$

where $h_{g,f} = h_{g,f}(T_d)$ and T_d is the droplet temperature which is assumed to be uniform. Furthermore, ρ is the density, u the velocity relative to the shock, n_d the droplet number density, r_d the droplet radius, \dot{m}_v the mass vaporization rate of the droplets, Y the mass fraction, ω the molar reaction rate, W the molecular weight, f_d the droplet drag, f_w the wall drag, D the detonation velocity, q_w the heat loss to the wall, q_d the heat flux for droplet heating, h the enthalpy, and the subscript g denotes properties of the gas phase, d properties of the droplet, k the k th species, w the wall, and f the fuel.

The above equations are to be solved subject to the following auxiliary relations:

$$h_g = \sum_{k=1}^K h_{g,k} Y_{g,k}, \quad h_{g,k} = (h_{g,k})_0 + \int_0^T c_{pg,k} dT_g, \quad p = \rho_g R_g T_g \quad (3.13), (3.14), (3.15)$$

$$f_d = n_d C_{D,d} (4\pi r_d^2) \rho_g |u_d - u_g| (u_d - u_g) / 2 \quad (3.16)$$

$$C_{D,d} = 22 \text{Re}_d^{-1} (1 + 0.276 \text{Re}_d^{1/2} \text{Pr}^{1/3}) \quad (3.17)$$

$$f_w = C_{D,w} (P/A) \rho_g |D - u_g| (D - u_g) / 2 \quad (3.18)$$

$$q_w = C_{H,w} (P/A) |D - u_g| \lambda_g (T_g - T_w) \quad (3.19)$$

where c_p is the specific heat, R_g the universal gas constant, $C_{D,d}$ the drag coefficient [52], Pr the Prandtl number, P and A the perimeter and area of the tube respectively, $C_{D,w}$ and $C_{H,w}$ the drag and heat transfer coefficients of the wall respectively, Re the Reynolds number, and λ_g the heat conductivity of gas.

In specifying the droplet vaporization process, it is noted that because of the high temperature and pressure of the post-shock state, droplet heating is expected to be important. Furthermore, the high post-shock pressure and the low droplet temperature immediately downstream of the shock imply the potential of fuel vapor condensation onto the droplet. As such, the droplet vaporization, condensation, and heating processes need to be described reasonably realistically [56] instead of following the simple d^2 -law with a constant gasification coefficient. Consequently, the following relations describe droplet heating and vaporization:

$$\dot{m}_v = n_d(4\pi r_d) \frac{\lambda_g}{(Le)c_{p,g}} \ln(1+B_Y)(1+0.276 Re_d^{1/2} Pr^{1/3}) \quad (3.20)$$

$$q_d = n_d(4\pi r_d) \frac{\lambda_g}{c_{p,g}} \ln(1+B_H)(1+0.276 Re_d^{1/2} Pr^{1/3})L \quad (3.21)$$

$$Le = \frac{\lambda_g}{\rho_g c_{p,g} D_g}, \quad B_Y = \frac{Y_{f,s} - Y_f}{1 - Y_{f,s}}, \quad B_H = \frac{c_{p,g}(T_g - T_d)}{L} \quad (3.22)$$

$$Y_{f,s} = Y_{f,s}(p, T_d) \quad (3.23)$$

where the subscript s denotes the droplet surface, L the latent heat of vaporization, and D_g the mass diffusivity of gas. It is seen that the droplet vaporization rate is controlled by the vapor pressure gradient and the heat flux at the droplet surface. Equation (3.23) relates the surface vapor pressure with the droplet temperature, and in the present study is given by the Antoine equation [57]:

$$\log_{10}(p_{f,s}) = A - \frac{B}{T_d + C} \quad (3.24)$$

where $p_{f,s}$ is the fuel vapor pressure at the droplet surface, and A , B and C are empirically determined constants. Finally the fuel mass fraction $Y_{f,s}$ and $p_{f,s}$ are related through

$$Y_{f,s} = \frac{X_{f,s}W_f}{X_{f,s}W_f + (1-X_{f,s})\overline{W}_{g,\bar{j}}}, \quad X_{f,s} = \frac{p_{f,s}}{p} \quad (3.25)$$

where $\overline{W}_{g,\bar{j}}$ is the mean molecular weight of the gaseous mixture without the fuel.

From the governing equations of motion, evolution of the flow variables are given by:

$$\frac{du_g}{dx} = \frac{(\gamma-1)M^2 S}{(M^2-1)\rho_g u_g^2} \quad (3.26)$$

$$S = f_w \left(\frac{\gamma}{\gamma-1} u_g - D \right) + q_w + f_d \left(\frac{\gamma}{\gamma-1} u_g - u_d \right) + q_d + \sum_{k=1}^K \left[(h_{g,k} - c_{p,g} T_g \frac{\overline{W}_g}{W_k}) \omega_k W_k \right] \quad (3.27)$$

$$+ \dot{m}_v \left\{ \frac{\gamma}{\gamma-1} u_g (u_d - u_g) - c_{p,g} T_g \frac{\overline{W}_g}{W_f} - \frac{(u_d^2 - u_g^2)}{2} + [h_{g,f}(T_g) - h_{g,f}(T_d)] \right\}$$

$$\frac{dT_g}{dx} = -\frac{u_g}{c_{p,g}} \frac{du_g}{dx} + \frac{1}{\rho_g u_g^2} \left\{ f_w D + f_p u_d - \sum_{k=1}^K h_{g,k} \omega_k W_k - q_w - q_d + \dot{m}_v \left[\frac{u_d^2 - u_g^2}{2} - h_{g,f}(T_g) + h_{g,f}(T_d) \right] \right\} \quad (3.28)$$

$$\frac{d\rho_g}{dx} = -\frac{\rho_g}{u_g} \frac{du_g}{dx} + \frac{\dot{m}_v}{u_g}, \quad \frac{dr_d}{dx} = -\frac{\dot{m}_v}{\rho_d 4\pi r_d^2 n_d u_d} \quad (3.29), (3.30)$$

$$\frac{du_d}{dx} = -\frac{f_d}{\rho_d n_d \frac{4}{3} \pi r_d^3 u_d}, \quad \frac{dT_d}{dx} = \frac{q_d - \dot{m}_v L}{\rho_d n_d \frac{4}{3} \pi r_d^3 u_d c_{v,d}} \quad (3.31), (3.32)$$

$$\frac{dY_{g,k}}{dx} = \frac{1}{\rho_g u_g} [\omega_k W_k + \dot{m}_v (Y_{d,k} - Y_{g,k})] \quad (3.33)$$

where M and \overline{W}_g are the Mach number and average molecular weight of the gas mixture.

The parameter S in the numerator of Eq. (3.26) consists of the energy source/sink terms due to wall drag, wall heat loss, droplet drag, droplet heat loss, chemical reaction, and vaporization respectively. The detonation velocity D is the eigenvalue of this problem and can be obtained by matching the sonic point ($M \rightarrow 1$) and the point where all energy source terms balance ($S \rightarrow 0$), which is the downstream boundary condition [46].

Since all the parameters of the mixture ahead of the shock are known, the post-shock parameters can be solved using the normal shock relations, with the assumption that the droplets maintain the same velocity and temperature in crossing the shock:

$$\rho_{g,1} u_{g,1} = \rho_{g,2} u_{g,2} \quad (3.34)$$

$$p_1 + \rho_{g,1} u_{g,1}^2 = p_2 + \rho_{g,2} u_{g,2}^2 \quad (3.35)$$

$$h_{g,1} + \frac{1}{2} u_{g,1}^2 = h_{g,2} + \frac{1}{2} u_{g,2}^2 \quad (3.36)$$

where the subscripts 1 and 2 respectively denote parameters before and immediately after the shock. The post-shock parameters are used as the initial conditions of the above ODE's.

3.2.2. Results and Discussion

The above equations were solved numerically with detailed reaction mechanism [58] and transport. The parameters in Eq. (3.24) were: $A = 4.02832$, $B = 1268.636$, $C = -56.199$, with T_d and $p_{f,s}$ having the units of K and bar respectively [57]. The tube diameter was 38.1 mm, and the wall heat loss coefficient was $C_{H,W} = 0 \sim 0.01$. Finally, Le and Pr were set to 1 and 0.72, respectively.

Extensive exploration of the various parameters and sub-processes of the spray detonation structure and propagation showed two aspects of the detonation dynamics which are rather interesting and not readily anticipated, namely the effects of droplet size and pre-vaporization on detonation propagation and quenching. They are discussed in the following.

3.2.2.1. Effects of Droplet Size

The dependence of the computed detonation velocity on the wall drag coefficient is shown in Fig. 3.18 for different droplet sizes and heat loss coefficients, with the initial conditions being $T_1 = 298.15$ K, $p_1 = 0.5$ atm, $\phi = 1$ and $\alpha = 1$, and $C_{H,W} = 0$ and 0.01 for Fig. 3.18a and 3.18b respectively.

Figure 3.18a shows that, as the drag coefficient approaches zero such that the system becomes lossless and corresponds to the CJ limit, the detonation velocity becomes progressively independent of the droplet size. Since droplet drag and heating still occur for vanishing wall drag, the present result that the detonation velocity approaches the CJ velocity substantiates the concept that these "loss" processes are internal to the spray. That is, the loss is temporary and is re-captured by the gas as long as droplet vaporization is completed before the sonic point. Consequently, internal loss alone cannot extinguish a detonation wave.

When wall drag is allowed, this "external" loss prolongs the ignition delay [46]. The lengthened ignition delay then leads to a corresponding increase in the integrated loss due to

wall drag. This reduces the detonation velocity, weakens the shock strength, and further increases the ignition delay. It is then clear that this nonlinear feedback mechanism could lead to detonation quenching. Consequently, for a given droplet size, the detonation velocity (on the upper branch of the solution curve) decreases with increasing drag coefficient until the wave is quenched at the turning point of the response curve, in accordance with the concept of Zeldovich [46] in identifying the turning point as the state of quenching.

The presence of droplet vaporization cools the gas and thereby further aggravates and sensitizes the ignition kinetics. However, unlike the case of particle-laden detonation [49], for which the extent of reduction in detonation velocity increases monotonically with decreasing particle size, the variation is non-monotonic for spray detonation. The quenching limit also shows a non-monotonic dependence on the droplet size. Specifically, it is seen that, for a fixed wall drag coefficient, the detonation velocity first increases as the droplet size increases, reaches a maximum value at a certain droplet size, and then decreases as the droplet size further increases.

A similar result is shown in Fig. 3.18b for the non-adiabatic situations, with $C_{H,W} = 0.01$. It is seen that the quenching limits for the non-adiabatic curves in terms of, say, the wall drag coefficient, are much lower than those of the adiabatic cases due to heat loss to the wall. Furthermore, while detonation for droplet size less than $3 \mu\text{m}$ is beyond the quenching limit for the moderate wall drag coefficient of 0.01, propagation is facilitated for mixtures with larger droplet sizes.

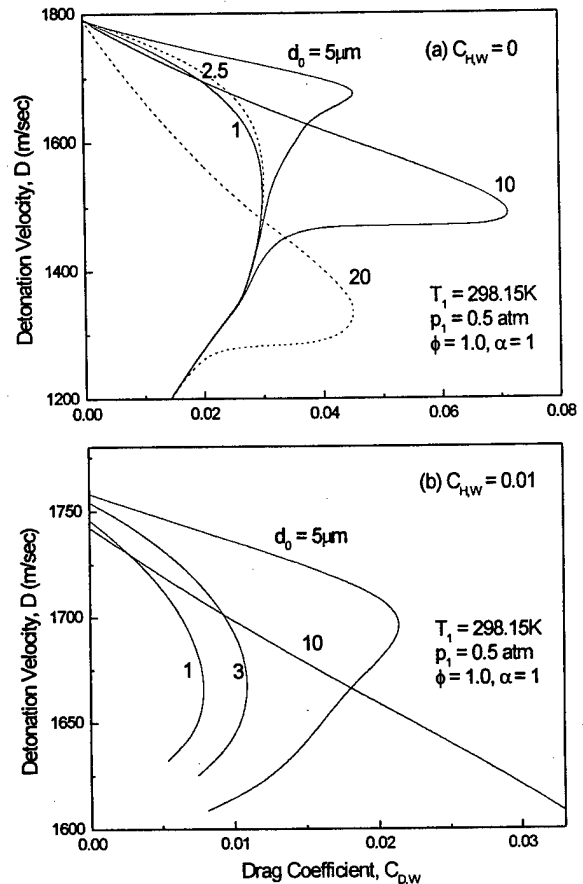


Fig. 3.18. Dependence of detonation velocity on wall drag coefficient and droplet size for stoichiometric heptane/air spray mixture, with liquid fuel loading (defined to be the fraction of total fuel in liquid phase) $\alpha = 1$, initial temperature 298.15 K and initial pressure 0.5 atm. (a) $C_{H,W} = 0$; (b) $C_{H,W} = 0.01$.

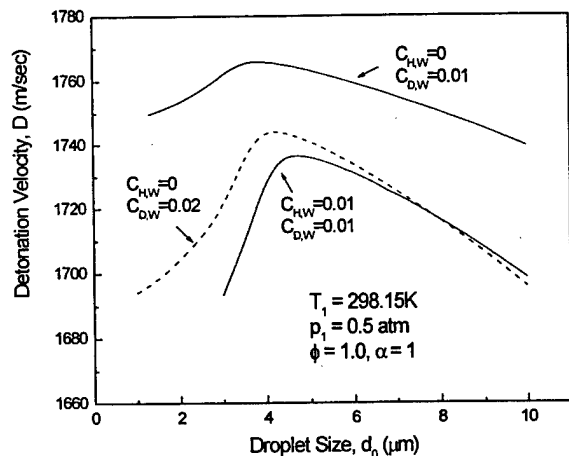


Fig. 3.19. Dependence of detonation velocity on droplet size with different wall drag coefficient and wall heat loss coefficient, for stoichiometric heptane/air spray mixture, with liquid fuel loading $\alpha = 1$, initial temperature 298.15 K and initial pressure 0.5 atm.

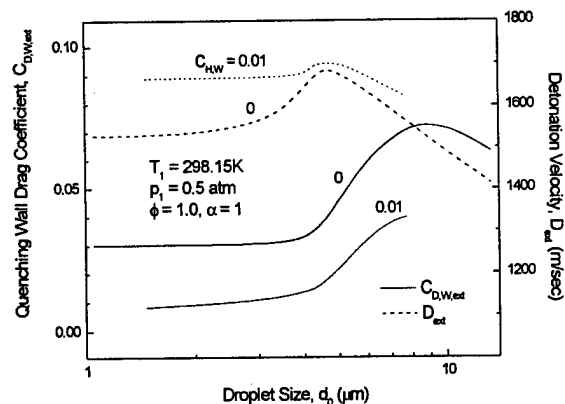


Fig. 3.20. Dependence of quenching wall drag coefficient and the corresponding detonation velocity at the quenching point on droplet size, for stoichiometric heptane/air spray mixture with different wall heat loss coefficients, for liquid fuel loading $\alpha = 1$, initial temperature 298.15 K and initial pressure 0.5 atm.

The above non-adiabatic behavior is demonstrated more clearly in Figs. 3.19 and 3.20. Specifically, Fig. 3.19 shows the non-monotonic variation of the detonation velocity with the droplet size for various drag and heat loss coefficients, demonstrating the existence of an optimum droplet size for maximum detonation velocity. Figure 3.20 plots the detonation velocity and the corresponding drag coefficient at the quenching state, designated by the subscript “*ext*”, and again shows the non-monotonic variation as well as the existence of an optimum droplet size for enhanced detonability.

The reason for this non-monotonic response is shown in Figs. 3.21 and 3.22, in which the detonation structure in terms of the gas temperature and the droplet number density, size and vaporization rate for different initial droplet sizes are compared. Small droplets, with initial diameter of 1 μm are considered first. It is seen that the droplet number density continuously increases as the shocked gas flows downstream (Fig. 3.22a). This increase is caused by the drag acting on the droplet, rendering the flow to become more concentrated with droplets as it travels downstream. This point is demonstrated in Fig. 3.21a, which shows that shortly downstream of the shock, some chemical reaction is initiated, as indicated by the slight rise in the gas temperature. Since the fuel initially is totally in the form of droplets ($\alpha = 1$), the amount of fuel participating in this reaction is all supplied by droplet vaporization. However, due to the

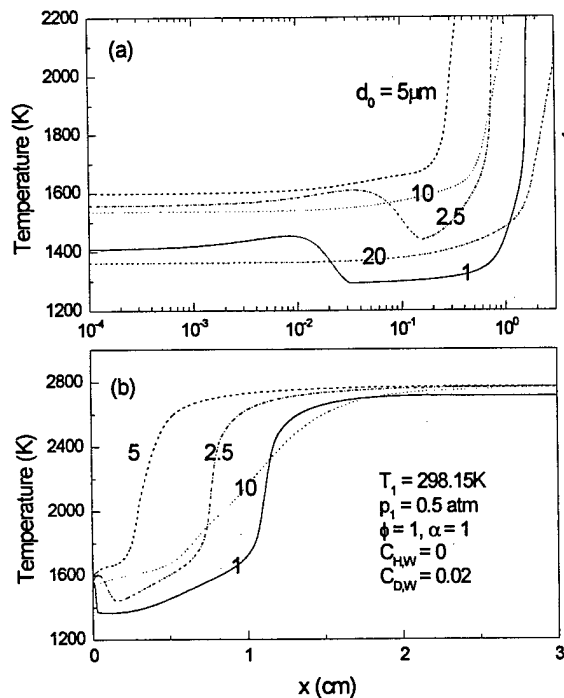


Fig. 3.21. Steady state detonation temperature profiles of different droplet sizes for stoichiometric heptane/air spray mixture, with $\alpha=1$, initial temperature 298.15 K and initial pressure 0.5 atm, for fixed wall drag coefficient $C_{D,w}$, (a) log variation in x-axis, (b) linear variation in x-axis.

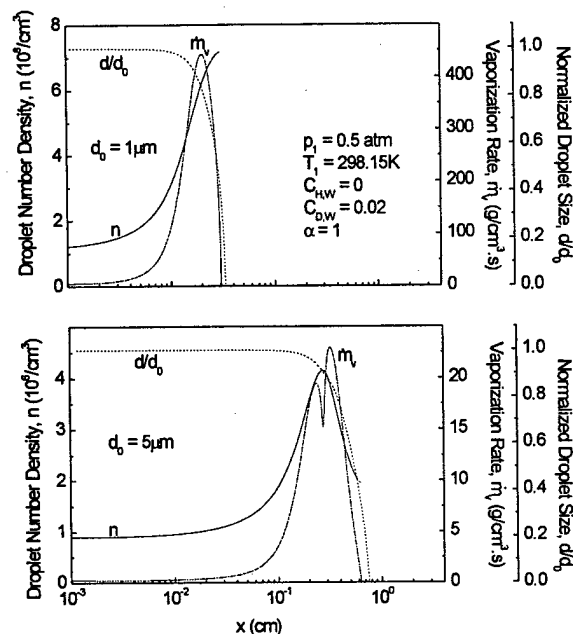


Fig. 3.22. Steady state detonation profiles of droplet number density, volumetric vaporization rate, and normalized droplet size, for stoichiometric heptane/air spray mixtures, at initial temperature 298.15 K, initial pressure 0.5 atm, droplet loading $\alpha=1$, for droplet size: (a) $d_0=1\mu\text{m}$, and (b) $d_0=10\mu\text{m}$.

increase in droplet number density, the overall liquid vaporization rate is greatly increased after this initial droplet heating stage (Fig. 3.22a), causing a substantial cooling of the gas. Consequently, chemical reaction is suppressed and this first stage ignition fails. The gas temperature then continuously decreases until the droplets are completely vaporized. The gas phase then undergoes a second ignition delay, under a lower temperature, and the ignition length is extended exponentially as a consequence. Ignition is eventually attained, as indicated by the temperature runaway.

Similar behavior is observed as the droplet size is increased to $d_0=2.5\mu\text{m}$. Since the droplets experience a smaller drag effect, they are concentrated at a later stage, leading to more fuel vaporized and reacted, and hence a larger increase in the gas temperature (Fig. 3.21a). This first stage ignition, however, still fails when cooling due to vaporization is initiated. The second induction period is nevertheless shorter because the gas starts out with a higher

temperature. The integrated external loss is then less, which results in a higher detonation velocity.

When the droplet size is increased to $d_0 = 5\mu\text{m}$ (Fig. 3.22b), the deceleration due to drag is very small and the first stage thermal runaway is already sufficiently advanced that it cannot be suppressed by the cooling due to the concentrated vaporization. The first stage ignition is therefore successful, with reduced ignition length and integrated heat loss, and consequently increased detonation velocity. It is also of interest to note that the momentary dip in the vaporization rate shown in Fig. 3.22b is due to the diminishment of its convective augmentation (the $0.276Re^{1/2} Pr^{1/3}$ term in Eq. (3.20)) as the droplets travel almost in phase with the gas. Furthermore, the eventual reduction in the droplet number density, as compared to the monotonically increasing trend for the $1\mu\text{m}$ case, is due to the increase in gas velocity with significant chemical heat release, causing the droplet to lag behind the gas and hence diluting its concentration. The increased temperature due to thermal runaway is the major reason for the second peak in the vaporization rate.

Further increasing the droplet size will increase the ignition delay again because vaporization becomes too slow such that the gas phase reaction is "choked" and limited to the rate of droplet vaporization. This then leads to a fundamental change in the detonation structure, as shown in Fig. 3.21b, which is the same plot as Fig. 3.21a except the x-variation is now linear in order to accentuate the differences in the structure for small and large droplets. It is seen that while the temperature increase is exponential-like for the small droplets, indicating Arrhenius-sensitivity of the reactions, it is more gradual and in fact is somewhat linear for the larger droplets, indicating a substantially milder sensitivity in the reaction rate. The reaction is therefore choked for these situations, being controlled by the vaporization rate. This is demonstrated in Fig. 3.23, in which development of the local droplet loading ratio is plotted. It is seen that for smaller droplets this ratio is less than unity, indicating the presence of fuel vapor which is needed to support the gas-phase (Arrhenius) reaction. However, for larger droplets, this ratio is basically unity, indicating the immediate consumption of any vapor that is released by the droplets.

Returning to Fig. 3.18, it is seen that moderately large droplets (e.g. $d_0 = 10\mu\text{m}$) can sustain higher quenching limits. The reason is that since the overall vaporization rate is now slower and hence exerts a greater influence on the rate of fuel consumption, the heat release rate

becomes less sensitive to temperature through Arrhenius kinetics. This reduced sensitivity is substantiated by the extensive range of linear-like dependence of the detonation velocity reduction on the loss strength. Of course, when the droplet is too large (e.g. $d_0 = 20\mu\text{m}$), the “induction” length becomes excessively long and quenching is facilitated due to the correspondingly significant increase in the integrated loss.

3.2.2.2. Effects of Pre-vaporization

In the study of spray combustion there is always the interest of pre-vaporizing the fuel on the belief that processes involving droplet vaporization and burning would prolong the spray combustion time. To investigate the effects of fuel pre-vaporization on detonability, Fig. 3.24 shows the detonation velocity as a function of drag coefficient for droplet sizes of 1 and 10 μm , with various levels of liquid fuel loading, α . It is seen that, for the small droplet of 1 μm , pre-vaporization increases the detonation velocity and extends the detonability limit for both adiabatic and non-adiabatic cases, although the effect is relatively small. The reason for the facilitation is the reduced need for post-shock vaporization. For larger droplets, however, this effect on the detonation velocity holds only for small drag coefficients. As the drag coefficient increases, dependence of the detonation velocity on the liquid loading varies non-monotonically.

To understand this interesting behavior, the detonation structures for three different cases are compared: no liquid loading ($\alpha = 0$), maximum liquid loading ($\alpha = 1$) with small droplet size ($d_0 = 1 \mu\text{m}$), and maximum liquid load with large droplet size ($d_0 = 10 \mu\text{m}$). Furthermore, it is important to account for the energy transferred from the gas phase to the latent heat of vaporization in the course of prevaporization. The effect can be assessed in the limits of isothermal and adiabatic freestreams. Isothermal situations are studied first, with $T_1 = 298.15 \text{ K}$. Figure 3.25 shows that for the pure gaseous case ($\alpha = 0$), the temperature immediately after the

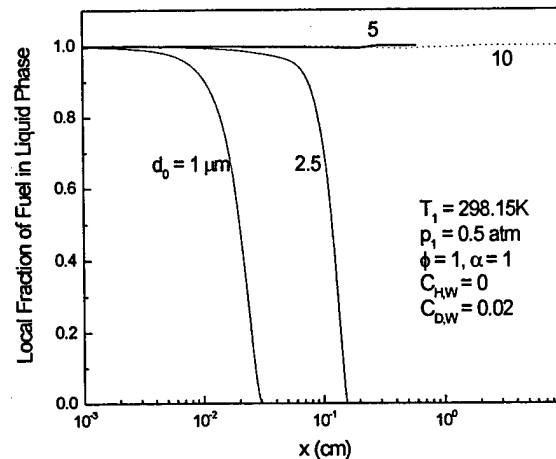


Fig. 3.23. Variation of local liquid fuel loading, defined to be the fraction of total fuel in liquid phase, with the post-shock space coordinate x , for different droplet sizes, with initial liquid fuel loading $\alpha = 1$, initial temperature 298.15 K and initial pressure 0.5 atm, $C_{H,W} = 0$, and $C_{D,W} = 0.02$.

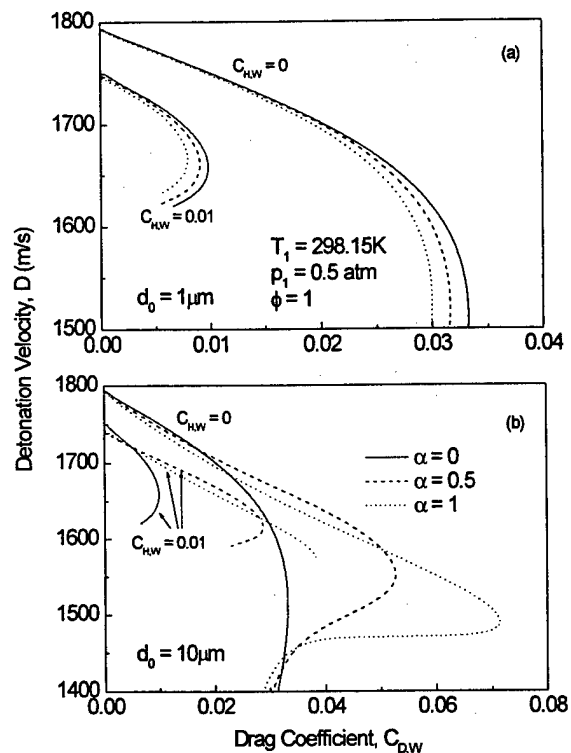


Fig. 3.24. Dependence of detonation velocity on wall drag coefficient and droplet loading α for stoichiometric heptane/air spray mixtures, at initial temperature 298.15 K, initial pressure 0.5 atm, for droplet size (a) $d_0 = 1\mu\text{m}$, and (b) $d_0 = 10\mu\text{m}$.

shock is about 100 K lower than the other two cases of maximum loading. The $1\mu\text{m}$ droplet case has a slightly longer induction length, compared to the gaseous case, due to the fast vaporization and hence failure of the first-stage ignition. However, the $10\mu\text{m}$ droplet mixture achieves runaway substantially earlier than the other two situations because it has a higher post-shock temperature, as compared to the $\alpha = 0$ case. Furthermore, it also achieves runaway in the first ignition stage, as compared to the $1\mu\text{m}$ case. While the influence of droplet size on detonability has been explained in relation to Fig. 3.18, the cause for the different post-shock temperatures for different amounts of liquid loading is not clear.

To identify the cause, Fig. 3.26 shows the normalized detonation Mach number, the heat capacity of the gas mixture before and after the shock, and the post-shock temperature and pressure as functions of the liquid loading, calculated by using Eqs.(3.34) to (3.36).

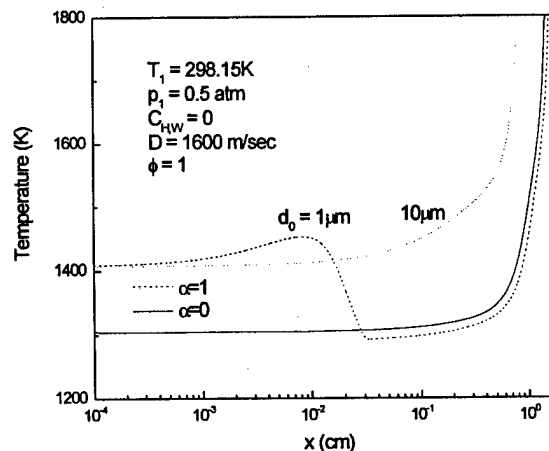


Fig. 3.25. Comparison of steady state detonation structure of stoichiometric heptane/air spray mixtures for the case in which all the fuel is initially in the gaseous phase ($\alpha = 0$) and the cases in which all the fuel is in the liquid phase ($\alpha = 1$) but with different droplet sizes ($1\mu\text{m}$ and $10\mu\text{m}$), showing that the mixture with all liquid fuel has a higher post-shock temperature than that with all fuel in gaseous phase.

Normalizations of the Mach number and the specific heats are based on the states of the pure gas. It is seen that the post-shock temperature and pressure exhibit opposite trends as the droplet loading changes, which cannot be explained based on constant- γ normal shock relations. To explain the higher p_2 with less loading, it is noted that the presence of a larger amount of vaporized fuel, which has a larger molecular weight than air, would reduce the upstream speed of sound, increase the shock Mach number, and consequently result in a greater degree of compression and hence a higher p_2 . However, while the stronger shock also tends to increase the post-shock temperature T_2 , the larger specific heat associated with the many degrees of freedom of the larger fuel molecules has a greater effect on T_2 , causing a net substantial reduction of this temperature. All of the above trends are clearly shown in Fig. 3.26.

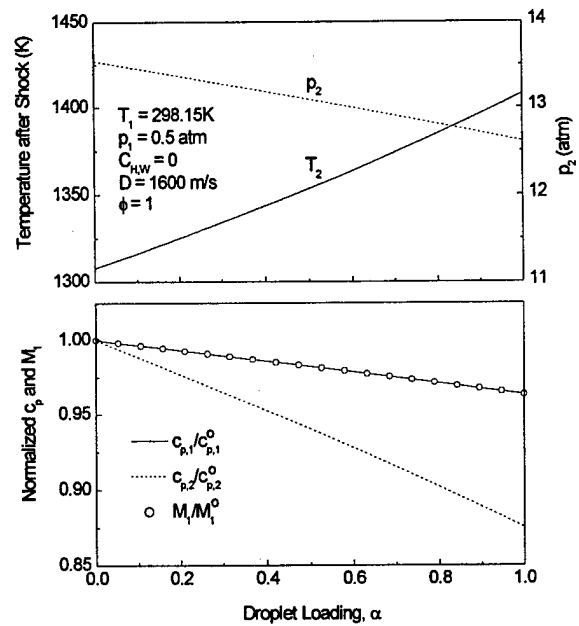


Fig. 3.26. Dependence of detonation Mach number, specific heat of gas mixture before and immediately after shock, temperature and pressure immediately after shock, on droplet loading α for fixed detonation velocity, with $T_1 = 298.1$ K and $p_1 = 0.5$ atm.

Figure 3.27 shows effects of pre-vaporizations for adiabatic upstreams, using the enthalpy of the un-vaporized case ($\alpha = 1$) as fixed values. It is seen that, for spray mixture with both small ($d_0 = 1\mu\text{m}$) and large ($d_0 = 10\mu\text{m}$) droplet sizes, propagation of the steady detonation wave through an adiabatically pre-vaporized mixture is only slightly faster than that through an isothermal one for small wall drag coefficient. However, the quenching wall coefficient for the adiabatic pre-vaporization case is only slightly smaller than that of the isothermal case for both small and large droplet sizes. The insensitivity of the detonation velocity to upstream adiabaticity versus isothermicity is due to the cancellation of two opposite effects. Specifically, by promoting isothermicity, the upstream temperature is increased. This on the one hand tends to increase the downstream temperature strictly due to shock jump considerations, while on the other hand it weakens the shock strength due to the increase in the speed of sound and hence decrease in the Mach number. The net effect is therefore small. The same consideration, though

with opposite trend, can be extended to adiabatic situations. This result therefore implies that the effects of prevaporization on the detonability discussed above hold for isothermal, adiabatic, and the intermediate situations.

3.2.3. Summary

Through the present study, the richness in phenomena offered by the various heterogeneous, droplet processes in spray detonation is appreciated. Consequently, the possible existence of optimum droplet sizes and loadings for enhanced detonation propagation and the extension of quenching limits were identified and explained. These phenomena are consequences of the strong coupling between droplet size, drag, vaporization, and loss to the wall, and as such they would not have been captured had conventional assumptions as in-phase velocities, d^2 -law vaporization, and constant specific heats been made.

The present result that there exists an optimum droplet size for detonation propagation, such that propagation may be inhibited by reducing the droplet size, is of particular interest. In this regard, it is noted that in the case of dust detonation, it was observed [59] that for a given dust loading it was more difficult to detonate a mixture with finer particle size. The reason given for this observation is similar to the present one.

It is further noted that while the study was conducted for the 1-D planar detonation in a tube which offers the crucial loss mechanism, the understanding gained herein can be readily transferred to the interpretation of the propagation and quenching of freely propagating curved detonation waves, because it has been well established that the effects of the frictional loss to the

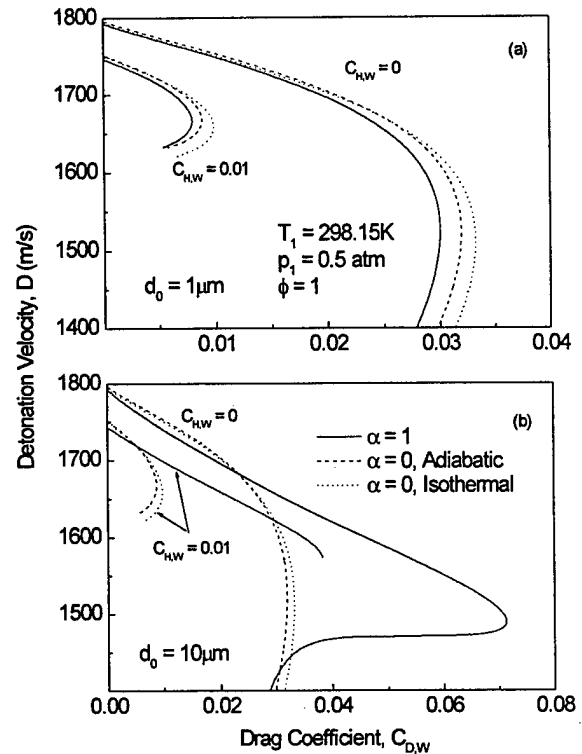


Fig. 3.27. Comparison of steady state detonation structure of stoichiometric heptane/air spray mixtures for the cases in which all the fuel is totally pre-vaporized ($\alpha = 0$) in adiabatic and isothermal environment, with the case in which all the fuel is initially in the liquid phase ($\alpha = 1$) as reference, showing that the steady state detonation velocity and the quenching limit only differ slightly between adiabatic and isothermal pre-vaporization cases.

wall are dynamically similar to that due to the curvature of the wave [46,49]. The study also showed that viable spray detonation propagation can probably only allow for droplets of the μm size range, up to say $10\ \mu\text{m}$, for the $38.1\ \text{mm}$ tube diameter used in the calculations. Recognizing that most atomization processes produce droplets whose Sauter Mean Diameter is in excess of this range, the fact that detonation is still possible is likely due to the presence of droplet shattering, upon crossing the shock, that significantly reduces the droplet size.

The identification of two modes of heat release, Arrhenius versus vaporization controlled, is particularly interesting as they depict two different detonation structures that are affected by the droplet size. Extension of the present study and understanding to other practical problems such as dust explosion of combustible materials is also warranted.

4. PENN STATE RESULTS

A focused research effort based on experiments and analysis has been carried out at Penn State to understand and develop PDE technology. The experimental work has investigated the deflagration to detonation transition (DDT) process for the relatively insensitive mixture of air/hydrocarbon fuel at both quiescent and multi-cycle conditions. In addition, the experimental research has investigated the transition of a detonation from a predetonator to a detonation tube. Both of these aspects are critical in developing a PDE engine. The concurrent modeling efforts on system performance and thermodynamic cycle analysis has yielded a practical framework for assessing the effects of all pertinent processes on engine dynamics. In this chapter, the experimental and modeling results are discussed and summarized.

4.1. Experimental Results

The experiments conducted at Penn State were focused on first, understanding the physical mechanisms of DDT and detonation transition from a predetonator tube (small diameter) to a detonator tube (large diameter) and second, exploiting this understanding to optimize both processes. For the DDT optimization experiments, both single and multi-cycle experiments were performed for various mixtures of oxygen, nitrogen and gaseous fuel (ethylene) with the goal of achieving successful detonations for the air/fuel combination. Detonation transition studies were also conducted for the same propellant mixtures, again with the goal of developing techniques for successful detonation transition based on sound physical arguments for the air/fuel combination.

4.1.1. DDT Studies

For air breathing applications, hydrocarbon-air propellant combinations are being considered, which are particularly difficult to detonate within a practical length [60]. In addition, a key barrier to the realization of an operational PDE is achieving reliable and repeatable detonations in the shortest distance possible to minimize system weight.

Researchers in the past have employed a series of repeated obstacles along the flow path to enhance flame acceleration in order to achieve self-sustained detonations [60-66]. Fundamentally, obstacle-induced turbulence increases the flame burning rate by increasing the flame surface area and the transport of local mass and energy. Moreover, turbulence scales play

a significant role in flame acceleration associated with burning rate. In the earlier stage of flame evolution upon mild ignition, large scales of turbulence are necessary to increase the surface area or flame folding, whereas excess flame stretching and rapid mixing of the burned gas may have an adverse effect on further flame evolution, which may cause the flame to completely quench. Once the flame evolves into the distributed reaction zone and thus, transforms into turbulent flame brush, finer turbulence scales are necessary to increase the flame surface area within the flame brush [61,64,65]. Therefore, optimizing the design of the obstacle configuration is necessary for reducing both deflagration-to-detonation transition (DDT) length and time in a practical PDE. Direct detonation initiation in flight vehicles would require an impractical amount of energy [67], therefore, minimizing DDT length is a fundamental goal in PDE development.

The final flame velocity generated by the turbulent flame acceleration process relies on various parameters, including the sensitivity of the mixture composition, the dimensions of the detonation tube and the size, shape and distribution of the obstacles [60,61,64,68]. Essentially, the flame acceleration process by either obstacle-induced flow or naturally occurring flow instabilities eventually leads to the DDT process throughout the shock-induced combustion ignition region by the positive feedback coupling mechanism between the shock and the flame. The DDT process is often followed by the formation of explosion centers from pockets of reactants which create small blast waves and the process is continuously amplified through multi-shock interactions with the flame [69-71]. Experiments and computational investigations of the DDT process demonstrate that the explosion could occur between the leading shock and the flame shock, at the flame front, at the shock front, or at the contact discontinuity formed by the coalescence of shock waves that proceed the flame [69,70]. Finally, with the DDT process, a strong detonation wave is formed due to coupling between the amplified blast waves and the reaction zone.

During the turbulent flame acceleration before transition to detonation, shock waves also form in the flow which further increases the burning rate such that the energy released by chemical reactions generates weak compression waves that propagate into the reactants ahead of the flame and form the initial shock wave ahead of the reaction zone. As the flame accelerates, the product temperature increases, which results in an increase in the sonic velocity and consequently allows the acoustic waves to merge into a shock wave ahead of the flame.

When the shock wave gains sufficient energy to initiate chemical reactions, shock-induced combustion occurs as the flame moves downstream. The close coupling of the energy release and the shock wave strengthens the feedback system between them, further increasing the shock wave strength and the reaction rate, resulting in the formation of a strong self-sustained detonation wave [69,71]. Combustion rate enhancement depends on the amplitude of the shock wave and the chemical reactivity of the unburned mixture.

Although research has been performed in the past to understand DDT phenomena including the use of obstacles to accelerate transition, direct observation of such phenomena has seldom been attempted. Previous research was performed using long tubes and mixtures of easily detonable fuels such as hydrogen or acetylene with pure oxygen, which cannot be used in a practical air-breathing PDE system [60,62,63]. The difficulty in sustaining a detonation depends on several parameters including tube geometry, choice of fuel and oxidizer, equivalence ratio, presence and concentration of inert gases, spark energy, initial chamber pressure and temperature, and obstacle configuration. Therefore, optimizing the system is necessary to produce the desirable detonation by considering these parameters for the practical PDE.

The objective of this phase of the study was to investigate design strategies that minimize the distance required to achieve DDT in mixtures of hydrocarbon fuel and air. An in-house developed obstacle geometry was utilized for the experiments. The obstacle size, distance between obstacles and the length of the obstacle configuration were optimized to obtain a minimum DDT length for hydrocarbon-air combustion. In-situ Schlieren, Planar Laser-Induced Fluorescence (PLIF) from hydroxyl radicals (OH), and flame emission imaging diagnostics were employed to visualize the shock wave, reaction zone and heat release, respectively. Shock and flame speeds were measured using an array of high-frequency pressure transducers and photodiodes mounted on the tube. Results are presented for both single-shot detonations in quiescent mixtures as well as multi-cycle detonations. The initial single-shot detonations involving quiescent mixtures were conducted as a basis for comparison with results from multi-cycle operation.

4.1.1.1. Experimental Setup

The DDT experiments were carried out in a 1.65 m long square tube with a 44 x 44 mm cross-section as shown in Fig. 4.1a. The cross-sectional dimensions were chosen to

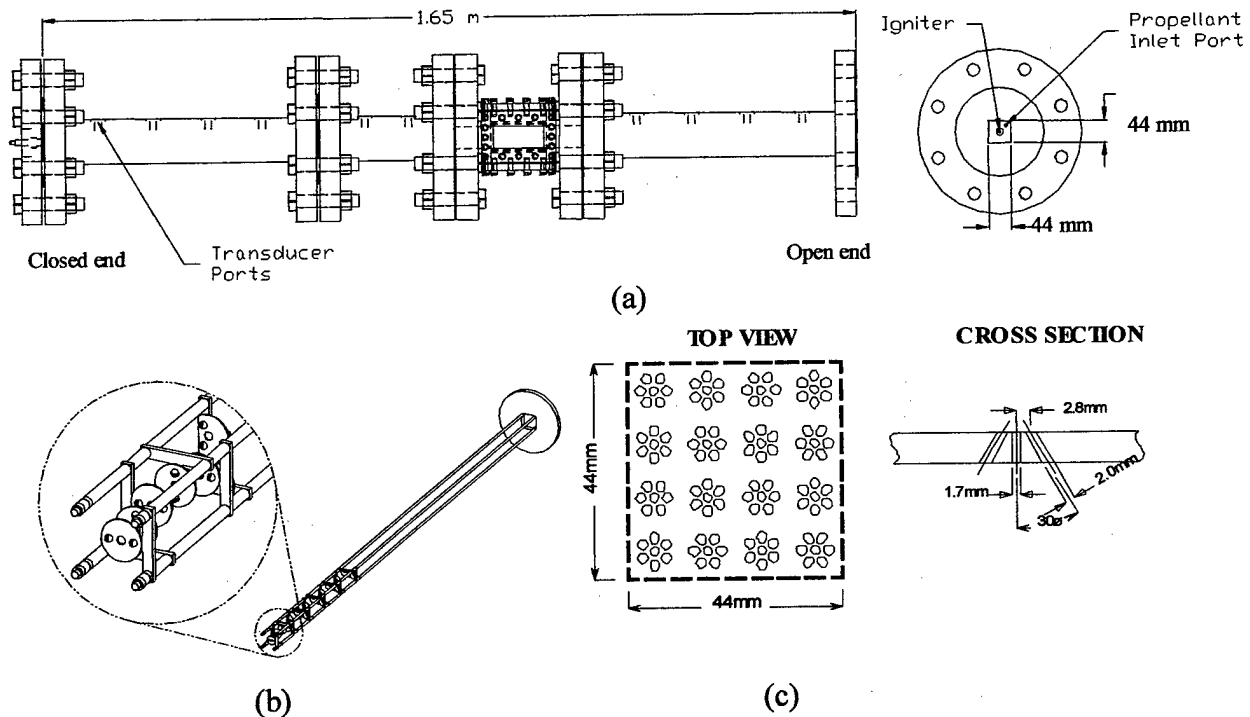


Fig. 4.1. (a) Optically accessible square detonation tube, (b) obstacle configuration and (c) propellant injector design. The sizes of the fuel and oxidizer holes are 1.7 mm and 2.0 mm,

accommodate detonations of most hydrocarbon-air mixtures [72]. The detonation tube incorporated four interchangeable sections including an optically-accessible section (window access on four sides). The obstacle used in this study consisted of flat plates mounted in a helical pattern as shown in Fig. 4.1b, similar in concept to a Shchelkin spiral [60]. Obstacles were mounted on four rods positioned inside the tube using T-shaped supports. The obstacle configuration was structurally robust to withstand detonation impulses, designed for ease in reconfiguration to facilitate rapid design optimization, and accessible to optical diagnostics.

Ethylene (C_2H_4) was selected as the fuel, due to its well-documented detonation properties with air [73] and because it is a common decomposition component of heavy hydrocarbon species typical of liquid fuels. For the baseline single-shot detonation experiments, ethylene and air propellants at an equivalence ratio of 1.2 were used since it is relatively easy to achieve detonation combustion due to the propellant combination's minimal cell size. Before filling the detonation tube, the open tube end was sealed with a 2 μ m thick Mylar film and the tube was evacuated to 3.1 Torr. The tube was then filled with the premixed fuel-air mixture to room temperature and atmospheric pressure conditions. The quiescent mixture was

ignited at the closed end of the tube with a ~25 J spark. Upon reaching the tube exit, the wave broke through the Mylar film.

During multi-cycle experiments, the propellants were injected into the detonation tube using the impinging jet injector shown in Fig. 4.1c. This injector design concept is based on conventional rocket injector designs for achieving rapid mixing. The injector has 16 impinging jet elements. Each element has a central fuel hole (1.7 mm) and six angled (30 degrees) oxidizer holes (2.0 mm). Impingement of the oxidizer jet on the central fuel jet ensures that a well-mixed flowfield is achieved in a short distance from the injector face. A spark plug was mounted transverse to the axis of the tube, 22 mm from the injector face. The injector assembly adds 60 mm to the length of the detonation tube. This injector assembly was not installed on the detonation tube for the single-shot experiments. The propellant flows in multi-cycle operation were controlled by fast response solenoid valves, with opening and closing times of ~3 ms, which were calibrated as metering orifices. Several detonations (typically ~20) of ethylene and air with equivalence ratio of 1.2 at 10 Hz were generated for the multi-cycle experiments. For a cycle, ethylene (4.4 g/s) and air (53.3 g/s) were delivered in 70 ms through the injector. The propellant valves were then closed and the mixture was ignited with a ~25 J spark. The mixture would then detonate and the tube was allowed to aspirate back to atmospheric pressure. A small amount of buffer air (5-10 ms) injected before the propellant charge for a cycle was found to dramatically improve detonation uniformity and repeatability.

OH-PLIF and Schlieren images were acquired simultaneously using the experimental apparatus shown in Fig. 4.2. The frequency-doubled laser beam from a Nd:YAG laser at 532 nm with nominal power of 230 mJ/pulse was split into two beam propagation paths using a dichroic mirror in order to provide the light source for the Schlieren system and the UV excitation beam for OH-PLIF simultaneously.

The first beam was used to pump a dye laser and the dye laser output was frequency-doubled using a wave extender to obtain the 283.01 nm (vacuum) UV beam with pulse energies of approximately 6.5 mJ for excitation of the OH $Q_1(6)$ transition. The laser sheet for the PLIF measurements was formed with a combination of a cylindrical and a spherical lens and directed into the optically-accessible section from the top. The 0.4 mm thickness sheet was positioned along the tube centerline. Window access provided a field of view of 100 mm × 45 mm. UG11 and WG 305 Schott glass filters were placed in front of an f/4.5, 105 mm UV lens

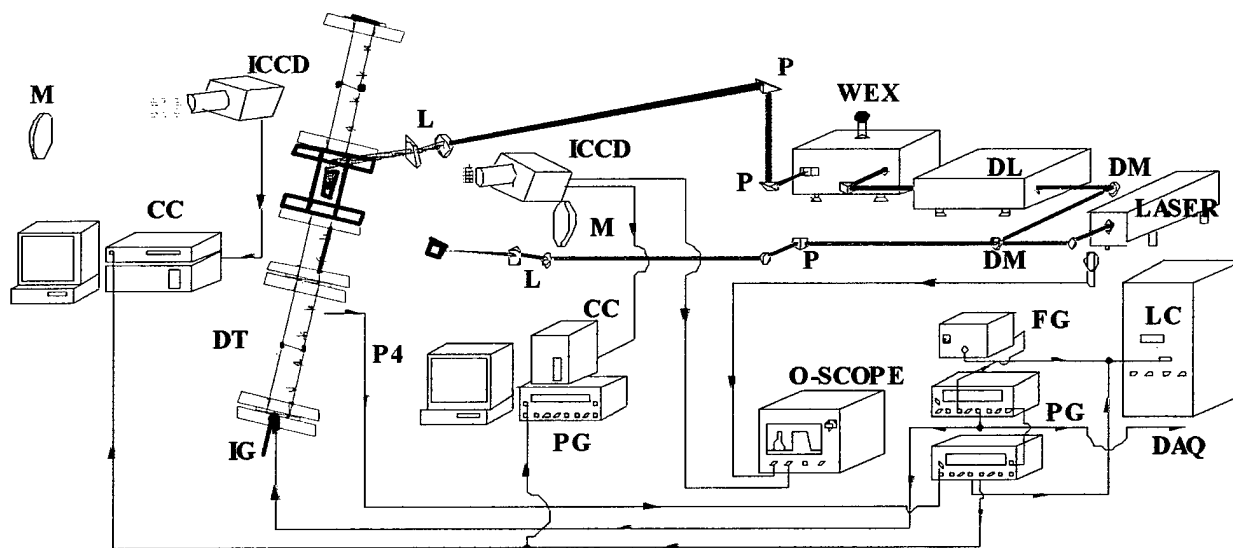


Fig. 4.2. The optical setup of the laser spark Schlieren and OH-PLIF imaging system. CC: camera controller, DAQ: data acquisition, DL: dye laser, DT: detonation tube, FG: function generator, ICCD: intensified CCD, IG: igniter, L: lens, controller, LC: laser controller, M: mirror, P: prism, PG: pulse generator and WEX: wave extender.

mounted on an intensified CCD camera. A 100 ns camera intensifier gatewidth was used to minimize interference from flame emission. When imaging the detonation region, one more UG11 glass filter was added in front of the camera to prevent saturation of the ICCD camera.

The Schlieren system was set up in a standard Z-arrangement. The second 532 nm beam was focused on an aluminum plate, and the resulting spark of incoherent light was used as a point light source. This light was collimated by a 1 m focal length, 146 mm diameter concave mirror and sent through the test section. The collimated light was collected by an identical mirror on the opposite side of the test section and then refocused through neutral density filters and a blue filter to reduce combustion light onto a razor blade. The razor edge was vertically oriented to observe the density gradients of the medium along the tube axis. The density gradients were imaged through a $f/4.5$, 60 mm lens onto a second intensified camera with a 200 ns gatewidth.

The experiments were run remotely using an electronic pulse generator that triggered the igniter, data acquisition system and the propellant valves during multi-cycle operation. A high-frequency pressure transducer mounted on the detonation tube was used to trigger the laser and both intensified CCD cameras to capture the combustion event at the proper location in the tube.

In order to monitor the combustion wave's pressure rise and flame emission, transducers were mounted along the tube, as shown in Fig. 4.1a. High-frequency pressure transducers were used to measure the compression wave arrival time, and fast response photodiodes were used to measure the time of arrival of the flame emission. The signals were sampled at 5 MHz using a data acquisition system interfaced to a computer. The arrival times and transducer positions were used to calculate flame and compression wave velocities.

4.1.1.2. Single-Shot Results

Velocity Measurements

A series of systematic experiments were performed to investigate the effect of various obstacle configuration parameters on the process of transition from weak deflagration to fully developed detonation. This series of experiments were all performed with single-shot detonations of ethylene/air at an equivalence ratio of 1.2 at atmospheric pressure and room temperature conditions. For reference, the C-J detonation velocity for these experimental conditions was calculated to be 1850 m/s using the chemical equilibrium code [74]. The C-J deflagration velocity, the so called "choking regime", which refers to the wave propagating at the speed of sound of the combustion products, is roughly half the C-J detonation velocity [75,76], and for the current conditions would be about 925 m/s. The obstacle configuration parameters that were examined included the obstacle size, spacing (pitch), and the obstacle configuration length. The obstacle pitch is defined as four times the spacing between adjacent obstacles. Numerous configurations were tested, but only eight of the most representative cases will be discussed here in conjunction with detonation characteristics related to flame acceleration. The eight configurations under consideration are summarized in Fig. 4.3. The fraction of the tube blocked by an obstacle is called the blockage ratio (BR) and is defined as the ratio of the projected area of the obstacle to the cross-sectional area of the detonation tube. Blockage ratios of 0.55, 0.41 and 0.28 were studied.

The average velocity between a pair of transducers was calculated from the ratio of the distance between the transducers to the difference of the wave arrival times at each location. The average velocities for different obstacle configurations as a function of axial location are plotted in Fig. 4.4, which shows the influence of obstacle configuration parameters on flame

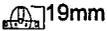
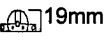
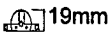
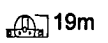
		Obstacle Size and Scale	
Obstacle	Pitch	0.5 m	
		1 m	
C1	47mm		
C2	94mm		
C3	94mm		
C4	94mm		
C5	94mm		
C6	94mm		
C7	94mm		
C8	94mm		
BLOCKAGE RATIO			
			0.55
			0.41
			0.28

Fig. 4.3. The obstacle configurations for DDT experiments.

acceleration. Only a series of weak pressure waves are observed at the head of the tube which have no clear wave arrival time, so the first two pressure transducers were not used in velocity calculations.

The results shown in Fig. 4.4 indicate that successful transition to detonation within the tube depends on the obstacle configuration parameters, an observation also noted in Refs. 60 and 61. Three different general velocity profiles can be classified from the results in Fig. 4.4: (1) failure to reach detonation velocity (configurations C1,C2,C7) in which only a strong deflagration velocity is achieved, (2) reaching C-J detonation velocity at the tube exit with some extended periods of propagation at the C-J deflagration velocity (C3,C4), and (3) achieving C-J detonation velocity at some point before the tube exit with continuous acceleration through the C-J deflagration velocity (C5,C6,C8).

The effect of the obstacle pitch on flame acceleration is demonstrated for configurations C1 and C2 where the pitch has been doubled. The velocity profiles show similar trends in the initial stages for configurations C1 and C2, but the maximum velocity is considerably greater for configuration C2. The initial acceleration in the burning rate is primarily due to the large-scale

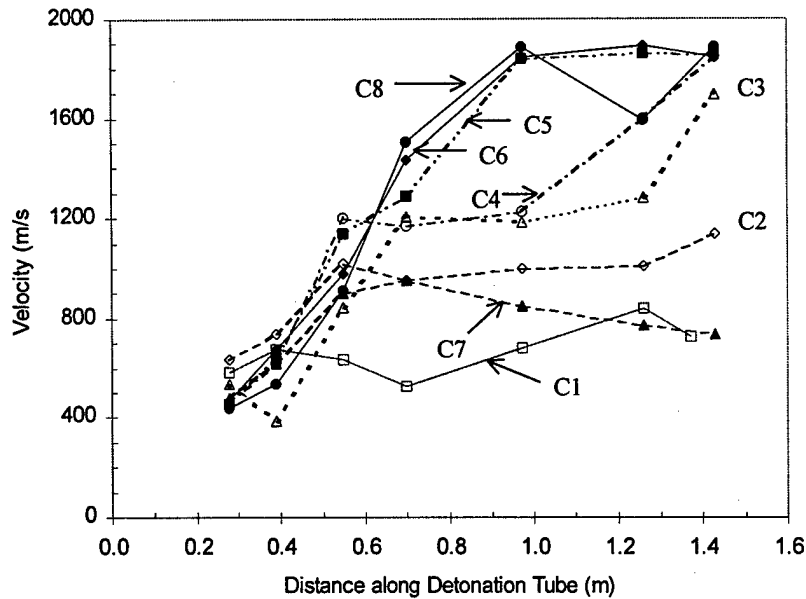


Fig. 4.4. Compression wave average velocities corresponding to obstacle configurations from Fig. 4.3.

turbulence that the obstacles impart to the flow, and initially the combustion accelerates steadily as the flame moves downstream. Further downstream, the small-scale turbulence in the shear layer and the trapped pockets of combustion become the dominant factors that further increase the burning rate [64-66]. The trapped pockets of combustion occur due to the breakdown of the large-scale turbulence of the mean flow, leaving pockets of unburned mixture in the wake of the obstacles [66]. However, when the obstacle pitch becomes too small, the momentum loss of driving the flow through the obstacles exceeds the benefits in flame acceleration. In both configurations C1 and C2, the obstacle configuration length is long enough for the flame velocities to reach nearly steady values as a balance is reached between the accelerating influence of the obstacle-induced turbulence and the flow momentum lost due to interaction with the obstacles.

The overall effect of blockage ratio on the velocity profile is observed by comparing configurations C2 and C3 where the pitch and length of the obstacle configuration are held constant, but blockage ratio is changed. The amount of flame acceleration produced depends highly on both the large and small-scale turbulence generated by the obstacles. The blockage ratio also has a strong impact on the amount of flow momentum lost as the flow passes over the obstacle configuration. Both obstacle configurations C2 and C3 have similar velocity traces in the initial regions, but C3, the obstacle with a smaller blockage ratio, achieves a considerably

higher velocity within the confines of the obstacle configuration, due to the lower momentum losses. Previous studies indicate that as the blockage ratio increases to a critical value, ranging from roughly 0.3 to 0.6, the flame velocity is able to increase further due to greater flame stretching, but beyond the critical value the flame velocity is dramatically reduced [61,65,66]. Although the C-J detonation velocity is achieved at the tube exit in configuration C3, the wave takes longer to develop and reach the C-J deflagration velocity as compared with configuration C4. This is due to the presence of larger obstacles ($BR = 0.41$) at the beginning of the tube, which are more effective at producing large-scale turbulence in the initial region where the propellant flow velocities are low.

The wave velocity is observed to roughly asymptote to the C-J deflagration velocity within the obstacle configuration, in obstacle configurations C3 and C4, where the obstacle configuration length is longer than necessary. The duration of propagation at the C-J deflagration velocity can be reduced by roughly half that observed for configuration C3 by shortening the length of the obstacle configuration. When the obstacle configuration length is shortened to terminate as soon as the C-J deflagration velocity is attained, the time spent at C-J deflagration velocity is dramatically reduced as demonstrated in configuration C5. Reaching the C-J deflagration velocity within the obstacle configuration appears to be a necessary condition for transition to detonation to occur after the wave leaves the obstacle configuration as suggested by Ciccarelli and Boccio [76]. After the flame achieves the C-J deflagration velocity and leaves the obstacle configuration, it continuously accelerates until it achieves the C-J detonation velocity, due to the coupling mechanism between the reaction zone and the leading normal shock [75,77]. If the obstacle configuration is terminated prematurely, as in configuration C7, the wave does not achieve the C-J deflagration velocity before leaving the obstacle configuration, and consequently it fails to transition to detonation. Structural supports were added to the obstacle configuration at the 1.2 m location to keep the obstacle rods flush to the tube walls and out of the window viewing area. This structural support is responsible for the detonation decelerating at approximately 1.3 m from the closed end, as seen in the C8 trace. The detonation then reaccelerates downstream due to reinitiating mechanisms [76]. Configuration C8 allowed the wave to attain C-J detonation velocity in the shortest distance, and it was used in subsequent imaging studies.

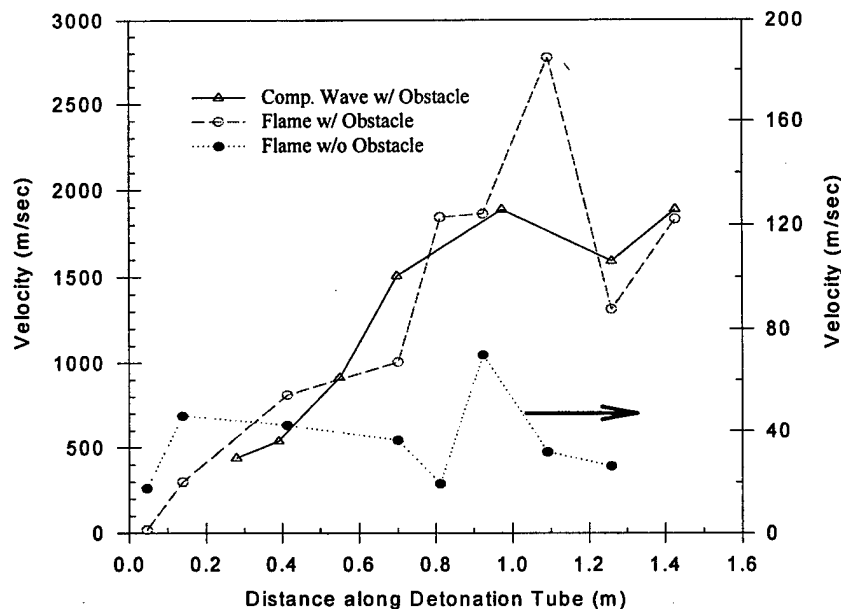


Fig. 4.5. The flame and compression wave speeds with obstacle and the flame speed without obstacle.

The flame and compression wave speeds for obstacle configuration C8 are shown in Fig. 4.5 as a function of the distance along the tube (x). Several interesting observations regarding the velocity profiles can be made. In the early stage of deflagration ($x < 0.2$ m), the compression waves travel at the local acoustic speed (~ 300 m/s) and move away from the low velocity deflagration. Before reaching the C-J deflagration velocity (~ 1000 m/s), the conglomeration of compression waves in front of the reaction zone begin to coalesce into a normal shock. As the waves propagate down the tube, they raise the temperature and pressure of the reactants based on simple shock relationship ($0.2 \text{ m} < x < 0.5 \text{ m}$). This increase in temperature and pressure, along with obstacle-induced flame stretching, allows the flame to accelerate to a slightly higher velocity than the compression waves and decreases the separation between the two. As the flame continues downstream ($0.5 \text{ m} < x < 1 \text{ m}$), the close proximity of the reaction zone and compression wave enables coherent energy release to further strengthen the leading shock wave. This coherent energy release also allows the blast waves from the localized explosions that occur in the flow behind the shock to be amplified and drive the shock wave to the point where autoignition occurs behind the wave [77]. Autoignition initiates a reaction zone close behind the shock wave ($1 \text{ m} < x < 1.2 \text{ m}$) which makes the reaction zone velocity appear to greatly exceed the C-J detonation velocity as seen in Fig. 4.5, which is similar to observations in the hydrogen-air mixture detonation study by Ciccarelli and Boccio [76].

After autoignition occurs, the flame and shock propagate at the same velocity and remain closely coupled ($x > 1.2$ m).

A flame velocity profile for a deflagration with no obstacle configuration in the tube is plotted along the right hand axis in Fig. 4.5 to demonstrate the dramatic effect of the obstacle configuration on the flow. Without an obstacle configuration, the deflagration is too weak to produce a meaningful compression wave. As expected, the flame velocity is one to two orders-of-magnitude lower than that of a combustion wave with the obstacle in the tube. Again, it is emphasized that the obstacle configuration dramatically impacts the combustion characteristics of the DDT process.

Flame Acceleration Without Obstacle Configuration

Visualization of deflagrations propagating in the tube without the obstacle configuration were acquired to compare with the images presented in the following sections and improve understanding of the role of the obstacle in flame acceleration and transition to detonation. Schlieren and OH-PLIF images of the deflagration without an obstacle configuration are shown in Figs. 4.6 and 4.7 for two axial locations. The times shown in these figures are from the time

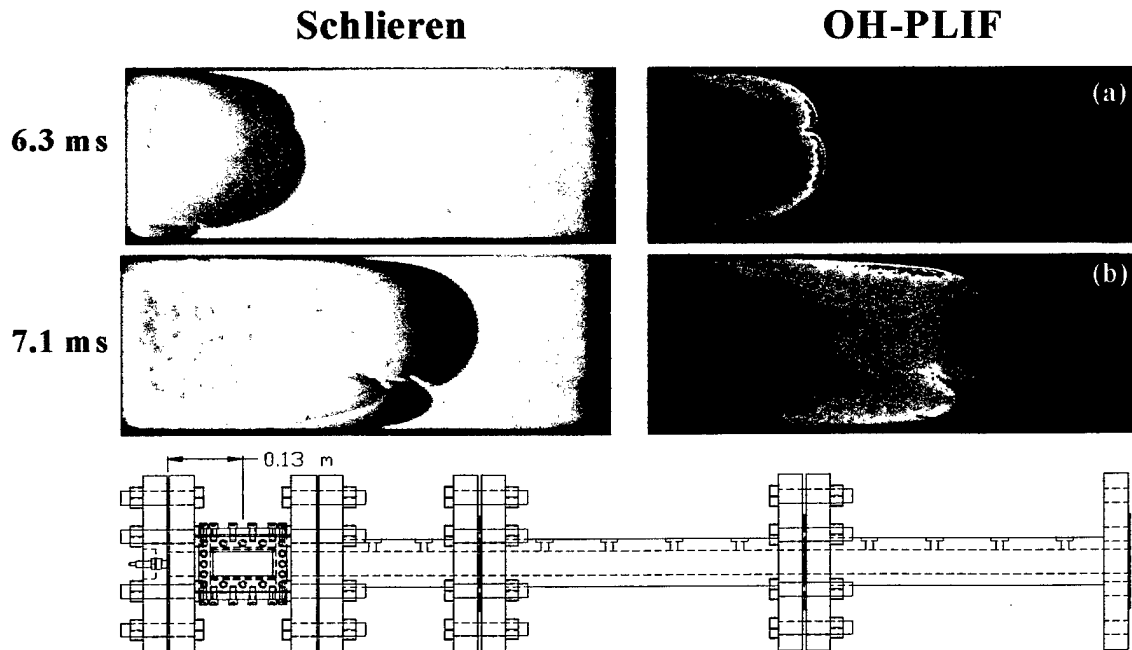


Fig. 4.6. Images of flame acceleration without obstacle, 0.13 m from closed end - Light and dark shading indicate high and low signal intensity, respectively. Flow is from left to right.

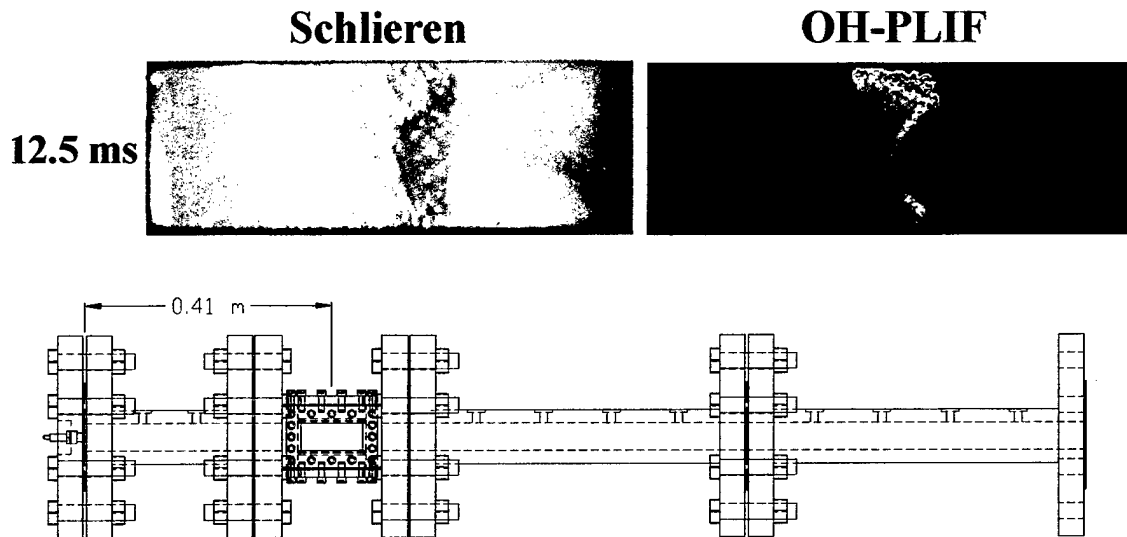


Fig. 4.7. Images of flame acceleration without obstacle, 0.41 m from closed end - Light and dark shading indicate high and low signal intensity, respectively. Flow is from left to right.

of ignition. All of the features that are present in the Schlieren images are due to combustion phenomena where the flame speeds in these images are ~ 40 m/s.

Images taken with the window section centered 0.12 m from the closed end are shown in Fig. 4.6. The two image pairs were taken 0.8 ms apart, and illustrate the flame beginning to transition from laminar to turbulent behavior. The increase in volume of the hot combustion products drives the reactants ahead of the flame front at a low initial velocity on the order of the flame speed, allowing the nearly laminar flame structure observed here. The combustion is localized to a thin sheet that slowly propagates down the tube. Local flame front speeds estimated from OH images are approximately 42 m/s and 19 m/s at the tube centerline and near the wall, respectively. A few large-scale folds in the flame front can be observed in both image pairs, but they are especially obvious in the Schlieren (b) image. These wrinkles arise from shear produced between the reactant flow and the wall of the tube. The flame wrinkling tends to weaken the local reaction rate [78], but the net effect is an increase in burning rate due to an overall increase in flame front area. Some enhancement in the burning rate can also be observed near the walls in OH-PLIF (a), which is likely due to the shear produced in the flow boundary layer stretching the flame surface.

The flame acceleration further downstream is shown in Fig. 4.7 for the window section centered 0.41 m from the closed end. The flame front is now fully turbulent. The small-scale

turbulence induced in the shear layer along the walls helps to intensify combustion and allow the flame to propagate more rapidly there. The indentation in the flame front at the tube centerline is likely enhanced by a Taylor interface instability [77], which is perturbed by compression waves reflecting from the tube closed end and sidewalls. The flow and consequently the flame would remain turbulent due to a continual input of energy from the shear layer near the wall.

DDT Process Analysis

A series of simultaneous Schlieren and OH-PLIF images were taken at different regions in the detonation tube for obstacle configuration C8 to closely examine the role that the obstacles play in accelerating DDT.

Initial Flame Acceleration

Simultaneous Schlieren and OH-PLIF images obtained at different times with the window section centered 0.13 m from the closed end are shown in Fig. 4.8 in which the first three obstacles have a blockage ratio of 0.41 whereas the last two obstacles have a blockage ratio of 0.28. The times associated with each image pair are based on an arbitrary zero time. Although each pair of images was taken during a separate experiment, experiments performed with identical timing demonstrated excellent repeatability. Figure 4.8 shows a rapid flame acceleration region where the measured flame velocity increased from ~15 m/s at the start of window section to nearly 300 m/s at the end of window section. This behavior is in agreement with the exponential acceleration predicted for repeated obstacles in previous theoretical work [64,77]. The velocities are low in this region, so compression waves generated by the dilating hot product gases will be acoustic waves that rapidly propagate away from the flame. All of the features that are visible in the Schlieren images are due to combustion phenomena.

In the first image pair, the combustion occurs along the large-scale vortex that is formed by the flow passing the second obstacle (Schlieren (a)), but no combustion is evident on the tube centerline after the second obstacle (OH-PLIF (a)). The leading edge of the flame front is smooth and nearly laminar (Schlieren (a)). Combustion is distributed across the tube just before the second obstacle (OH-PLIF (a)). Even after the flame has propagated further downstream (OH-PLIF (b)), there is still no significant combustion in the center of the region after the second obstacle, indicating that the flame is contained within the vortex shed by the obstacle, which

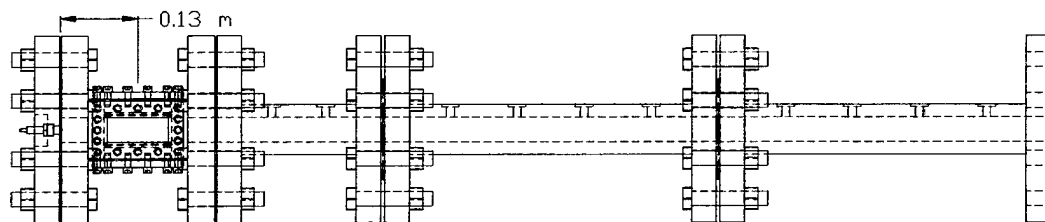
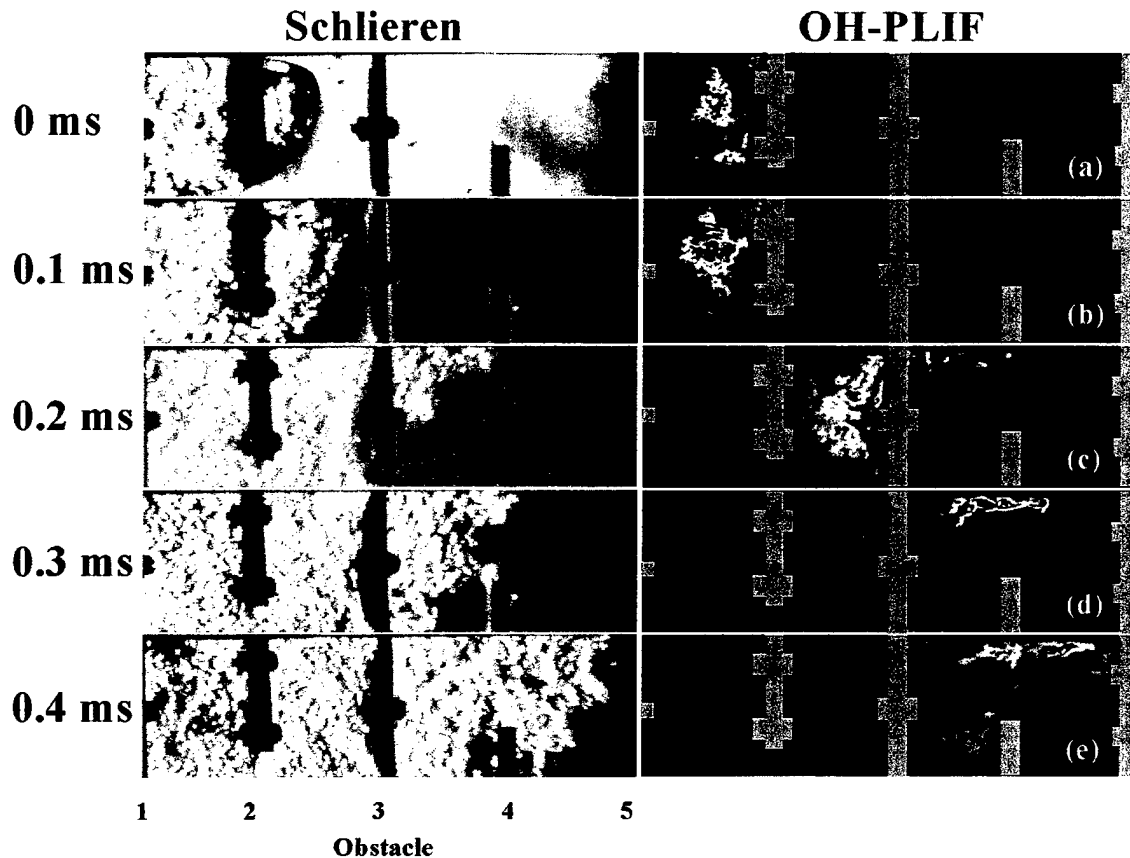


Fig. 4.8. Images in the initial flame acceleration region – Light and dark shading indicate high and low signal intensity, respectively. Flow is from left to right.

takes time to propagate to the tube centerline. This observation supports the claim of Lee and Moen [64,65] that the initial obstacle-induced flame acceleration is dominated by the large-scale vortical structures that dramatically distort the flame surface and consequently increase the burning rate.

In the third image pair, the influence of small-scale turbulence becomes more apparent. The cascading of the large-scale turbulence behind the second obstacle into smaller scales is apparent in comparing the leading edge of the flame front in Schlieren plate (a) and Schlieren plate (c). These finer scales of turbulence are important in increasing the diffusion of heat and

mass across the flame front and dramatically increase the burning rate, allowing rapid propagation of combustion across the region in front of the third obstacle (Schlieren and OH-PLIF (c)). There is also a pronounced effect of small scale turbulence in the boundary layer which allows the reaction zone to rapidly propagate along the top wall of the tube between obstacles three and four (OH-PLIF (c)).

The large scale eddies still dominate the behavior as the flame propagates around the third obstacle in Schlieren plate (d), but the turbulent wrinkling of the flame dramatically increase the rate at which the large eddy burns out and combustion sweeps across the area in front of the fourth obstacle and into the region behind the fifth obstacle (Schlieren and OH-PLIF plate (e)). There is also some confined heat release in the stagnation region in front of the fourth obstacle (OH-PLIF (e)).

The images shown in Fig. 4.8 are in excellent agreement with the conclusions of Lee and Moen [64] such that the initial acceleration of flames by repeated obstacles is dominated by large scale eddies. However, as the large-scale eddies cascade into smaller scale turbulence, the smaller scale eddies serve to increase the diffusion of heat and mass across the flame front and further increase the burning rate, by more rapidly burning out the large scale eddies.

Shock Wave Formation

The increase in volume of the combustion products produces a train of weak compression waves that propagate into the reactants ahead of the flame. As the flame accelerates, the product temperature increases and the compression waves can coalesce into a shock wave. During this process, the role of the obstacle is to continue to increase the flame surface area by generating large-scale turbulence and to provide surfaces for the compression waves to reflect from and redirect them back toward the flame front. The passage of the compression waves directly increases the temperature and pressure of the reactants, which increases the burning rate. The compression waves also tend to destabilize the interface between the cold reactants and hot products, producing a Taylor interface instability [77]. This instability provides additional deformation of the flame front, which also serves to increase the flame burning rate.

The Schlieren and OH-PLIF images obtained with the window section centered 0.41 m from the closed end are depicted in Fig. 4.9. The times associated with each image pair are based on an arbitrary zero time. Accumulations of strong compression waves are clearly

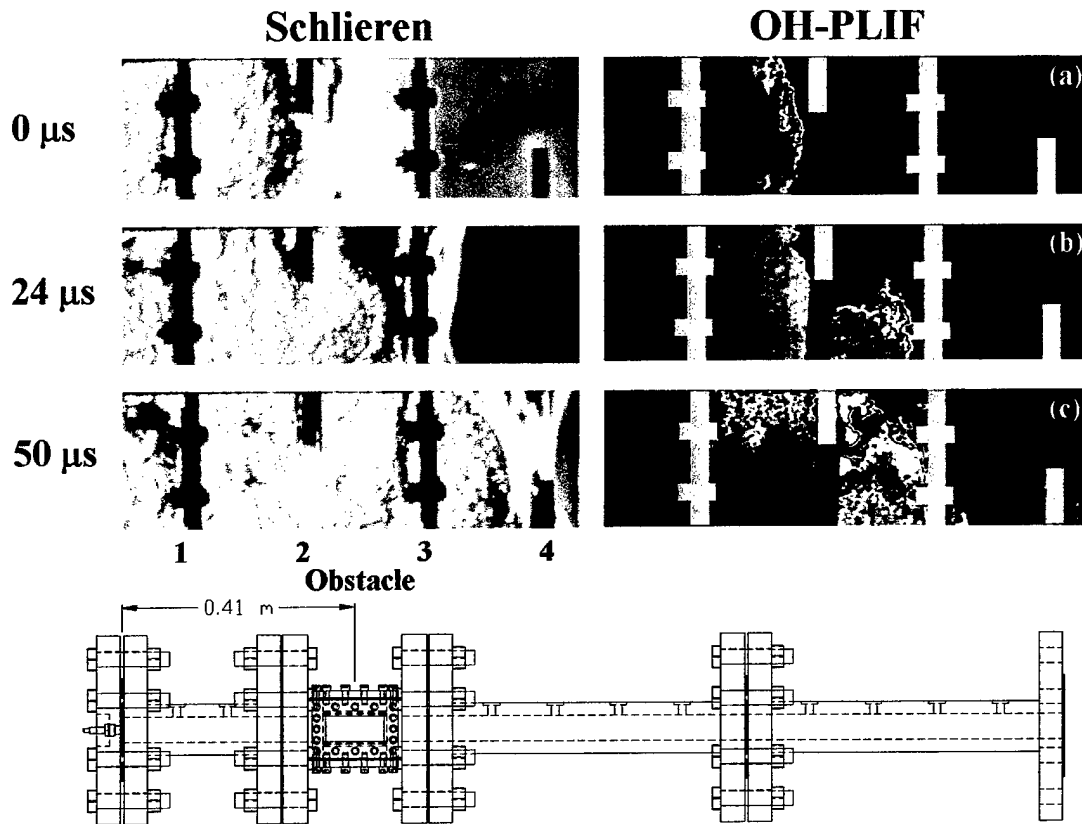


Fig. 4.9. Images in the shock wave formation region - Light and dark shading indicate high and low signal intensity, respectively. Flow is from left to right.

observed in all of these images as the farthest right flow feature in the Schlieren images. The velocity in this region increases from ~ 500 m/s to ~ 800 m/s. The heat release shown in these OH-PLIF images is intense and broadly distributed. As can be seen from the eddy developed around the second obstacle in OH-PLIF (a) and (b), the large-scale turbulence generated by the obstacles is still a predominant feature of the flow. The flow is highly turbulent at this point, and the fine scale turbulence helps to rapidly burn out the large scale eddies, as seen in OH-PLIF (c).

The obstacles also affect the coupling between the compression waves and the reaction zone. The compression waves can freely move downstream into the open region between the second and third obstacles (Schlieren (a)). In plate (b), the wave speed has been retarded near the third obstacle, which allows the combustion to approach and further strengthen the compression waves. In the region after the third obstacle, the compression waves are once again able to move away from the reaction zone. The turbulent flow around the obstacles produces a

highly three-dimensional distribution in the reaction zone and leaves some pockets of reactants, such as the wake of the second obstacle, where combustion is delayed (plate (b)). When the mixture trapped in the wake of the second obstacle starts to react, the compression waves have already propagated well downstream (plate (c)).

The approximate separation lengths between the flame front and precursor shock wave are calculated from the images. The separation length is the axial distance from the flame front to the compression wave front, which directly indicates the strength of the coupling between the two waves. Along the tube centerline, the separation length decreases from approximately 16 mm to 7 mm when the flame occurs at the middle of the image. However, the length starts to increase to approximately 26 mm again as the flame travels further downstream. Such oscillation in the wave coupling continues as the waves propagate down the tube, but continues to decrease in amplitude until the onset of detonation. It is also emphasized that the flowfield is highly three dimensional, due to the interaction of the flow with the obstacles.

Explosion Center Formation

With the window section centered 0.69 m from the igniter, the intense chemical reactions present during this stage of the DDT dramatically reduce the signal-to-noise ratio of the OH-PLIF measurements. Because of this difficulty, flame chemiluminescence (OH* emission) is responsible for much of the OH signal strength for images taken in this region.

A series of images of the flame evolution, taken with the window section centered 0.69 m from the closed end are shown in Fig. 4.10. The left edge of the field of view is 0.11 m from the end of the obstacle configuration. The compression wave speed measured in this section increases from ~1200 m/s to ~1500 m/s, higher than both the C-J deflagration velocity and the flame speed. The compression waves are closely coupled to the turbulent flame brush that follows the wave front (Schlieren and OH-PLIF (a) and (b)). There are no longer obstacles in the flow path to directly generate large scale eddies in the flow, but the reflection of compression waves from the tube walls and from the tube closed end tends to enable the same Taylor interface instability that was discussed in the previous region. This interaction between the compression waves and the interface between the product and reactant gases deforms the flame front and tends to increase the surface area.

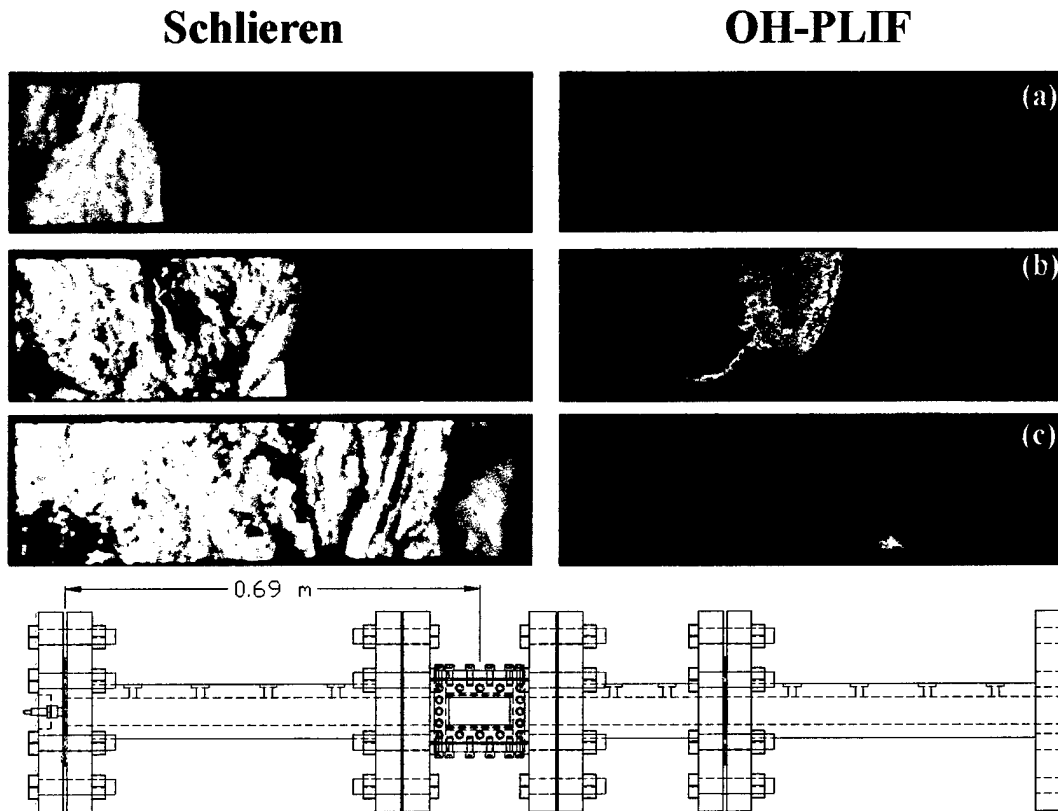


Fig. 4.10. Images in the region of explosion center formation - Light and dark shading indicate high and low signal intensity, respectively. Flow is from left to right.

The compression wave front in Schlieren (a) is highly convoluted and corrugated and some of this corrugation persists in Schlieren (b), even though the wave front has become more normal. This strong variation in compression wave structure and intensity is reflected in the distribution of heat release across the tube, which closely follows the structure of the compression wave front (OH-PLIF (a) and (b)). This correspondence in the compression wave and heat release structure is indicative of coherent energy release, which serves to amplify and strengthen the compression wave front and then further strengthens the reaction zone intensity. This energy release in phase with the pressure oscillations is essentially the Rayleigh criterion, which leads to adverse pressure oscillations in other devices, such as gas turbines [78]. This behavior is essential to transition to detonation, and is part of an acceleration mechanism proposed by Lee and Moen known as SWACER or Shock Wave Amplification through Coherent Energy Release [77]. This coupling of the heat release with the pressure fluctuations allows for their rapid amplification, which is essential for achieving transition to detonation.

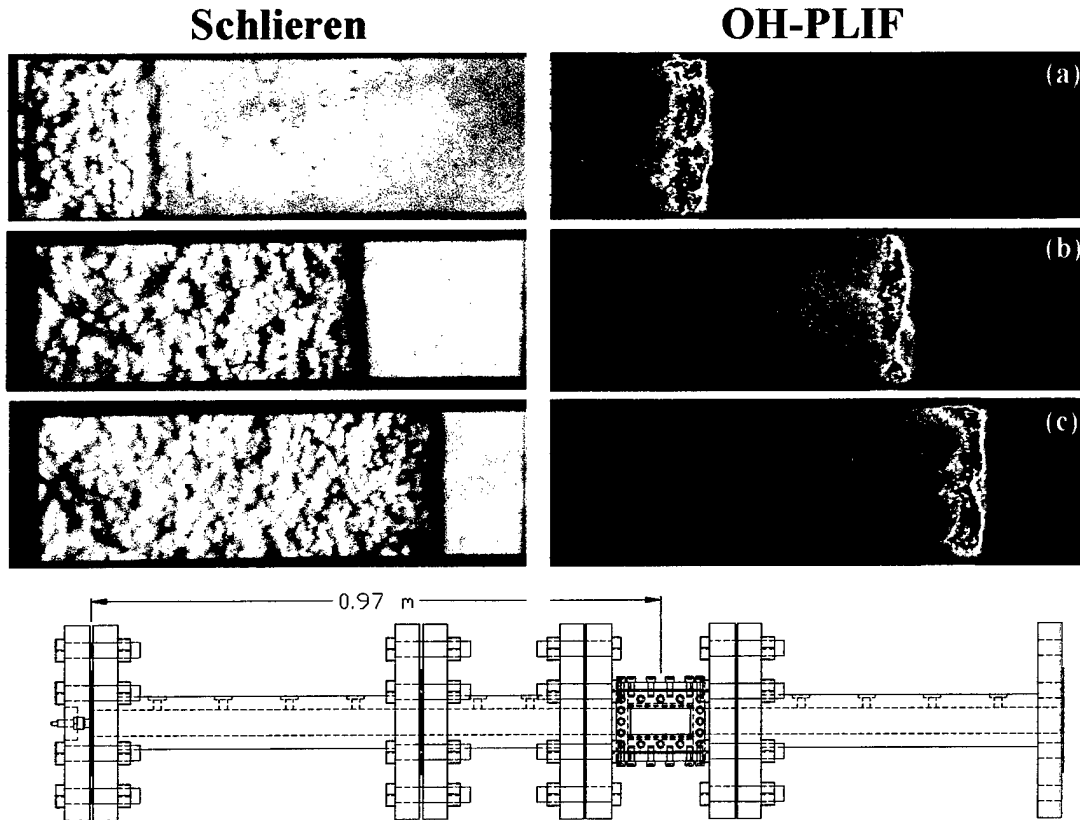


Fig. 4.11. Images of an established detonation wave - Light and dark shading indicate high and low signal intensity, respectively. Flow is from left to right.

The final process that leads to transition to detonation is the occurrence of localized explosions in trapped pockets of unburned reactants. These explosions send out blast waves, which are amplified by the aforementioned coherent energy release and serve to drive the compression wave front past the C-J detonation velocity and allow the formation of a self-sustained detonation. An intense localized explosion is seen in the flow boundary layer in plate (c) of Fig. 4.10.

Detonation Formation

A normal detonation wave established in the window section centered 0.97 m from the closed end is shown in Fig. 4.11. As in the previous sub-section, the flame chemiluminescence is very intense and is responsible for much of the OH signal in the images presented. At this point, the compression waves that were observed in the previous region have fully coalesced into a strong normal shock. The shock is strong enough to cause autoignition in the reactants and it is

closely followed by a nearly uniform and very intense reaction zone. Transverse waves can be seen on the left hand side of Schlieren (b) and (c), well behind the reaction zone. These waves play an important role in establishing the true three-dimensional structure of the detonation wave.

The maximum steady velocity achieved in deflagrations without an obstacle configuration was ~ 40 m/s, one to two orders-of-magnitude less than C-J detonation velocity. This reemphasizes the important role that the obstacle configuration plays in accelerating the DDT process. In particular, the large-scale turbulence that is produced as the propellant flow interacts with the obstacles, and the smaller turbulence that those large-scale eddies cascade into, dramatically accelerate the burning rate. This rapid increase in burning rate allows the rapid generation of compression waves, which precondition the reactants and further accelerate the combustion process. The fundamental step of the DDT process is the successful production of a shock wave strong enough to autoignite the reactants. If the burning rate rises rapidly, the compression wave energy will be more compactly distributed along the length of the tube and the coupling of reaction zone and shock wave precursor waves will be much stronger. The obstacle configuration C8 used in this study had the additional benefit of reflecting compression waves back toward the reaction front, which served to increase the reaction rate and keep the compression waves from propagating down the tube and decoupling themselves from the reaction zone.

4.1.1.3. Multi-Cycle Results

Multi-cycle results with the square detonation tube were obtained for 10 Hz operation using ethylene and air, but further increases in repetition rate were hindered by problems with filling the tube completely and igniting the rapidly moving mean flow. The C8 obstacle configuration as shown in Fig. 4.3 was used for the multi-cycle experiments. A fifty percent reduction in DDT time from 6 to 3 ms was observed when compared to the single-shot experiments, but the DDT length remained unaffected around 0.95 m.

Compression wave velocities from several detonations in one multi-cycle experiment are shown in Fig. 4.12. In addition, a velocity trace from a typical single-shot experiment using the same obstacle Fig. 4.11 shows is shown in the figure for comparison. The decrease in velocity in Fig. 4.12 at approximately 1.2 m from the injector face is due to the detonation being perturbed

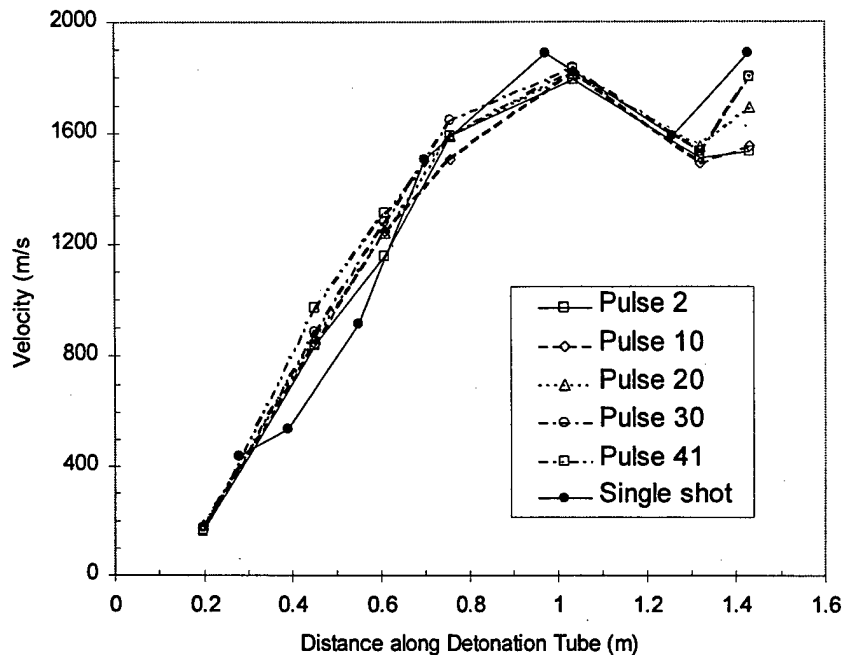


Fig. 4.12. Compression wave velocities for multi-cycle operation from the closed end.

by a structural support used to keep the obstacle rods flush to the walls in the imaging section. The multi-cycle detonations were very consistent from shot to shot, with the only observable change being at the last position, where the velocity slightly increases as the detonation tube temperature increases. The influence of dynamic injection on DDT is clearly observed in the initial portion of the tube, where the multi-cycle detonations accelerate much faster than for the corresponding quiescent single-shot case, due to the existence of mean flow velocity and turbulence at the time of ignition.

Simultaneous CH^* chemiluminescence and Schlieren images were acquired during multi-cycle operation at a rate of 5 Hz, during 10 Hz operation. Note that CH^* chemiluminescence provides the flame emission which is similar to OH^* chemiluminescence. Two pairs of typical images are shown in Fig. 4.13, taken 1.02 m from the injector face. These results are very similar to those obtained in single-shot operation at the similar location (Fig. 4.11).

4.1.2. Detonation Transition Studies

In the past decades, several studies have been devoted to determining the conditions for successful propagation of a CJ detonation wave from a small tube either to an unconfined or a confined environment. It is now commonly accepted that when the predetonator diameter is

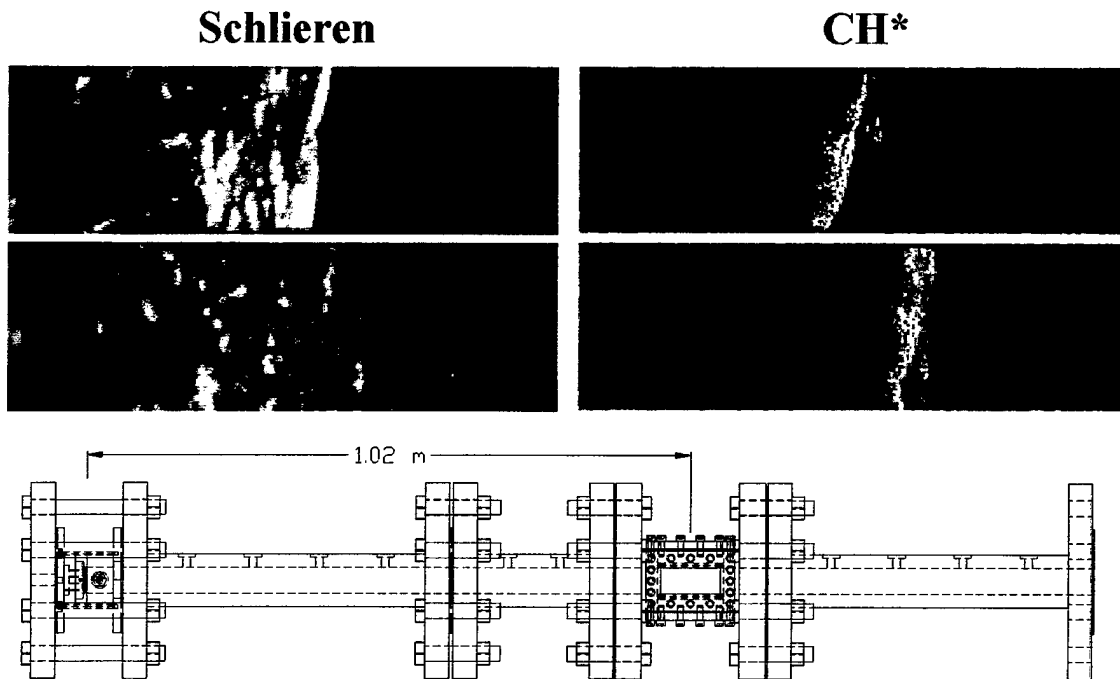


Fig. 4.13. Multi-cycle images of transition to detonation region - Light and dark shading indicate high and low signal intensity, respectively. Flow is from left to right.

large enough to accommodate 9 to 13 detonation cells, depending on the geometry and fuel/oxidizer mixture, successful transition of the detonation occurs [79-81]. This tube diameter is usually referred to as the critical diameter. Unfortunately, meeting this critical diameter requirement would require predetonator tubes for a practical PDE to be of a large diameter, which would, in turn, result in increased difficulty in initiating a detonation. Although this problem could be avoided by using more sensitive mixtures in the predetonator, such as fuel/oxygen mixtures, the added PDE engine complexity discourages pursuing such a solution.

During the same period another process that leads to the formation of a detonation has been the subject of several studies, namely the deflagration to detonation transition. The first experiments conducted by Urtiew and Oppenheim [82] on this topic demonstrated that at the time immediately preceding the onset of a detonation wave, an “explosion in the explosion” occurs, which accelerates the flame and leads to the formation of a detonation wave. This explosion (referred to here as localized explosions) can either occur between the leading shock and the flame shock, at the flame front, at the shock front, or at the contact discontinuity formed by the coalescence of shock waves that precede the flame [82,83]. No matter which phenomena cause the onset of a detonation, the detonation wave that emerges from the DDT

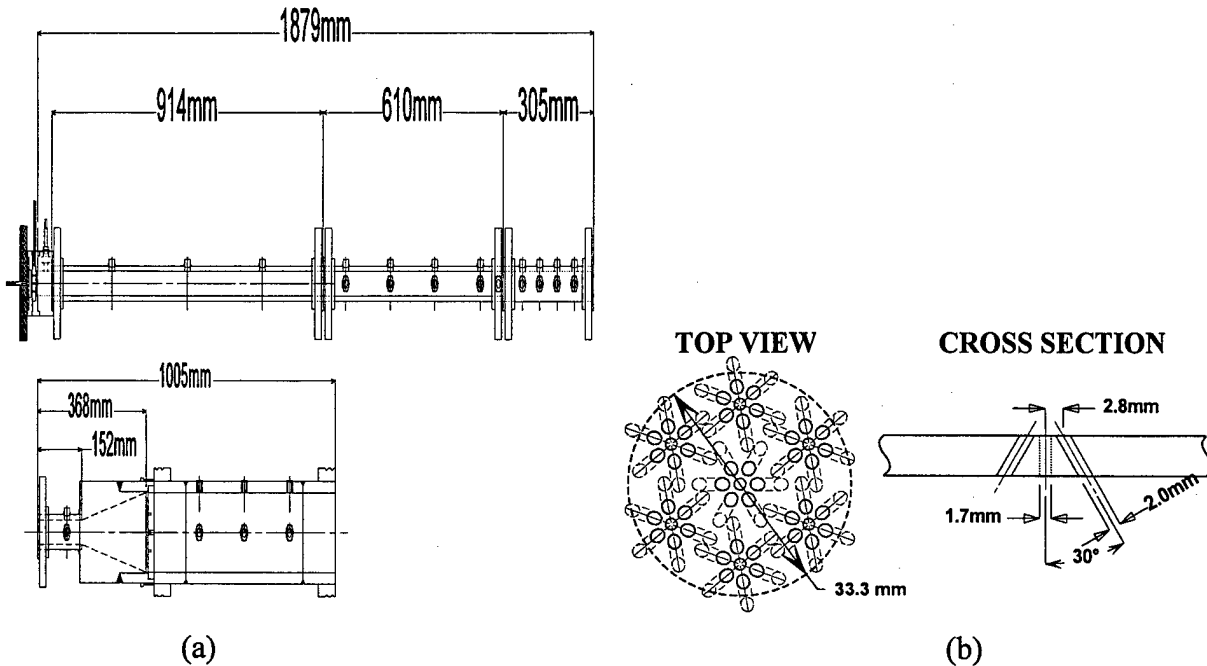


Fig. 4.14. (a) Detonator tube including predetonator, transition section and main detonator. (b) Impinging injector face. The fuel is injected along the center holes with surrounding oxidizer holes.

process presents a high degree of overdrive. Such a highly unsteady state of a detonation wave can be exploited, along with shock-focusing obstacles, to ease the transition of the detonation from the predetonator to the main tube. The same concept can be utilized in multi-cycle PDE operation. Furthermore, the volume of the predetonator can be significantly reduced by employing obstacles to enhance flame acceleration in the predetonator [72,84,85].

4.1.2.1. Experimental Setup

The detonation tube used in these studies is composed of three sections shown in Fig. 4.14a: a 33.3-mm diameter, 1.117 or 2.031-m long predetonator, a 216-mm long conical transition section with a 10-degree divergence angle, and a 105-mm diameter, 637-mm long thrust tube. The geometry and angle of divergence of the transition section were designed to minimize diffraction effects at the area change [86]. Ethylene-oxygen-nitrogen mixtures, with a fixed equivalence ratio of 1.1, are injected at the head end of the predetonator through an impinging jet injector, shown in Fig. 4.14b. In order to confirm the target equivalence ratio, fuel concentration was monitored using the 3.39 μm He-Ne laser absorption measurement.

The evolution of the detonation wave is monitored by using high-speed piezoelectric pressure transducers and photodiodes mounted along the tube at identical axial positions. Throughout the experiments, the level of nitrogen dilution, i.e. the ratio of moles of nitrogen to moles of oxygen, is varied from 0 to 3.76 by keeping constant the fuel and oxygen mass flow rates and by changing the nitrogen flow rate. In order to explore the effects of shock-focusing obstacles on the developing detonation wave in and around the transition section, shock-focusing obstacle disks of 50% and 78% BR (blockage ratio), and a 78% BR 45° obstacle cone were used in the experiments.

4.1.2.2. Results and Discussion

A summary of the experiments conducted is given in Table 4.1. Experiments where successful detonation transition was observed are marked with "S", whereas detonation failures are marked with "F". A total of 13 different configurations were investigated in the current study. These configurations can be divided into two groups. For the first group, a 1.117-m long predetonator was used, whereas for the second group the predetonator length was extended to 2.031 m. Within each group several shock-focusing obstacles placed at different locations downstream from the transition exit were used. As seen from the table, detonation transition is easily obtained for the most sensitive mixtures, i.e. mixtures characterized by a low nitrogen dilution. As nitrogen dilution is increased, the detonation wave fails to transition first for those

Table 4.1. Summary of Tested Configurations.

N ₂ /O ₂	1117 mm Predetonator Tube							2031 mm Predetonator Tube					
	78% BR Flat Disk				50% BR		No	78% BR Flat Disk			45 Deg Cone		
	Direct				With Dump		Direct	Direct	Direct			Backward	Forward
	0 cm	5 cm	10 cm	15 cm	5 cm	10 cm	5 cm		5 cm	10 cm	15 cm	0 cm	0 cm
0.00	S	S											S
0.75	S	S											S
1.50	S	S											S
2.25	S	S	S	S									S
2.40		S			F	S	S						S
2.50								F					S
2.60		S			F	S	S/F	F	S				S
2.70								S					S
2.80		S			F	F	F		S				
3.00	F	S	S/F	S/F				F	S			S/F	S
3.20		F	F	F					S			F	
3.40		F	F	F					F	S/F	F		
3.60		F	F	F					F	F	F		
3.76	F	F	F	F				F	F	F			S

S: Successful Detonation

F: Failure Detonation

Velocity are measured at the 38 cm downstream of transition exit

configurations where a shock-focusing obstacle is not used and eventually for those where shock-focusing obstacle is used as well. It is apparent that a shock-focusing obstacle enhances the chance that a detonation wave has to survive over the transition from the predetonator to the main thrust tube; however, for the 1.117-m long predetonator, none of the configurations explored here allowed a successful detonation transition with a nitrogen to oxygen dilution ratio higher than 3.0.

It is also seen from the table that, when a longer predetonator is used, the range of nitrogen dilution for which successful detonation transition occurs is extended to a nitrogen to oxygen ratio equivalent to air (3.76). In fact, as nitrogen dilution is increased, the onset of the detonation in the predetonator is moved further downstream toward the transition section. In the final stages of the DDT process localized explosion occurs and the resulting detonation wave is characterized by a high degree of overdrive. Thus, the overdriven detonation wave enters the transition section before it decays back to the CJ state. It is believed that within the transition section, further interaction of the decaying detonation with the shock-focusing obstacle generates hot spots where localized explosion occurs. Again, this phenomenon sustains the detonation and allows it to successfully transition into the thrust tube.

An example of pressure traces measured during the experiment along the tube axis is plotted in Fig. 4.15 along with the space-time diagram. Examples of the pressure and corresponding photodiode traces, at an axial location close to the transition section, are also shown in more detail in Fig. 4.15c. It can be seen from these traces that as the flame accelerates along the tube, compression waves generated by the dilation of the hot gases resulting from the combustion, coalesce in front of the flame and generate a leading shock. While the shock propagates along the tube at a constant Mach number (approximately equal to 2), the flame accelerates and tends to catch up with the leading shock. Inside the transition section, the DDT process is finalized and thus, an overdriven detonation wave and a corresponding detonation wave are generated. Subsequently, the detonation wave propagates as a CJ detonation down the main tube.

A schematic representation of the process that is believed to be occurring in the conical transition section is depicted in Fig. 4.16. The key phenomena include the propagation of overdriven detonation occurring in the end region of the predetonator which is followed by a initiation of significant energy release in the volume of gases located in the transition section.

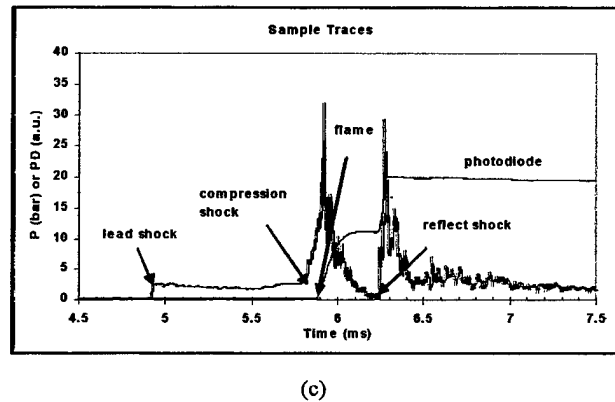
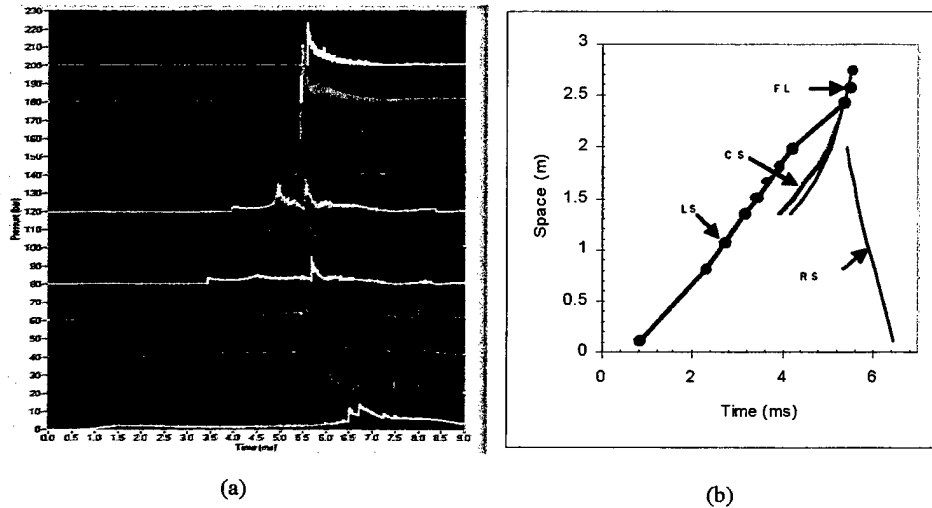


Fig. 4.15. Sample pressure traces with schematic diagram of the deflagration to detonation transition and space-time data showing the leading edge (LS), compression shock (CS), flame (FL), and reflected shock (RS).

The enhancement observed with the addition of the transition obstacles is postulated to be a result of shock focusing as compression waves are reflected from the obstacle and walls.

Unfortunately, the lack of any diagnostics within the transition section does not allow the directly identification of the process responsible for the successful detonation transition. Nevertheless, since for the current apparatus it was observed that the strength of a reflected shock off the shock-focusing cone is less than 10% of the strength of the incident shock, it can be inferred from the pressure trace recorded directly upstream from the transition section that a localized explosion has occurred in between this location and the exit of the transition section. Thus, it can be concluded that the overdriven state of the detonation is responsible for the successful transition of the detonation wave into the main thrust tube.

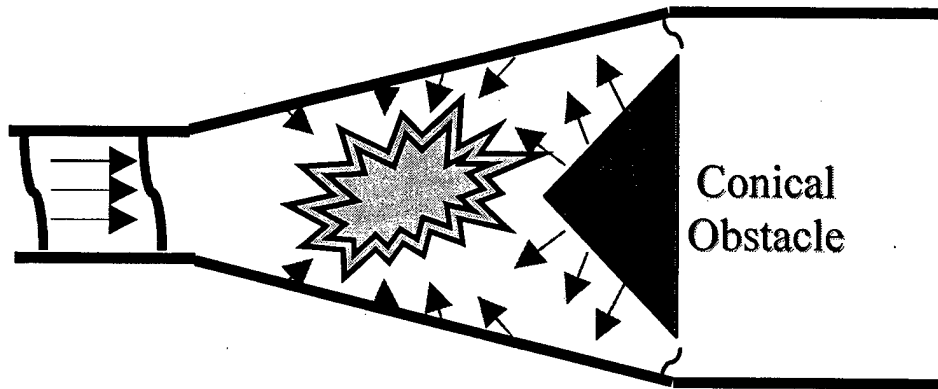


Fig. 4.16. Schematic representation of the initiation of detonation transition from the predetonator to main thrust tube.

Based on the results presented several important effects arise for further investigation. First, the present results indicate that conical obstacle is superior to the flat disk obstacles of comparable blockage ratio. The explanation presented argues that shock focusing is enhanced by the conical obstacle as compared to the flat disk obstacles. This hypothesis has yet to be proven using direct visualization of the transition section, which is planned for future investigations. If shock focusing is a key aspect of the process then specific contouring of the transition obstacles may provide a means to further optimize the obstacles in terms of enhancing the transition from the predetonator to the main thrust tube.

Second, the volume of the transition section may be of importance in terms of the energy release process that occurs. Only a few experiments have been done to date to investigate this effect and the results appear to indicate that the transition section volume does have an effect as mixtures having nitrogen to oxygen ratios close to air are used. Finally, the extension of this work to fuels other than ethylene is essential for practical PDE operation. Preliminary studies using propane have shown that similar phenomena occur in terms of the transitioning mechanism. However, as one would expect, it is more difficult to successfully initiate a detonation in the main thrust tube for propane than for ethylene, particularly as nitrogen to oxygen ratio approaches values close to that of air.

4.1.3. Summary

The DDT enhancing characteristics of helically configured flat plate obstacle were examined systematically in a series of single-shot ethylene-air experiments. The large-scale turbulence generated by the flow interaction with the obstacles was shown to dramatically

increase the flame surface area and consequently increase the burning rate. The production of fine-scale turbulence in the flow boundary layer and in the breakdown of the large-scale vortices was also observed to increase the local burning rate and dramatically accelerate the burning velocity. Obstacle blockage ratios between 0.3 and 0.6, and sufficient obstacle spacing were found to provide optimum levels of flame stretching without inducing excessive flow drag.

For all obstacle configurations, the critical step to achieving detonation in these experiments was attaining the C-J deflagration velocity within the obstacle configurations. Any length of obstacle after the compression waves reached the C-J deflagration velocity was observed to be unnecessary and delayed the onset of detonation. After attaining the C-J deflagration velocity, the flame would remain at that speed until it reached the exit of the obstacle configuration, where it would proceed to accelerate and transition to detonation. If the wave had not reached the C-J deflagration velocity before exiting the tube, the compression waves and reaction would decouple and DDT would not occur.

In the imaging study of the obstacle configuration C8, the reaction rate was also accelerated by the action of compression waves that emanated from the expanding hot product gases. The compression waves served to increase the temperature and pressure of the reactants, which directly increased the burning rate. Reflection of the compression waves back toward the flame surface also served to excite a Taylor interface instability that further stretched the flame surface and increased the burning rate. The obstacles used in these experiments enhanced this process by providing numerous surfaces to reflect the compression waves back toward the flame front. The obstacle configuration also hindered the progress of the compression waves in propagating down the tube until the burning rate was fast enough to maintain coupling between the flame front and the compression waves.

Heat release in phase with the pressure oscillations in the flow enabled disturbances to be amplified. This allowed the localized explosions that occurred in the flow to be amplified and further strengthen the leading shock wave. Once the shock wave was sufficiently strong, autoignition occurred and a closely coupled reaction zone was established behind the shock, thus forming a self-sustained detonation wave.

Multi-cycle experiments were also conducted in the square tube to examine the effect on the DDT process of the initial mean flow and turbulence resulting from dynamic injection of the propellants into the tube. Repeatable operation at 10 Hz showed a decrease in DDT time from 6

to 3 ms whereas the DDT length remained constant around 0.95 m. Multi-cycle images of the transition from a strong deflagration to a normal detonation wave were found to be very similar to the results obtained for the single-shot experiments.

A series of studies has also been completed to investigate transitioning of a detonation from a small diameter predetonator tube to a large diameter main thrust tube using obstacles placed in the transition section connecting the two tubes. These results show that transitioning can occur for a predetonator tube diameter that is less than 9 to 13 detonation cell sizes that is often the criteria observed for unconfined detonation transition. A key result of the current studies is that the conditions in the region just upstream of the transition section are critical in determining whether a successful transition is observed. In particular, achieving a CJ detonation in the predetonator does not assure that a detonation will be initiated in the main thrust tube. In fact, the critical phenomena appear to be the occurrence of localized explosions that occur just prior to establishment of a CJ detonation. It is postulated that the resulting overdriven detonation coupled with shock reflections from the transition obstacle that are focused in the volume of combustible gas in the transition section leads to a rapid energy release in a confined region and results in the initiation of the detonation in the main thrust tube.

4.2. Modeling Results

A system performance and thermodynamic cycle analysis for air-breathing pulse detonation engines (PDEs) was established in the MURI-PDE project. The work accommodates all the essential elements of an engine, including inlet, manifold/valve, injector, combustor, and nozzle, as shown schematically in Fig. 4.17. Emphasis is placed on multi-tube configurations with repetitive flow-distribution capabilities (e.g., rotary valves). The primary outcome is a general framework, in a form suitable for routine practical applications, for assessing the effects of all known processes on engine dynamics. It also helps designers and researchers to optimize the overall system performance and to identify the major technological barriers at minimal computational expense. Major variables and phenomena of consideration include fueling strategy, injection scheme, chamber conditions, and configuration geometry.

The analysis is developed using a modular approach. Each module represents a specific component of the engine, and its dynamic behavior was formulated using complete conservation equations. The governing equations and their associated boundary conditions are numerically

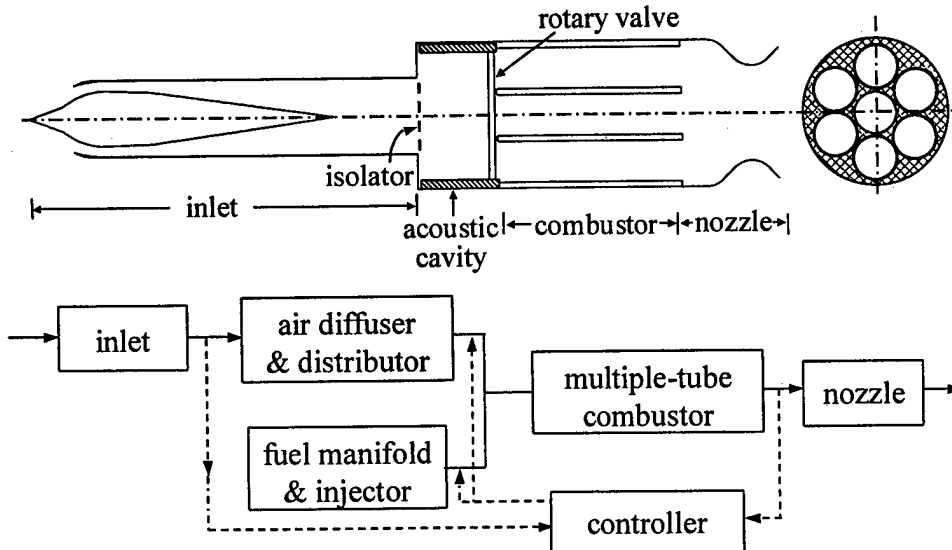


Fig. 4.17. Supersonic air-breathing pulse detonation engine.

solved using a recently developed space-time method which circumvents the deficiencies of existing computational methods for treating detonation waves and shock discontinuities. Both one- and two-dimensional simulations are conducted to study the various fundamental scientific and practical engineering issues involved in the development of PDEs.

The research was conducted at several levels of complexity in a hierarchical manner to establish its accuracy and reliability. The work performed in the past three years focused on the following areas:

1. supersonic inlet dynamics;
2. thermodynamic cycle analysis;
3. single-tube thrust chamber dynamics and performance;
4. effect of nozzle configuration on PDE performance; and
5. multi-tube thrust chamber dynamics and performance.

A summary of the major results in the above areas is give below.

4.2.1. Supersonic Inlet Dynamics

Inlet and its interaction with combustor represent a crucial aspect in the development of PDEs. The inlet is designed to capture and supply stable airflow at a rate demanded by the combustor, and to maintain high-pressure recovery and stability margin at various engine operating conditions. The overall vehicle performance depends greatly on the energy level and

flow quality of the incoming air. A small loss in inlet efficiency may translate into a substantial penalty in net engine thrust. Moreover, any change in the inlet flow structure may modify the downstream combustion characteristics and subsequently lead to undesirable behavior such as flame blow-off and flash-back. Thus, matching inlet behavior to engine requirements is of fundamental importance to designers [87].

In addition to its primary function of supplying air, an inlet simultaneously acts as a sensitive element that may modify the entire system dynamics due to its intrinsic unsteadiness and interactions with the combustion chamber. Typically, pressure waves are produced in the combustion chamber and propagate upstream to interact with the inlet flow through a manifold where mixing of air and fuel occurs. The resultant flow oscillations in the inlet diffuser then either propagate downstream in the form of acoustic waves or are convected downstream with the mean flow in the form of vorticity and entropy waves, and further reinforce the unsteady motions in the combustor. A feedback loop is thus established between the inlet and combustor. The situation becomes much more complicated for a supersonic PDE due to the shock-wave/boundary-layer interaction and shock/acoustic wave interaction [88].

Much effort has been expended to study the inlet aerodynamics and its response to downstream disturbances arising from combustion oscillations. The analysis is based on the axisymmetric, Favre-averaged conservation equations. Turbulence closure is achieved using a two-layer model. The inlet configuration for the present study is shown in Fig. 4.18. It is designed for a flight altitude of 9.3 km and flight Mach number of 2.1. The corresponding static pressure and temperature and total pressure and temperature are 0.29 atm, 228 K, 2.65 atm, and 428 K, respectively. Figure 4.19 presents the Mach-number contours at two different back pressures ($p_b = 2.1$ and 2.2 atm), which are carefully chosen such that the engine operates at a supercritical condition to provide a sufficient shock stability margin. Under these conditions, the two leading conical shocks generated by the double-cone centerbody compress airflow externally, merge slightly above the cowl lip, and form a strong shock which extends into the external-flow region. In addition, a shock stemming from the cowl inner surface continues downstream, hitting and reflecting from both the cowl and centerbody walls and finally leading to a terminal normal shock. The flow in this region undergoes a compression-expansion cycle and becomes subsonic after passing through the normal shock located in the divergent section of the diffuser. During this process, the inlet recovers a high percentage of the freestream total

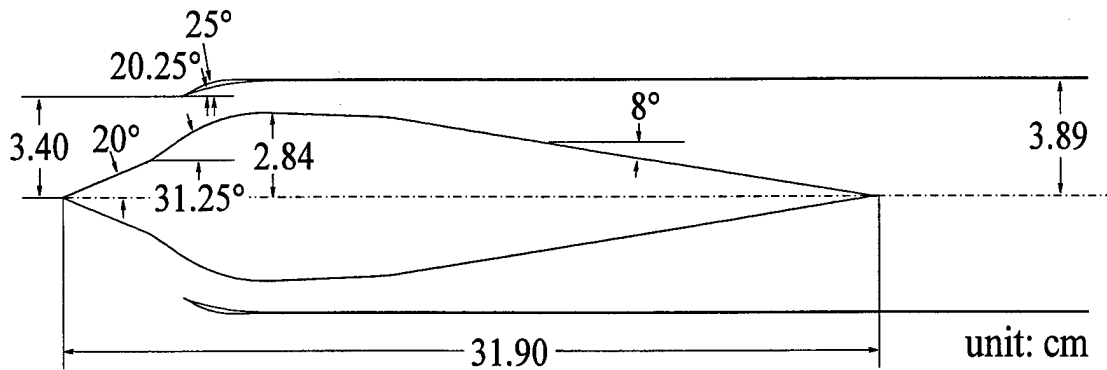


Fig. 4.18. Supersonic inlet with mixed-compression.

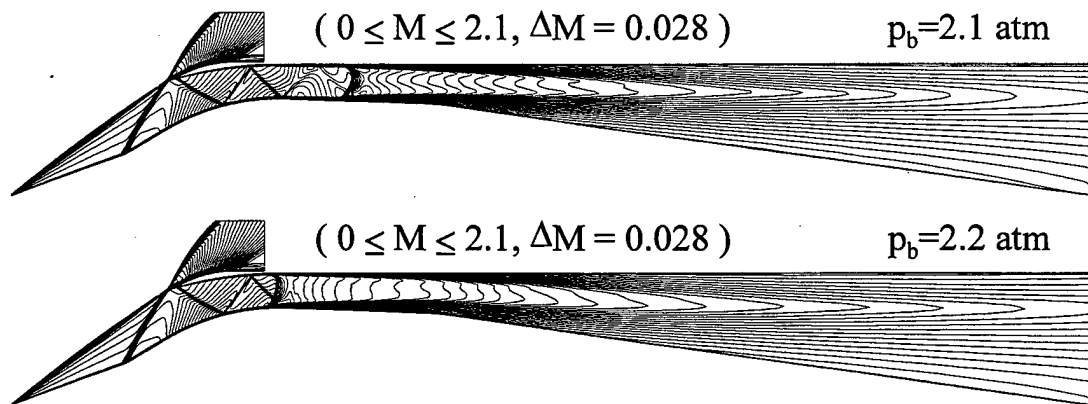


Fig. 4.19. Mach-number contours with different back pressures under steady-state condition.

pressure by decelerating the airflow through the shock system. The pressure recovery coefficients for the two cases are 84% and 88%, respectively, and the Mach numbers immediately in front of the terminal shocks are 1.42 and 1.32.

The response of the inlet shock system to downstream disturbances has also been studied by imposing periodic pressure oscillations at the exit plane. A wide range of fluctuation frequency and amplitude were considered. Important phenomena of concern include oscillations of mass flow rate, pressure recovery and flow distribution, as well as shock displacement. In general, the acoustic response of the inlet flow increases with increasing amplitude of the imposed oscillation, but decreases with the frequency. Also included as part of the result is the acoustic impedance function at the inlet exit, a parameter that can be effectively used to characterize the inlet/combustor coupling [89].

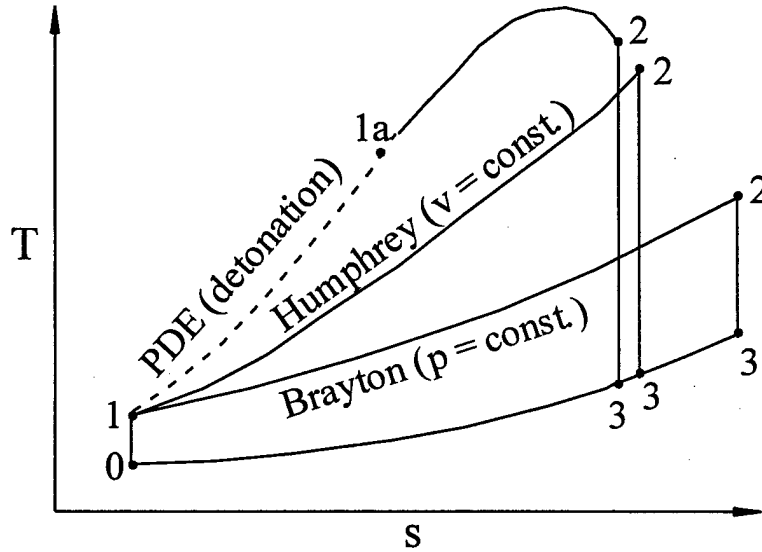


Fig. 4.20. Temperature-entropy diagram of ideal PDE, Humphrey, and Brayton cycles.

4.2.2. Thermodynamic Cycle Analysis

An ideal thermodynamic cycle analysis has been conducted to estimate the theoretical limit of the performance of an air-breathing PDE. Figure 4.20 shows the temperature-entropy diagram of an ideal PDE cycle. The Humphrey (constant-volume) and Brayton (constant-pressure) cycles are also included for comparison. The thermodynamic cycle efficiencies of these cycles are

$$\eta_{th,PDE} = 1 - \frac{\frac{\gamma_1 - 1}{\gamma_2 - 1} \left(\frac{\gamma_2}{\gamma_1} \right)^2 \frac{1}{M_S^2} \left[\frac{1 + \gamma_1 M_S^2}{1 + \gamma_2} \right]^{\frac{\gamma_2 + 1}{\gamma_2}} \psi^{\frac{1 - \gamma_2 - 1}{\gamma_1 - 1} \frac{\gamma_1}{\gamma_2} - 1}}{\tilde{q}} \quad (4.1)$$

$$\eta_{th,Humphrey} = 1 - \frac{\frac{\gamma_2}{\gamma_1} \left[\frac{\gamma_1 - 1}{\gamma_2 - 1} \right]^{\frac{\gamma_2 - 1}{\gamma_2}} \left[\gamma_1 \frac{\tilde{q}}{\psi} + 1 \right]^{\frac{1}{\gamma_2}} \psi^{\frac{1 - \gamma_2 - 1}{\gamma_1 - 1} \frac{\gamma_1}{\gamma_2} - 1}}{\tilde{q}} \quad (4.2)$$

$$\eta_{th,Brayton} = 1 - \frac{\left[\frac{\tilde{q}}{\psi} + 1 \right] \psi^{\frac{1 - \gamma_2 - 1}{\gamma_1 - 1} \frac{\gamma_1}{\gamma_2} - 1}}{\tilde{q}} \quad (4.3)$$

where $\tilde{q} \equiv q/C_{p1}T_0$ is the non-dimensional heat addition, and $\psi \equiv T_1/T_0$ is the cycle static temperature ratio. γ_1 and γ_2 are the specific heat ratios of the unburned and burned gases

separated by the shock, respectively. The Mach number of the detonation wave relative to the unburned gas, M_S , can be calculated using the equation below,

$$M_S^2 = \left[\frac{\gamma_2^2 - \gamma_1}{\gamma_1^2 - \gamma_1} + \frac{\gamma_2^2 - 1}{\gamma_1 - 1} \frac{\tilde{q}}{\psi} \right] + \sqrt{\left[\frac{\gamma_2^2 - \gamma_1}{\gamma_1^2 - \gamma_1} + \frac{\gamma_2^2 - 1}{\gamma_1 - 1} \frac{\tilde{q}}{\psi} \right]^2 - \frac{\gamma_2^2}{\gamma_1^2}} \quad (4.4)$$

With thermodynamic cycle efficiencies available, the specific impulse of each ideal cycle, I_{sp} , can be obtained by a control-volume analysis,

$$I_{sp} = \frac{\sqrt{u_0^2 + 2\eta_{th}q} - u_0}{f g_0} \quad (4.5)$$

where u_0 is the free stream velocity, g_0 the gravitational acceleration, and f the ratio of fuel to air mass flow rate. Figure 4.21 shows the specific impulse as a function of static temperature ratio for a stoichiometric hydrogen/air system at the aforementioned flight condition. The system performance increases with increasing static temperature ratio. The PDE offers the best performance among the three cycles, especially when the static temperature ratio is smaller than 3. This may be attributed to the fact that for a given amount of heat addition, the Mach number of the detonation wave increases with decreasing ψ , as indicated by Eq. (4.4). Consequently, the pre-compression effect of the shock is more significant, leading to a higher temperature and pressure of the unburned gas prior to combustion among the three cycles. When $T_1 = 428$ K ($\psi = 1.877$), the I_{sp} of an ideal PDE reaches 4422 s.

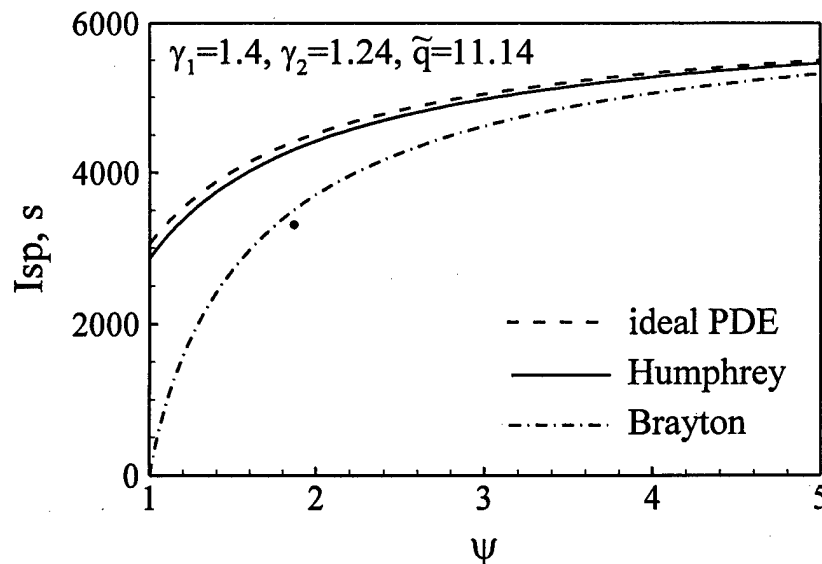


Fig. 4.21. Specific impulse of ideal PDE, Humphrey, and Brayton cycles as function of static temperature ratio ψ .

4.2.3. Single-Tube Thrust Chamber Dynamics

Thorough understanding of the single-tube thrust chamber dynamics represents the very first step in developing a PDE design methodology. The system dynamics is formulated based on the conservation laws for a multi-component chemically reacting system in two-dimensional coordinates. Both detailed and global chemical kinetics for hydrogen fuel are considered. The governing equations and their associated boundary conditions are solved using a recently developed space-time conservation-element/solution-element (CE/SE) method that circumvents the deficiencies of existing numerical methods for treating detonation waves and shock discontinuities [90-93]. The resultant computer code is further parallelized using the Message-Passing-Interface library to improve its efficiency.

A series of single-shot calculations were conducted for a 0.6 m long straight tube. The tube is initially filled up with a stoichiometric hydrogen/air mixture at ambient pressure (p_0) and temperature (T_0). A small driver-gas region with a temperature of 2000 K, a pressure of 30 atm, and a width of 0.2 mm near the head end is implemented for detonation initiation. During the single-shot process, the head-end pressure remains a plateau value (p_3) for certain period and then decays to a value below the ambient state. The impulse can be calculated by integrating the force exerting on the head end with time from the beginning to the instant when the head-end pressure equals to the ambient pressure. The contribution from the driver gas to the impulse is estimated to be less than 0.5%. Figure 4.22 shows the impulse per unit chamber cross-section area as a function of the product of the pressure difference between the plateau and the ambient value and the residence time t_{CJ} ($t_{CJ} = L/D_{CJ}$) for different ambient conditions. The results from Kailasanath's simulations for different tube lengths [94] are included for comparison. Based on the results, the single-shot impulse can be estimated with the following correlation,

$$I/A = 4.04(p_3 - p_0)t_{CJ} \quad (4.6)$$

This expression is similar to that based on a semi-analytical model proposed by Wintenberger et al. [3], which predicts a constant of proportionality of about 4.13.

Calculations are further performed for a single-tube PDE operating at an flight altitude of 9.3 km and a Mach number of 2.1. The total pressure and total temperature at the combustor entrance, obtained from the inlet flow analysis are 2.12 atm and 428 K, respectively. The detonation tube measures a length of 0.6 m and a diameter of 0.16 m. The valve at the tube

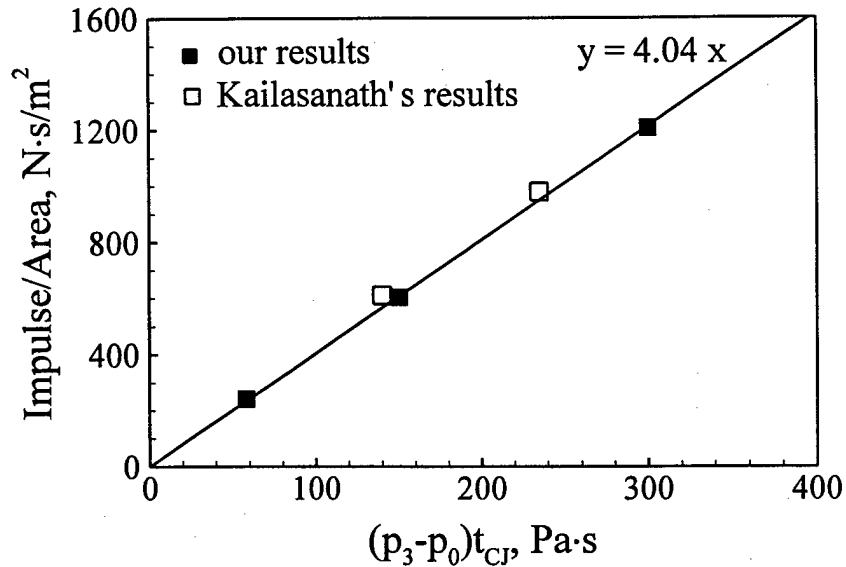


Fig. 4.22. Generalized impulse curve from a series of single-shot simulations of a straight-tube PDE.

entrance is assumed to be either fully open or fully closed. The engine operation sequence is controlled by three time periods: the period (τ_{close}) during which the valve is closed (including the time for detonation initiation, detonation propagation and blow-down), the purging period (τ_{purge}) during which a small amount of cold air is injected to prevent pre-ignition, and the refilling period (τ_{refill}). The sum of these three periods equals to the operation cycle period (τ_{cycle}), i.e., $\tau_{cycle} = \tau_{close} + \tau_{purge} + \tau_{refill}$. The purging period should be as small as possible, as long as it prevents pre-ignition. A small value of 0.1 ms is used for the purging period in all of the calculations.

Figure 4.23 shows the snapshots of the pressure- and density-gradient fields at $t = 0.7$ ms for a case with an operation cycle period of 3 ms and a valve close-up time of 2.4 ms. At this time instant, the primary shock wave degenerating from the detonation wave has moved out of the tube and transformed to a weakened bow shock. Other common features, including the expansion fans located at the edge of the tube exit, the presence of the secondary shock, and the two vortices and rolled-up slip lines developed due to shock diffraction, are all clearly resolved. A detailed wave pattern is numerically obtained by tracing the characteristic lines of the flowfield along the centerline and is shown in Fig. 4.24 for the first cycle of operation. The engine reaches stable cyclic operation at the fifth cycle and the specific impulse (fuel-based, cycle-averaged) is 2328 s. The timing effect on the PDE system performance is explored by

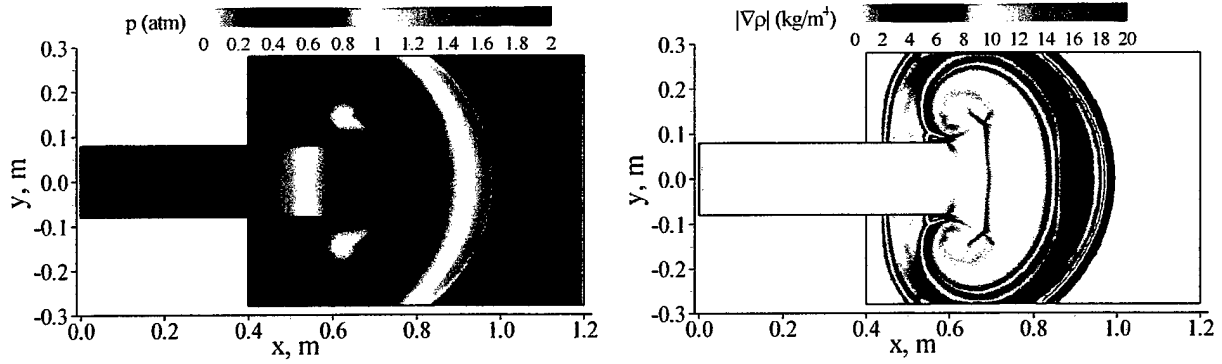
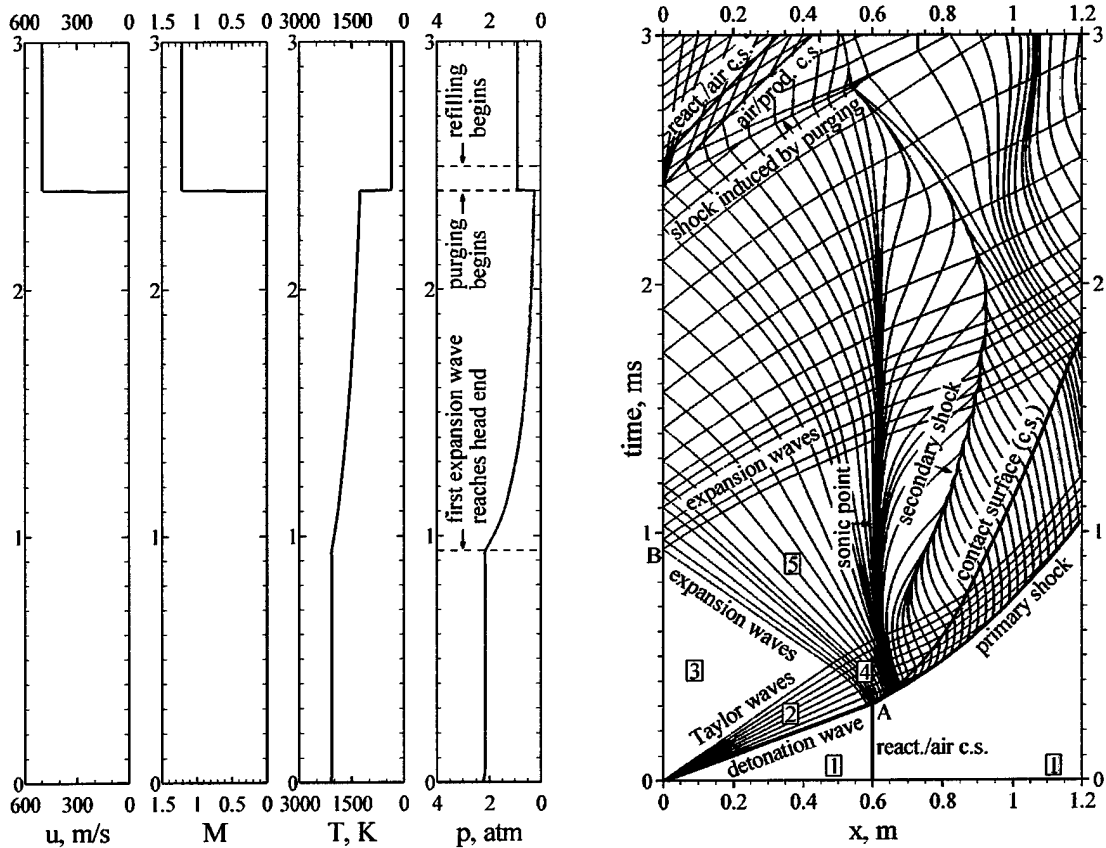
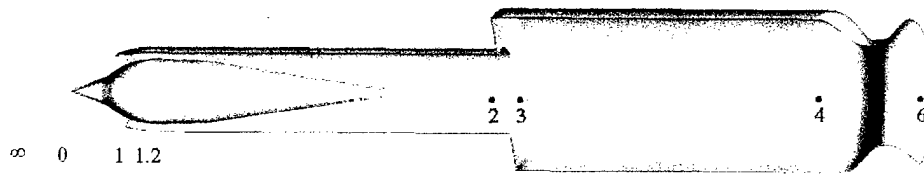


Fig. 4.23. Snapshots of pressure and density-gradient field at $t = 0.7$ ms.



4.24. x - t diagram for the first cycle and time histories of properties at head end under a typical PDE operation ($\tau_{\text{cycle}} = 3$ ms, $\tau_{\text{close}} = 2.4$ ms, $\tau_{\text{purge}} = 0.1$ ms)

varying the valve close-up time. In all the cases considered herein, the specific impulses are far below the prediction from the ideal PDE thermodynamic cycle analysis. For comparison, the performance parameters and flow conditions of a corresponding ramjet engine are given in Fig. 4.25, which has a specific impulse of about 3370 s. Thus, with the straight-tube configuration, a PDE performs much worse than a ramjet engine.



- free stream conditions:
 $M_\infty = 2.1$, $h = 9.3$ km
 $T_{0,\infty} = 428$ K, $p_{0,\infty} = 2.65$ atm
 $T_\infty = 228$ K, $p_\infty = 0.29$ atm
- inlet exit conditions:
 $M_2 = 0.29$, $\dot{m} = 1.01$ kg/s
 $T_{0,2} = 428$ K, $p_{0,2} = 2.23$ atm
 $T_2 = 422$ K, $p_2 = 2.10$ atm
- combustor conditions:
 $M_3 = 0.1$, $M_4 = 0.24$, $\Phi = 1.0$ (H_2)
 $T_{0,4} = 2488$ K, $p_{0,4} = 2.04$ atm
 $T_4 = 2473$ K, $p_4 = 1.96$ atm
- engine performance:
 $F = 963$ N (216 lbf)
 $I_{sp} = 3371$ s

Fig. 4.25. Performance parameters of ramjet engine for stoichiometric hydrogen/air mixture.

4.2.4. Effect of Nozzle Configuration on PDE Performance

Nozzle plays a decisive role in determining the propulsive performance of a PDE. Recent studies [21,95] indicate that nozzle may considerably change the thrust delivered by an engine. In addition to its influence on specific impulse through modification of the gas expansion process, nozzle affects the chamber flow dynamics and, consequently, the timing of various phases of the engine operation cycle, especially for high-altitude cruise and space applications. In general, the question of nozzle optimization is not resolved due to the difficulties arising from the coupling with the other parts of an engine. Ideally, the nozzle contour should change within each cycle and adapt itself to the instantaneous local conditions. It is, however, impossible to design and fabricate such a flexible nozzle with adaptation on the time scales of PDE operation.

Three nozzle configurations, i.e., a convergent, a divergent, and a plug nozzle, were first tested. The performance gain appears limited with these nozzles mainly due to the lack of a physical mechanism for preserving the chamber pressure during the blow-down and refilling processes. In view of this deficiency, a choked convergent-divergent (CD) nozzle was employed. The nozzle has a length of 0.2 m, with a convergent angle of 45° and a divergent angle of 15° . Figure 4.26 shows the snapshots of the pressure- and density-gradient fields at $t = 0.80$ ms for a cycle period of 3 ms and a valve close-up time of 2.1 ms. Steady cyclic

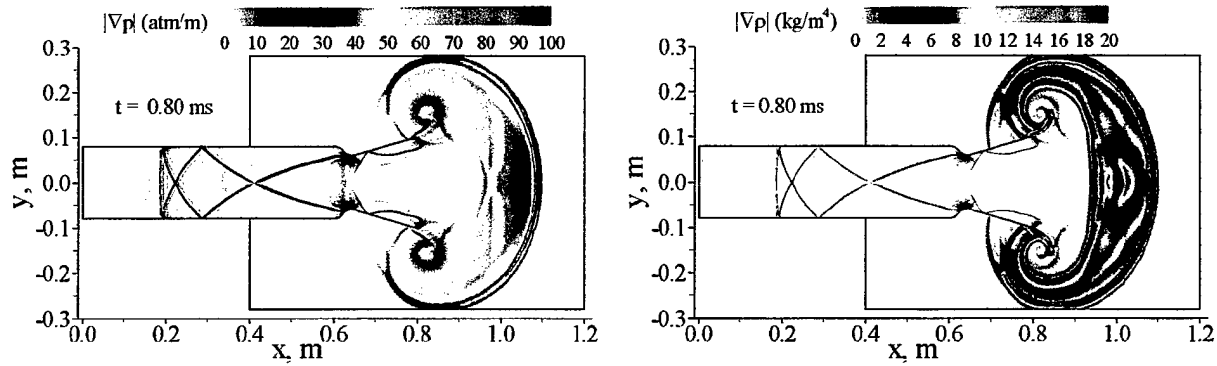


Fig. 4.26. Flow fields at 0.80 ms ($\tau_{cycle} = 3$ ms, $\tau_{close} = 2.1$ ms).

operation is reached at the fifth cycle with a specific impulse of 3120 s, which is 34% higher than the maximum specific impulse obtained from the straight tube cases, demonstrating a substantial improvement by adding a CD nozzle.

A comprehensive parametric study was conducted by varying the cycle period τ_{cycle} and valve close-up time τ_{close} . To save computational effort, quasi one-dimensional calculations were implemented. Tests found that the quasi one-dimensional simulations may overestimate the specific impulse by less than 10%. Figure 4.27 shows the effects of τ_{close} on the specific thrust (air-based) and specific impulse (fuel-based) for four different cycle periods: 2.5 ms, 3 ms, 4 ms, and 5 ms. The specific thrust increases as the valve close-up time τ_{close} decreases for each operation frequency considered herein. For given τ_{cycle} and τ_{purge} , a smaller τ_{close} translates to a shorter blow-down process and thus a higher head-end pressure at the end of the blow-down process, consequently leading to a higher refilling pressure and density during the refilling process. The refilling time also increases, and thus the amount of the reactant refilled increases.

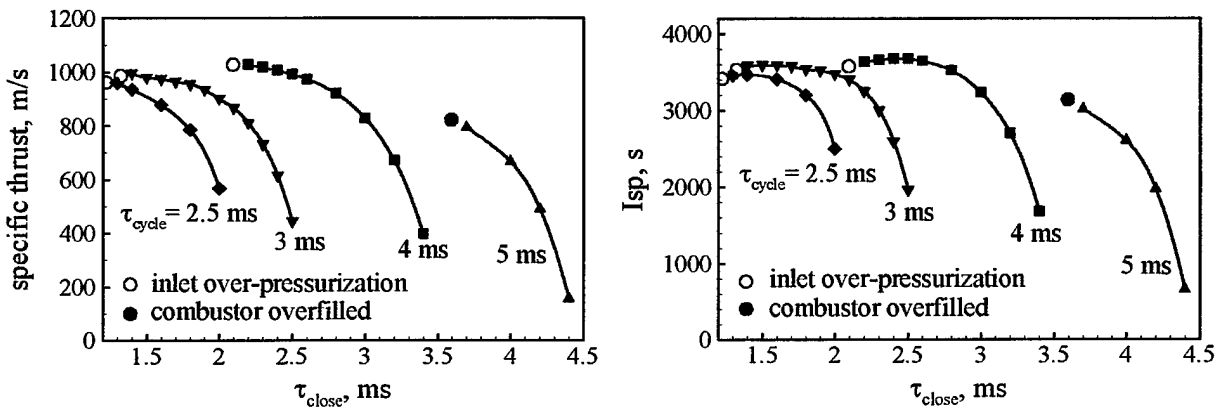


Fig. 4.27. Effects of τ_{close} on specific thrust and specific impulse at four different operation frequencies.

Combined, these two factors result in a higher cycle-averaged chamber pressure and consequently a higher specific thrust. It should be noted, however, that the valve close-up time couldn't be too small. Its lower limit is determined by the following two factors. One is inlet over-pressurization, i.e., the head-end pressure exceeds the air stagnation pressure at the combustor entrance, thereby prohibiting the detonation tube from purging or refilling when the valve is open. The other is over-filling, i.e., the fresh reactant flows out of the nozzle to the external region before being burned, and is wasted unless afterburning is considered. The effect of the valve close-up time on the specific impulse is similar. Figure 4.27 demonstrates that an optimum frequency exists for a given configuration. For the configuration studied herein, the frequency of 250 Hz ($\tau_{cycle} = 4$ ms) offers the best performance margin.

4.2.5. Multi-Tube Thrust Chamber Dynamics

In addition to the study of single-tube PDE system dynamics, much effort was expended to investigate the intricate combustion and gasdynamic processes in multi-tube thrust chambers [96]. As a specific example, a thrust chamber consisting of three detonation tubes connected downstream with a common convergent-divergent nozzle is considered herein. This configuration helps preserve the chamber pressure during the blow-down and refilling stages, and consequently improves the propulsive performance of the engine.

Figure 4.28 presents the time evolution of the density-gradient field within one cycle of operation. The frequency is 333 Hz for each tube. Initially, the bottom tube is partially filled with a stoichiometric hydrogen/air mixture. Detonation is initiated, propagates downstream, and eventually degenerates to a non-reacting shock wave. The resultant shock wave then proceeds further downstream, diffracts at the exit of the tube, reflects on the inner walls, and causes complex waves propagating upstream into all the three detonation tubes and downstream into the nozzle (see Fig. 4.28b). During this period, the middle tube undergoes the purging and refilling processes. After one-third cycle period, detonation is initiated and propagates in the middle tube while the top tube begins to purge burnt gases and refill fresh mixtures (see Fig. 4.28c). The detonation wave then degenerates to a shock wave after passing through the interface between the reactant and purged gases. Further interactions between the shock wave and the local flowfield result in an extremely complex flow structure as shown in Fig. 4.28d. After

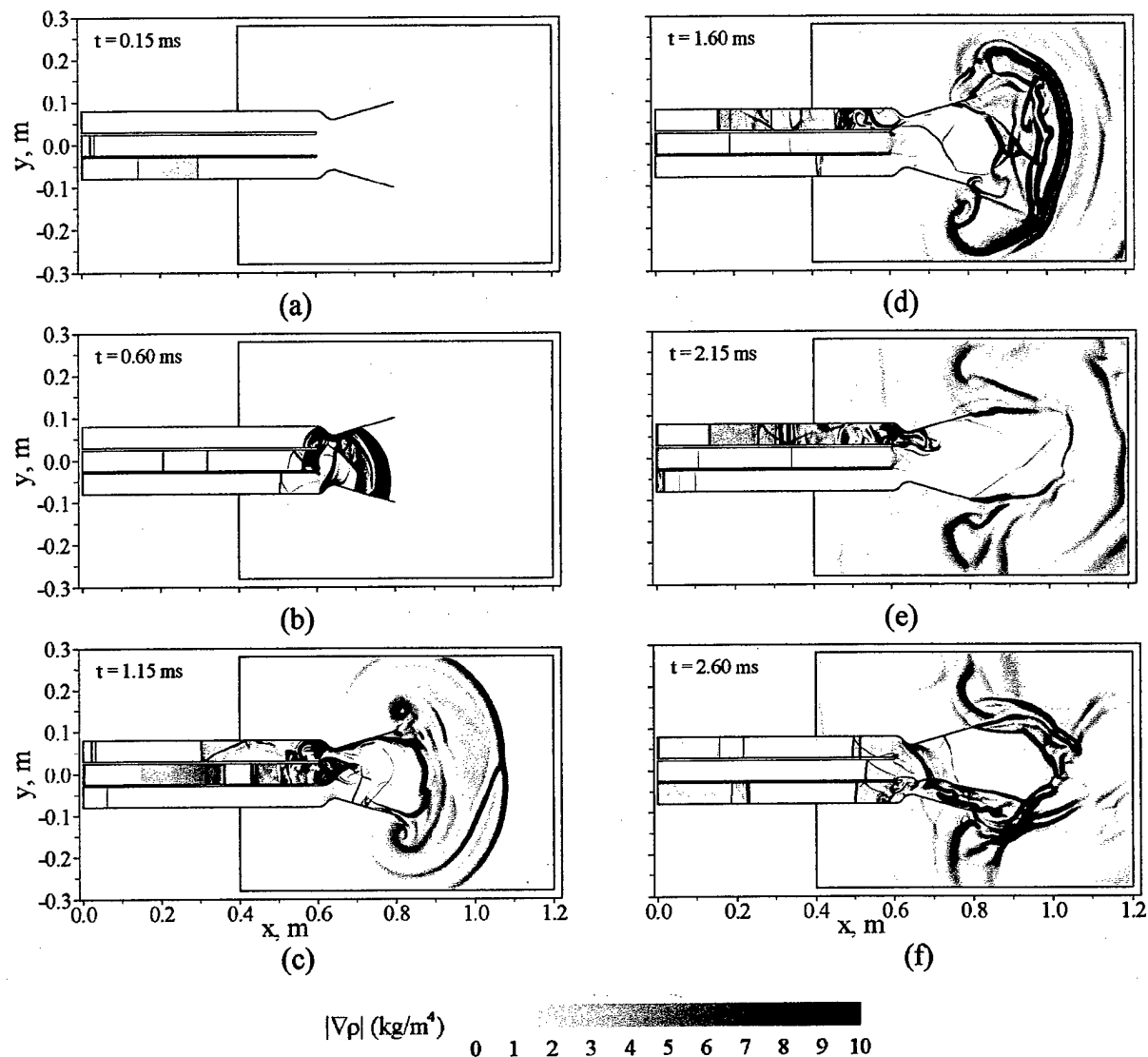


Fig. 4.28. Evolution of density-gradient field during first cycle of operation ($\tau_{cycle} = 3$ ms, $\tau_{close} = 2.1$ ms).

another one-third cycle period, detonation is initiated and propagates in the top tube (see Fig. 4.28e).

Steady cyclic operation is reached at the fifth cycle. Figure 4.29 shows the time evolution of the density-gradient field during the fifth cycle of operation. The cycle-averaged specific impulse is 3279 s, which is about 5% higher than that achieved by a single-tube PDE, demonstrating the improvement by implementing a multi-tube design.

The time history of the instantaneous specific thrust is shown in Fig. 4.30. Also included is the result of the single-tube case for comparison. A very high peak exists for the single-tube

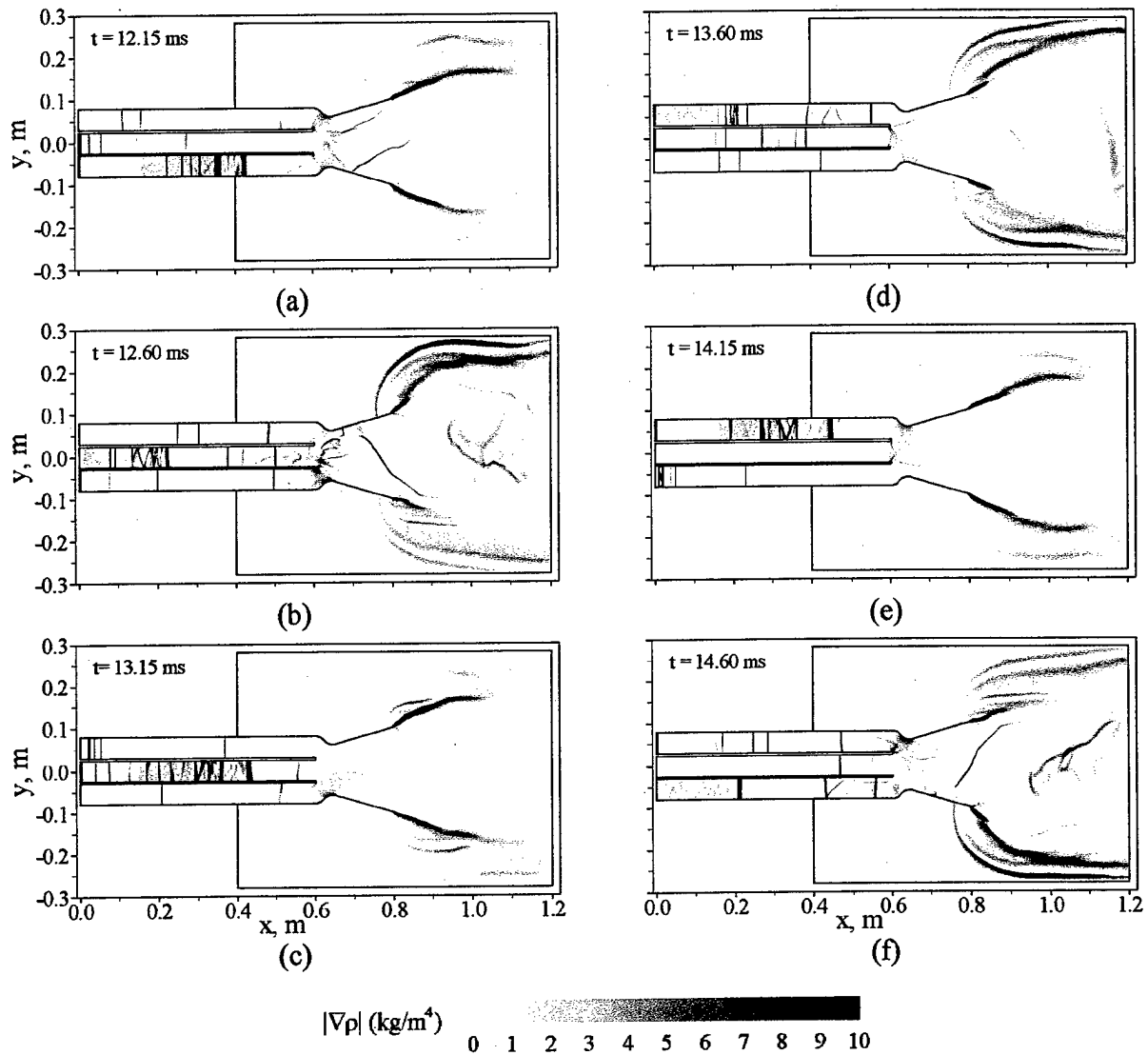


Fig. 4.29. Evolution of density-gradient field during fifth cycle of operation ($\tau_{cycle} = 3$ ms, $\tau_{close} = 2.1$ ms).

case. The deviation of the peak value from the cycle-averaged quantity represents the degree of unsteadiness of the engine operation. For a triple-tube case, the number of peaks increases to three in each cycle, but the peak magnitudes are significantly reduced, showing a substantial improvement in flow steadiness. It should be noted that there exists considerable lateral thrust in a multi-tube PDE due to its unsymmetric operations. The maximum lateral thrust of the present triple-tube engine can reach 1,000 N per kg of air mass flow, thereby causing unnecessary vibration of the vehicle. One way to avoid this problem is the implementation of tube pairs. Each pair of tubes include two detonation tubes which are located at symmetric positions and

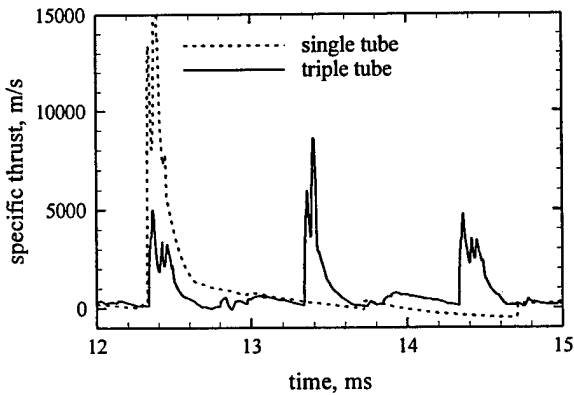


Fig. 4.30. Time history of specific thrust during fifth cycle of operation. ($\tau_{cycle} = 3$ ms, $\tau_{close} = 2.1$ ms).

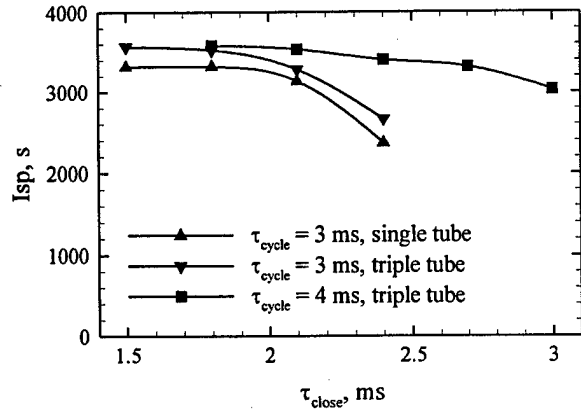


Fig. 4.31. Effects of valve close-up time on specific impulse.

operate synchronously in time to ensure symmetric operation and consequently eliminates the lateral thrust.

A parametric study was also conducted to study the timing effect on system performance by varying τ_{cycle} and τ_{close} . Figure 4.31 shows the effects of τ_{close} on cycle-averaged specific impulse for two different cycle periods: 3 and 4 ms. The single-tube result for $\tau_{cycle} = 3$ ms is also included for comparison. Clearly, the multi-tube design helps improve the system performance.

4.2.6. Summary

The present work provides detailed information about the thrust chamber dynamics of single-tube and multi-tube PDEs. The effects of various operating parameters and chamber configurations on engine performance have been investigated systematically. Results can be effectively utilized to optimize the engine design and to identify the various loss mechanisms limiting the PDE performance.

5. SUMMARY

Experimental and analytical research results reported here provides fundamental understanding related to detonation phenomena in a context that addresses the technology barriers limiting Pulse Detonation Engine development. The multi-university team of Penn State University, Caltech and Princeton University worked cohesively to further scientific understanding of detonation phenomena related to PDE development.

Caltech investigated fundamental detonation physics, detonation initiation techniques, fuel physical properties, detonation cell widths, impulse measurements and modeling for detonation tubes, and the structural aspects of detonation tubes. In this effort, significant accomplishments were achieved. Visualizations of detonation structure using PLIF in propagating detonations led to observations of "keystones" that were correlated to transverse wave structure. Measurements of detonation diffraction were used for developing a simple model for correlating critical diffraction diameter to chemical kinetic and gasdynamic properties of propagating detonations. Detonation cell widths in mixtures of JP10 and air were measured over a range of equivalence ratios and initial pressures. A detonation initiation technique based on torodial imploding waves was also developed. The detonation tube impulse was measured for hydrocarbon fuels using the ballistic pendulum technique. Finally, an analytical model for impulse from a detonation tube was developed and validated against single-cycle and multi-cycle experimental results.

Analytical efforts at Princeton University have focused on understanding chemical kinetics on induction length and propagation and quenching of spray detonations. In the first area of study, several chemistry-related issues on the structure and propagation of detonation waves have been investigated. While the vehicle of study is the ignition length of the C-J wave, and the numerical calculations were conducted for system parameters of interest to PDE applications, the concepts and order of magnitude effects identified are expected to be of general utility. In the second area of study, the phenomena offered by the various heterogeneous, droplet processes in spray detonation was analyzed. The possible existence of optimum droplet sizes and loadings for enhanced detonation propagation and the extension of quenching limits were identified and explained. These phenomena are consequences of the strong coupling between droplet size, drag, vaporization, and loss to the wall, and as such they would not have been

captured had conventional assumptions as in-phase velocities, d^2 -law vaporization, and constant specific heats been made.

The chemical kinetics study convincingly demonstrated that for hydrogen oxidation, the branching-termination chain mechanisms in the overall reaction rate plays an important role, and that increasing pressure can actually moderate its progress. The concept of crossover temperature was applied to derive an operation boundary in terms of initial pressure and temperature, and stoichiometry, in order to avoid operation regimes for which the ignition length could become excessively long. The potential reduction of the detailed hydrogen/oxygen reaction mechanism to simpler schemes suitable for integration into large-scale computations was also investigated. Results demonstrated that, because of the relatively small numbers of species and reactions associated with the H_2/O_2 mechanism as compared to those of hydrocarbon oxidation, only a minimal reduction was possible in that the existing detailed mechanism was probably already almost the smallest for a comprehensive description of hydrogen oxidation. The potential utility of a 2-step mechanism for near-stoichiometric operations is however noted. Finally, by comparing the ignition lengths of hydrogen with those of ethylene and heptane, which are representative hydrocarbon fuels, the effect of compressibility through the upstream speed of sound and Mach number was identified, showing that the potential benefit of the high reactivity of hydrogen is moderated by its lower Mach number and hence lower post-shock temperature and pressure. This negative compressibility effect also indicates that using hydrogen as an ignition enhancer for hydrocarbon fuels can actually prolong the ignition delay.

In the area of spray detonations, of particular interest are the results that show that there exists an optimum droplet size for detonation propagation, such that propagation may be inhibited by reducing the droplet size. The study also showed that viable spray detonation propagation can probably only allow for droplets of the μm size range, up to say 10 μm , for the 38.1 mm tube diameter used in the calculations. Recognizing that most atomization processes produce droplets whose Sauter Mean Diameter is in excess of this range, the fact that detonation is still possible is likely due to the presence of droplet shattering, upon crossing the shock, that significantly reduces the droplet size. The identification of two modes of heat release, Arrhenius versus vaporization controlled, is particularly interesting as they depict two different detonation structures that are affected by the droplet size.

Experimental research at Penn State focused on experimental studies of deflagration to detonation transition (DDT) and detonation transition from predetonator to detonator tubes. Complementary analytical efforts at Penn State focused on understanding supersonic inlet dynamics, and both single-tube and multi-tube thrust chamber dynamics. In addition, the effect of nozzle configuration on PDE performance was also analyzed. Finally a thermodynamic cycle analysis was also performed.

For the experimental DDT studies, the DDT enhancing characteristics of helically configured flat plate obstacles were examined systematically in a series of single-shot ethylene-air experiments. The large-scale turbulence generated by the flow interaction with the obstacles was shown to dramatically increase the flame surface area and consequently increase the burning rate. The production of fine-scale turbulence in the flow boundary layer and in the breakdown of the large-scale vortices was also observed to increase the local burning rate and dramatically accelerate the burning velocity. Obstacle blockage ratios between 0.3 and 0.6, and sufficient obstacle spacing were found to provide optimum levels of flame stretching without inducing excessive flow drag. For all obstacle configurations, the critical step to achieving detonation in these experiments was attaining the C-J deflagration velocity within the obstacle configurations. Any length of obstacle after the compression waves reached the C-J deflagration velocity was observed to be unnecessary and delayed the onset of detonation. After attaining the C-J deflagration velocity, the flame would remain at that speed until it reached the exit of the obstacle configuration, where it would proceed to accelerate and transition to detonation. If the wave had not reached the C-J deflagration velocity before exiting the tube, the compression waves and reaction would decouple and DDT would not occur. Multi-cycle experiments were also conducted to examine the effect on the DDT process of the initial mean flow and turbulence resulting from dynamic injection of the propellants into the tube. Repeatable operation at 10 Hz showed a decrease in DDT time from 6 to 3 ms whereas the DDT length remained constant around 0.95 m. Multi-cycle images of the transition from a strong deflagration to a normal detonation wave were found to be very similar to the results obtained for the single-shot experiments.

A series of studies has also been completed to investigate transitioning of a detonation from a small diameter predetonator tube to a large diameter main thrust tube using obstacles placed in the transition section connecting the two tubes. These results show that transitioning

can occur for a predetonator tube diameter that is less than 9 to 13 detonation cell sizes that is often the criteria observed for unconfined detonation transition. A key result of the current studies is that the conditions in the region just upstream of the transition section are critical in determining whether a successful transition is observed. In particular, achieving a CJ detonation in the predetonator does not assure that a detonation will be initiated in the main thrust tube. In fact, the critical phenomena appear to be the occurrence of localized explosions that occur just prior to establishment of a CJ detonation. It is postulated that the resulting overdriven detonation coupled with shock reflections from the transition obstacle that are focused in the volume of combustible gas in the transition section leads to a rapid energy release in a confined region and results in the initiation of the detonation in the main thrust tube.

The analytical work provides detailed information about the thrust chamber dynamics of single-tube and multi-tube PDEs. The effects of various operating parameters and chamber configurations on engine performance have been investigated systematically. Results can be effectively utilized to optimize the engine design and to identify the various loss mechanisms limiting PDE performance.

6. REFERENCES

- [1] Schultz, E., Wintenberger, E., Shepherd, J. E., "Investigation of Deflagration-to-Detonation Transition for Application to Pulse Detonation Engine Ignition Systems," *Proceedings of the 16th JANNAF Propulsion Symposium*, CPIA, 1999.
- [2] Lieberman, D. H., Parkin, K., and Shepherd, J. E., "Detonation Initiation by a Hot Turbulent Jet for Use in Pulse Detonation Engines" AIAA Paper 02-3909, 2002.
- [3] Wintenberger, E., Austin, J. M., Cooper, M., Jackson, S., and Shepherd, J. E., "An Analytical Model for the Impulse of a Single-Cycle Pulse Detonation Tube," Accepted for Publication in *Journal of Propulsion and Power*, 2002 (see also AIAA Paper 2001-3811).
- [4] Quirk, J. J., "Amrita: A Computational Facility (for CFD modeling)," *29th Computational Fluid Dynamics Lecture Series*, Von Karman Institute, 1998.
- [5] Izumi, K., Aso, S., Nishida, M., "Experimental and Computational Studies of Focusing Processes in Shock Waves Reflected From Parabolic Reflectors," *Shock Waves*, Vol. 3, 1994, pp. 341-345.
- [6] Bartenev, A. M., Khomik, B. E., Gelfand, B. E., Gronig, H., Olivier, H., "Effect of Reflection Type on Detonation Initiation at Shock Wave Focusing," *Shock Waves*, Vol. 10, 2000, pp. 197-204.
- [7] Jackson, S. I., and Shepherd, J. E., "Initiation Systems for Pulse Detonation Engines," AIAA Paper 2002-3627, 2002.
- [8] Manzhalei, V. I., "Detonation Regimes of Gases in Capillaries", *Fiz. Goren. Vzryva*, Vol. 28, No. 3, 1992, pp. 93-99.
- [9] Shepherd, J. E., Nuyt, C. D., Lee, J. J., "Flash Point and Chemical Composition of Aviation Kerosene (Jet A)," Explosion Dynamics Laboratory Report FM99-4, California Institute of Technology, December 1999.
- [10] Austin, J. M., and Shepherd, J. E., "Detonations in Hydrocarbon Fuel Blends," Accepted for Publication in *Combustion and Flame*, 2002.
- [11] Brabbs, T. A. and Merritt, S. A. "Fuel-rich Catalytic Combustion of a High Density Fuel," Technical Report 3281, NASA, 1993.

- [12] Tieszen, S. R., Stamps, D. W., Westbrook, C. K., Pitz, W. J., "Gaseous Hydrocarbon-Air Detonations", *Combustion and Flame*, Vol. 84, No. 3, 1991, pp. 376-390.
- [13] White, D., "Turbulent Structure in Gaseous Detonations," *Physics of Fluids*, Vol. 4, 1961, pp. 465-480.
- [14] Voitsekhovskii, B., Mitrofanov, V., and Topchian, M., "Struktura Fronta Detonastii i Gaza," Akad. Nauk. SSSR, Novosibirsk, Translation: The Structure of a Detonation Front in Gases, Rep. FTD-MT-64-527, Foreign Technology Division, Wright-Patterson A.F.B., Ohio, 1966
- [15] Edwards, D., Hooper, G., and Meddins, R., "Instabilities in the Reaction Zones of Detonation Waves," *Astronaut. Acta*, Vol. 17 (4-5), 1972, pp. 475-485.
- [16] Takai R., Yoneda, K., and Hikita, T., "Study of Detonation Wave Structure" 15th *International Symposium on Combustion*, 1974, pp. 69-78.
- [17] Pintgen, F., Eckett, C., Austin, J. M., Shepherd, J. E., "Direct Observations of Reaction Zone Structure in Propagating Detonations," Accepted for Publication in *Combustion and Flame*, 2002 (see also AIAA Paper 2002-0773).
- [18] Pintgen, F., Austin, J. M., and Shepherd, J. E., "Detonation Front Structure: Variety and Characterization," International Colloquium on Advances in Confined Detonations, July 2-5 2002, Moscow.
- [19] Schultz, E., "Detonation Diffraction through an Abrupt Area Expansion", PhD thesis, California Institute of Technology, 2000.
- [20] Cooper, M., Jackson, S., Austin, J. M., Wintenberger, E., and Shepherd, J. E., "Direct Experimental Impulse Measurements for Detonations and Deflagrations", Accepted for Publication in *Journal of Propulsion and Power*, 2002 (see also AIAA Paper 2001-3812).
- [21] Cooper, M., and Shepherd, J. E., "The Effect of Nozzles and Extensions on Detonation Tube Performance," AIAA Paper 2002-3628, 2002.
- [22] Kaneshige, M. and Shepherd, J. E., "Detonation Database" Technical Report FM97-8, GALCIT, July 1997. See also the electronic hypertext version at http://www.galcit.caltech.edu/detn_db/html/.
- [23] Li, C., Kailasanath, K., and G. Patnaik, "A Numerical Study of Flow Field Evolution in a Pulsed Detonation Engine," 38th AIAA Paper 2002-0314, 2002.

- [24] Zhdan, S. A., Mitrofanov, V. V., and Sychev, A. I., "Reactive Impulse from the Explosion of a Gas Mixture in a Semi-Infinite Space," *Combustion, Explosion and Shock Waves*, Vol. 30, No. 5, 1994, pp. 657-663.
- [25] Kennedy, J. E., "The Gurney Model of Explosive Output for Driving Metal," *Explosive Effects and Applications*, edited by J. A. Zuker and W. P. Walters, Chap. 7, Springer, New York, 1998, pp. 221-257.
- [26] Schauer, F., Stutrud, J., Bradley, R., "Detonation Initiation Studies and Performance Results for Pulsed Detonation Engines", AIAA Paper 2001-1129, 2001.
- [27] Beltman, W. and Shepherd, J., "Linear Elastic Response of Tubes to Internal Detonation Loading," *Journal of Sound and Vibration*, Vol. 252, No. 4, 2002, pp. 617-655.
- [28] Beltman, W., Burscu, E., Shepherd, J. E. and Zuhai, L., "The Structural Response of Tubes to Internal Shock Loading," *Journal of Pressure Vessel Technology*, Vol. 121, 1999, pp. 315-322.
- [29] Lew, A. and Koslowski, M., "Plastic Response of Thin Tubes to Gaseous Detonation Waves," Ae104 Project Report, Graduate Aeronautical Laboratories, California Institute of Technology, 1999.
- [30] Chao, T. and Shepherd, J. E., "Fracture Response of Externally Flawed Cylindrical Shells to Internal Gaseous Detonation Loading," to appear in *Proceedings of ASME Pressure Vessels and Piping Conference*, Vancouver, British Columbia, Canada, August 4-8, 2002
- [31] T. Chao, Wintenberger, E. and Shepherd, J. E., "On the Design of Pulse Detonation Engines," Explosion Dynamics Laboratory Report FM00-7, California Institute of Technology, January 2001.
- [32] Strehlow, R., *Combustion Fundamentals*, McGraw Hill Book Co., New York, 1984.
- [33] Lee, J. H. S., "Dynamic Parameters of Gaseous Detonations," *Annual Review of Fluid Mechanics*, Vol. 16, 1984, pp. 311-36.
- [34] Kreutz, T. G. and Law, C. K., "Ignition in Nonpremixed Counterflowing Hydrogen versus Heated Air: Computational Study with Detailed Chemistry," *Combustion and Flame*, Vol. 104, 1996, pp. 157-175.

- [35] Fotache, C. G., Kreutz, T. G. and Law, C. K., "Ignition of Counterflowing Methane versus Heated Air under Reduced and Elevated Pressures," *Combustion and Flame*, Vol. 108, 1996, pp. 442-470.
- [36] Kim, T. J., Yetter, R. A. and Dryer, F. L., "New Results on Moist CO Oxidation: High Pressure, High Temperature Experiments and Comprehensive Kinetic Modeling," *Twenty-Fifth International Symposium on Combustion*, The Combustion Institute, 1994, pp. 759-766.
- [37] Wang, H., http://ignis.me.udel.edu/model_release.html.
- [38] Davis, S. G. and Law, C. K., "Laminar Flame Speed and Oxidation Kinetics of Iso-Octane/Air and n-Heptane/Air Flames," *Twenty-Seventh International Symposium on Combustion*, The Combustion Institute, 1998, pp. 521-528.
- [39] Shepherd, J. E., "Chemical Kinetics of Hydrogen-Air-Diluent Detonations," *Dynamics of Explosions*, (Eds.: J. R. Bowen, J. C. Leyer, and R. I. Soloukhin), Vol. 106, 1986, pp. 263-293.
- [40] Lam, S. H. and Goussis, D. A., "Understanding Complex Chemical Kinetics with Computational Singular Perturbation," *Twenty-Second International Symposium on Combustion*, The Combustion Institute, 1998, pp. 931-941.
- [41] Lu, T. F., Ju, Y. and Law, C. K., "Complex CSP for Chemistry Reduction and Analysis," *Combustion and Flame*, Vol. 126, 2001, pp. 1445-1455.
- [42] Dabora E. K., "Fundamental Mechanisms of Liquid Spray Detonations," in *Fuel-Air Explosions* (J. H. S. Lee and C. M. Guirao, Eds.), University of Waterloo Press, Waterloo, 1982, pp. 245-264.
- [43] Sichel M., "The Detonation of Sprays: Recent Results," in *Fuel-Air Explosions* (J. H. S. Lee and C. M. Guirao, Eds.), University of Waterloo Press, Waterloo, 1982, pp. 265-302.
- [44] Smirnov, N. N., Zverev N. I. and Tyurnikov M. V., "Two-Phase Flow Behind a Shock Wave with Phase Transitions and Chemical Reactions," *Experimental Thermal and Fluid Science*, Vol. 13, 1996, pp. 11-20.

- [45] Williams, F. A., "Detonation and Two Phase Flow," *Progress in Astronautics and Rocketry*, (S. S. Penner and F. A. Williams, Eds.), Academic Press, New York, Vol. 6, 1962, pp. 99-114.
- [46] Zeldovich, Ya. B., Gelfond, B. E., Kazhdan, Ya. M. and Frolov, S. M., "Detonation Propagation in a Rough Tube Taking Account of Deceleration and Heat Transfer," *Combustion, Explosion & Shockwave*, Vol. 23, 1987, p. 103.
- [47] Kusharin, A. Y., Agafonov, G. L., Popov, O. E. and Gelfand, B. E., "Detonability of H₂/CO/CO₂/Air Mixtures," *Combustion Science and Technology*, Vol. 135, 1998, pp. 85-98.
- [48] Teodorczyk, A., "Structure and Velocity Deficit of Gaseous Detonation in Rough Tube," *Progress Astronautics A*, Vol. 153, 1993, pp. 405-424.
- [49] Ju, Y. and Law, C. K., "Propagation and Quenching of Detonation Waves in Particle Laden Mixtures," *Combustion and Flame*, Vol. 129, 2002, pp. 356-364.
- [50] Fan, B. C. and Sichel, M., "A Comprehensive Model for the Structure of Dust Detonations," *Twenty-Second International Symposium on Combustion*, The Combustion Institute, 1988, pp. 1741-1750.
- [51] Lee, D. and Sichel, M., "The Chapman-Jouguet Condition and Structure of Detonations in Dust-Oxidizer Mixtures," Presented at the 10th ICDERS, Berkeley, California, August 4-9, 1985.
- [52] Law, C. K., "A Theory for Monodisperse Spray Vaporization in Adiabatic and Isothermal Systems," *International Journal of Heat and Mass Transfer*, Vol. 18, 1975, pp. 1285-1292.
- [53] Law, C. K., "Adiabatic Spray Vaporization with Droplet Temperature Transient," *Combustion Science and Technology*, Vol. 15, 1977, pp. 65-74.
- [54] Liu, C. C. and Lin, T. H., "The Interaction Between External and Internal Heat-Losses on the Flame Extinction of Dilute Sprays," *Combustion and Flame*, Vol. 85, 1991, pp. 468-478.
- [55] Eidelman, S. and Burcat A., "Evolution of a Detonation Wave in a Cloud of Fuel Droplets: Part I. Influence of Igniting Explosion," *AIAA Journal*, Vol. 18, 1980, pp. 1103-1109.
- [56] Law, C. K., "Recent Advances in Droplet Vaporization and Combustion," *Progress in Energy and Combustion*, Vol. 8, No. 3, 1982, pp. 171-201.

- [57] Williamham, C. B., Taylor, W. J., Pignocco, J. M. and Rossini, F. D., "Vapor Pressures and Boiling Points of Some Paraffin, Alkylcyclopentane, Alkylcyclohexane, and Alkylbenzene Hydrocarbons," *Journal of Research*, National Bureau of Standards (U.S.), Vol. 35, 1945, pp. 219-244.
- [58] Held, T. J., Marchese, A. J. and Dryer, F. L., "A Semi-Empirical Reaction Mechanism for n-Heptane Oxidation and Pyrolysis," *Combustion Science and Technology*, Vol. 123, 1997, pp. 101-196.
- [59] Lee, F. P., Kauffman, C. W., Nicholls, J. A., and Sichel, M., "Detonability of RDX Dust in Air Oxygen Mixtures," *AIAA Journal*, Vol. 24, 1986, pp. 1811-1816.
- [60] Lindstedt, R., and Michels, H., "Deflagration to Detonation Transitions and Strong Deflagrations in Alkane and Alkene Air Mixtures," *Combustion and Flame*, Vol. 76, No. 2, 1989, pp. 169-181.
- [61] Moen, I., Lee, J. H. S., Hjertager, B., Fuhre, K., and Eckhoff, R., "Pressure Development Due to Turbulent Flame Propagation In Large-Scale Methane-Air Explosions," *Combustion and Flame*, Vol. 47, No. 1, 1982, pp. 31-52.
- [62] Hjertager, B., Fuhre, K., Parker, S., and Bakke, J., "Flame Acceleration of Propane-Air in a Large-Scale Obstructed Tube," Presented at the 9th ICODERS, Poitiers, France, 1983.
- [63] Lindstedt, R., and Michels, H., "Deflagration to Detonation Transitions in Mixtures of Alkane LNG/LPG Constituents with O₂/N₂," *Combustion and Flame*, Vol. 72, No. 1, 1988, pp. 63-72.
- [64] Moen, I., Donato, M., Knystautas, R., Lee, J. H. S., and Wagner, H., "Turbulent Flame Propagation and Acceleration in the Presence of Obstacles," Presented at the 7th ICOGER, Göttingen, Germany, 1979.
- [65] Moen, I., Donato, M., Knystautas, R., and Lee, J. H. S., "Flame Acceleration Due to Turbulence Produced by Obstacles," *Combustion and Flame*, Vol. 39, No. 1, 1980, pp. 21-32.
- [66] Chan, C., Moen, I., and Lee, J. H. S., "Influence of Confinement on Flame Acceleration Due to Repeated Obstacles," *Combustion and Flame*, Vol. 49, No. 1, 1983, pp. 27-39.

- [67] Benedick, W., Guirao, C., Knystautas, R., and Lee, J. H. E., "Critical Charge for the Direct Initiation of Detonation in Gaseous Fuel/Air Mixtures," *Progress in Astronautics and Aeronautics*, Vol. 106, 1986, pp. 181-202.
- [68] Guirao, C., Knystautas, R., and Lee, J. H. S., "A Summary of Hydrogen-Air Detonation Experiments," SAND 87-7128, 1987.
- [69] Urtiew, P., and Oppenheim, A., "Experimental Observations of the Transition to Detonation in an Explosive Gas," *Proceedings of The Royal Society of London, Series A*, Vol. 295, 1966, pp. 13-28.
- [70] Sileem, A., Kassooy, D., and Hayashi, A., "Thermally Initiated Detonation through Deflagration to Detonation Transition," *Proceedings of The Royal Society of London, Series A*, Vol. 435, 1991, pp. 459-482.
- [71] Chan, C., "Collision of a Shock Wave with Obstacles in a Combustible Mixture," *Combustion and Flame*, Vol. 100, 1995, pp. 341-348.
- [72] Santoro, R., Broda, J., Conrad, C., Woodward, R., Pal, S., and Lee, S.-Y., "Multidisciplinary Study of Pulse Detonation Engine Propulsion," *JANNAF, 36th CS/PSHS/APS Joint Meetings*, 1999.
- [73] Knystautas, R., Guirao, C., Lee, J. H. E., and Sulmistras, A., "Measurements of Cell Size in Hydrocarbon-Air Mixtures and Predictions of Critical Tube Diameter, Critical Initiation Energy, and Detonability Limits," *AIAA Journal*, 1984, pp. 23-37.
- [74] McBride, B., and Gordon, S. "Computer Program for Calculation of Complex Chemical Equilibrium Compositions and Applications," NASA Reference Publication 1311, 1996.
- [75] Knystautas, R., Lee, J. H. S., Shepherd, J., and Teodorczyk, A., "Flame Acceleration and Transition to Detonation in Benzene-Air Mixtures," *Combustion and Flame*, Vol. 115, No.2, 1998, pp. 424-436.
- [76] Ciccarelli, G., and Boccio, J., "Detonation Wave Propagation Through a Single Orifice Plate in a Circular Tube," *Proceedings of the Combustion Institute*, Vol. 27, 1998, pp. 2233-2239.
- [77] Lee, J. H. S., and Moen, I., "The Mechanism of Transition From Deflagration to Detonation in Vapor Cloud Explosions," *Progress in Energy and Combustion Science*, Vol. 6, No. 4, 1980, pp. 359-389.

- [78] Poinso, T., Veynate, D., and Candel, S., "Diagrams of Premixed Turbulent Combustion Based on Direct Simulation," *Proceedings of the Combustion Institute*, Vol. 23, 1990, pp. 613-619.
- [79] Bartlma, F. and Schroder, K., "The Diffraction of a Plane Detonation Wave at a Convex Corner," *Combustion and Flame*, Vol. 66, 1986, pp. 237-248.
- [80] Desbordes, D., "Transmission of Overdriven Plane Detonations: Critical Diameter as a Function of Cell Regularity and Size," *AIAA Journal*, 1988, pp. 170-185.
- [81] Knystautas, R., Lee, J. H., and Guirao, C., "The Critical Tube Diameter for Detonation Failure in Hydrocarbon-Air Mixtures," *Combustion and Flame*, Vol. 46, 1982, pp. 63-83.
- [82] Urtiew, P. and Oppenheim, A., "Experimental Observations of the Transition to Detonation in an Explosive Gas," *Proceedings of The Royal Society of London, Series A*, Vol. 295, 1966, pp. 13-28.
- [83] Sileem, A., Kassoy, D., and Hayashi, A., "Thermally Initiated Detonation through Deflagration to Detonation Transition," *Proceedings of The Royal Society of London, Series A*, Vol. 435, 1991, pp. 459-482.
- [84] Lee, S-Y., Conrad, C., Watts, J., Woodward, R., Pal, S. and Santoro, R. J., "Deflagration to Detonation Transition Using Simultaneous Schlieren and OH PLIF Images," AIAA Paper 2000-3217, 2000.
- [85] Santoro, R. J., Conrad, C., Lee, S-Y., and Pal S., "Fundamental Multi-cycle Studies of the Performance of Pulse Detonation Engines," 15th International Symposium on Air Breathing Engines, September 2-7, 2001, Bangalore, India.
- [86] Nettleton, M., "Shock Attenuation in a Gradual Area Expansion," *Journal of Fluid Mechanics*, Vol. 60, 1973, pp. 209-223.
- [87] Yang, V. and Cappuccio, M., "Supersonic Inlet Design for Missiles," Research Report, Department of Mechanical Engineering, The Pennsylvania State University. 1990.
- [88] Yang, V. and Culick, F. E. C., "Analysis of Unsteady Inviscid Diffuser Flow with a Shock Wave," *Journal of Propulsion and Power*, Vol. 1, 1985, pp. 222-228.
- [89] Oh, J. Y., Ma, F. H., Hsieh, S. Y., and Yang, V., "Interactions Between Shock Waves and Acoustic Waves in a Supersonic Inlet Diffuser", submitted to *Journal of Propulsion and Power*, 2002.

- [90] Chang, S. C., "The Method of Space-Time Conservation Element And Solution Element - A New Approach for Solving the Navier-Stokes and Euler Equations," *Journal of Computational Physics*, Vol. 119, 1995, pp. 295-324.
- [91] Wang, X. Y. and Chang, S. C., "A 2D Non-Splitting Unstructured Triangular Mesh Euler Solver Based on the Space-Time Conservation Element and Solution Element Method," *Computational Fluid Dynamic Journal*, Vol. 8, No. 2, 1999, pp. 309-325.
- [92] Wu, Y. H., Yang, V, and Chang S. C., "Numerical Simulation of Detonation with Detailed Chemical Kinetics Using the Space-Time Method," AIAA Paper 2000-0317, 2000.
- [93] Wu, Y. H., Yang, V, and Chang S. C., "Numerical Simulation of Chemically Reacting Flows with Detailed Chemical Kinetics Using the Space-Time Method," *Proceedings of 1st International Conference on Computational Fluid Dynamics*, Springer-Verlag, 2000.
- [94] Kailasanath, K., Li, C., and Cheatham S., "Computational Studies of Pulse Detonation Engines," 15th ONR Propulsion Meeting, Washington, DC, August 2002.
- [95] Cambier, J. L. and Tegner, J. K., "Strategies for Pulse Detonation Engine Performance Optimization," *Journal of Propulsion and Power*, Vol. 14, 1998, pp. 489-498.
- [96] Ma, F. H., Choi, J. Y., Wu, Y. H., and Yang, V., "Modeling of Multi-Tube Pulse Detonation Engine Dynamics," *Proceedings of International Colloquium on Advances in Confined Detonations*, Moscow, Russia, July 2002.

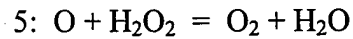
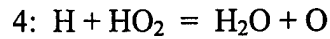
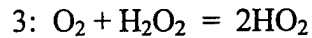
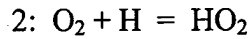
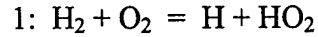
APPENDIX: REDUCED MECHANISMS

5-Step Reduced Mechanism:

QSS species: OH

Non-QSS Species: H₂, O₂, H₂O, O, H, HO₂, H₂O₂

Global Reactions:



Global Reaction Rates:

$$GW_1 = W_2 + W_3 + W_5 - W_{10} - W_{17}$$

$$GW_2 = -W_5 + W_6 + W_7 + W_8 + W_9 - W_{15}$$

$$GW_3 = -W_2 - W_4 - W_6 - W_7 - W_{11} - W_{12} - W_{14} + W_{17} + W_{19}$$

$$GW_4 = -W_2 + W_3 - 2W_4 - W_6 - W_7 + W_8 - W_{11} - W_{12} + W_{13} - W_{15} - W_{18} + W_{19}$$

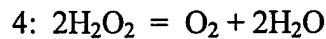
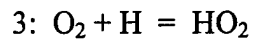
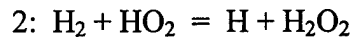
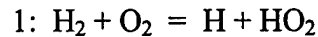
$$GW_5 = W_2 + W_4 + W_6 + W_7 + W_{11} + W_{12} + W_{15} + W_{16} + W_{18}$$

4-Step Reduced Mechanism:

QSS species: OH, O

Non-QSS Species: H₂, O₂, H₂O, H, HO₂, H₂O₂

Global Reactions:



Global Reaction Rates:

$$GW_1 = W_2 + W_4 + W_5 - W_8 - W_{10} - W_{13} - W_{14} + W_{15} + W_{18}$$

$$GW_2 = W_3 - W_4 + W_8 + W_{13} + W_{14} - W_{15} - W_{17} - W_{18}$$

$$GW_3 = -W_2 + W_3 - 2W_4 - W_5 + 2W_8 + W_9 - W_{11} - W_{12} + W_{13} - 2W_{15} - W_{18} + W_{19}$$

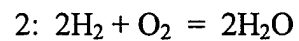
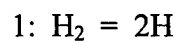
$$GW_4 = (W_3 - W_4 + W_8 + W_{13} + W_{16} + W_{19})/2$$

2-Step Reduced Mechanism:

QSS species: OH, O, H₂O₂, HO₂

Non-QSS Species: H₂, O₂, H₂O, H

Global Reactions:



Global Reaction Rates:

$$\text{GW}_1 = \text{W}_2 + \text{W}_4 + \text{W}_5 - \text{W}_8 - \text{W}_9 + \text{W}_{11} + \text{W}_{12} + 2\text{W}_{14} - \text{W}_{16} - 2\text{W}_{17} - \text{W}_{18} - 2\text{W}_{19}$$

$$\text{GW}_2 = (\text{W}_3 - \text{W}_4 + \text{W}_8 + \text{W}_{13} + \text{W}_{16} + \text{W}_{19})/2$$

REPORT DOCUMENTATION PAGE

Form Approved
OMB No. 0704-0188

The public reporting burden for this collection of information is estimated to average 1 hour per response, including the time for reviewing instructions, searching existing data sources, gathering and maintaining the data needed, and completing and reviewing the collection of information. Send comments regarding this burden estimate or any other aspect of this collection of information, including suggestions for reducing this burden, to Department of Defense, Washington Headquarters Services, Directorate for Information Operations and Reports (0704-0188), 1215 Jefferson Davis Highway, Suite 1204, Arlington, VA 22202-4302. Respondents should be aware that notwithstanding any other provision of law, no person shall be subject to any penalty for failing to comply with a collection of information if it does not display a currently valid OMB control number.

PLEASE DO NOT RETURN YOUR FORM TO THE ABOVE ADDRESS.

1. REPORT DATE (DD-MM-YYYY) 09/01/2003	2. REPORT TYPE Final Technical Report	3. DATES COVERED (From - To) 30-APR-1999 to 01-OCT-2002
--	---	---

4. TITLE AND SUBTITLE A Multidisciplinary Study of Pulse Detonation Engine Propulsion	5a. CONTRACT NUMBER
	5b. GRANT NUMBER N00014-99-I-0744
	5c. PROGRAM ELEMENT NUMBER

6. AUTHOR(S) Robert J. Santoro Vigor Yang Joseph E. Shepherd Chung K. Law	5d. PROJECT NUMBER
	5e. TASK NUMBER
	5f. WORK UNIT NUMBER

7. PERFORMING ORGANIZATION NAME(S) AND ADDRESS(ES) The Pennsylvania State University Dept. of Mech. and Nucl. Engr. Propulsion Engineering Research Center 240 Research Building East University Park, PA 16802	8. PERFORMING ORGANIZATION REPORT NUMBER
---	---

9. SPONSORING/MONITORING AGENCY NAME(S) AND ADDRESS(ES) Office of Naval Research Program Officer, Gabriel D. Roy ONR 333 Ballston Centre Tower One, 800 North Quincy Street Arlington, VA 22217-5660	10. SPONSORING/MONITOR'S ACRONYM(S) ONR
	11. SPONSORING/MONITORING REPORT NUMBER

12. DISTRIBUTION/AVAILABILITY STATEMENT

Approved for public release, distribution unlimited.

13. SUPPLEMENTARY NOTES

14. ABSTRACT

The multidisciplinary research effort brought together a team of leading researchers at Penn State, Caltech and Princeton University in the areas of initiation and propagation of detonations, liquid hydrocarbon spray detonation, combustion chemistry, injector and flow field mixing, and advanced diagnostics to study the fundamental phenomena of importance under both static and dynamic conditions representative of actual pulse detonation engine operation. The team focused its effort on conducting key experiments and analysis in the areas of (a) Fundamental Detonation Studies, (b) Injection, Mixing and Initiation, (c) Inlet-Combustor-Nozzle Performance, (d) Multi-Cycle Operation, and (e) Computer Simulation and Cycle Analysis. The results obtained in these five study areas, coupled with the results of the effort by the sister MURI team led by the Univ. of Calif. at San Diego in some of the aforementioned study areas and in the remaining two study areas of (a) Diagnostics and Sensors, and (b) Dynamics and Control, provide the foundation needed for the development of a PDE system.

15. SUBJECT TERMS

Detonations, Pulse Detonation Engines, Deflagration to Detonation Transition, Sprays, Chemical Kinetics, Ignition

16. SECURITY CLASSIFICATION OF:			17. LIMITATION OF ABSTRACT Unclassified	18. NUMBER OF PAGES 125	19b. NAME OF RESPONSIBLE PERSON Robert J. Santoro
a. REPORT UC	b. ABSTRACT UC	c. THIS PAGE UC			19b. TELEPHONE NUMBER (Include area code) 814-863-1285